

---

# Evaluation of Precipitation Forecasts by Polarimetric Radar

Monika Pfeifer

---



München 2007



# Evaluation of Precipitation Forecasts by Polarimetric Radar

**Monika Pfeifer**

DLR – Oberpfaffenhofen  
Institut für Physik der Atmosphäre  
D - 82234 Weßling

Dissertation  
der Fakultät für Physik  
der Ludwig - Maximilians - Universität München

Oberpfaffenhofen 2007

Gutachter der Dissertation:

Prof. Dr. U. Schumann  
Prof. Dr. S. Crewell

Tag der mündlichen Prüfung: 4. Mai 2007

Wer sie nicht konnte,  
Die Elemente,  
Ihre Kraft  
Und Eigenschaft,  
Wäre kein Meister  
Über die Geister.

*Johann Wolfgang von Goethe  
Faust I, Studierzimmer*

# Contents

<b>Abstract</b>	<b>iii</b>
<b>Zusammenfassung</b>	<b>iv</b>
<b>1 Introduction</b>	<b>1</b>
<b>2 Microphysics of Precipitation</b>	<b>6</b>
2.1 Theory . . . . .	6
2.1.1 Microphysical Processes . . . . .	6
2.1.2 Precipitating Hydrometeor Types . . . . .	7
2.2 Representation in NWP Models . . . . .	12
2.2.1 Concepts of Microphysical Parameterizations . . . . .	12
2.2.2 Mesoscale Models . . . . .	15
2.3 Observation by Polarimetric Radar . . . . .	19
2.3.1 Radar Detection of Precipitation . . . . .	20
2.3.2 Polarimetric Radar Quantities . . . . .	22
<b>3 Synthetic Polarimetric Radar</b>	<b>28</b>
3.1 Concept of a Polarimetric Radar Forward Operator . . . . .	29
3.2 Calculation of the Polarimetric Quantities . . . . .	31
3.3 Calculation of the Complex Dielectric Constant . . . . .	33
3.4 Beam Propagation . . . . .	35
3.5 Attenuation . . . . .	38
3.6 Interpolation of the Observations . . . . .	39

<b>4</b>	<b>Linking SynPolRad to the NWP Model</b>	<b>41</b>
4.1	Input Parameters for Rain . . . . .	42
4.2	Sensitivities of Polarimetric Quantities to Microphysical Properties of Ice . .	43
4.3	Determination of the Free Parameters for Ice . . . . .	46
4.4	Melting Ice and Brightband Effects . . . . .	49
4.5	Evaluation of SynPolRad . . . . .	51
<b>5</b>	<b>Stratiform Case Study – 5 July 2005</b>	<b>59</b>
5.1	Synoptic Overview, Observations, and Model Configuration . . . . .	60
5.2	Evaluation of the Life Cycle and Intensity . . . . .	60
5.3	Vertical Profiles . . . . .	71
5.4	Discussion . . . . .	74
<b>6</b>	<b>Convective Case Study – 12 August 2004</b>	<b>76</b>
6.1	Synoptic Overview, Observations, and Model Configuration . . . . .	77
6.2	Evaluation of the Life Cycle and Intensity . . . . .	78
6.3	Volume Scans and Vertical Profiles . . . . .	84
6.4	Evaluation of the MesoNH . . . . .	96
6.5	Discussion . . . . .	101
<b>7</b>	<b>Conclusions and Outlook</b>	<b>104</b>
<b>A</b>	<b>Technical Specifications of POLDIRAD</b>	<b>109</b>
<b>B</b>	<b>The T-Matrix Method</b>	<b>110</b>
<b>C</b>	<b>SynPolRad Parameters</b>	<b>113</b>
	<b>Symbols</b>	<b>115</b>
	<b>Abbreviations</b>	<b>117</b>
	<b>Acknowledgements</b>	<b>128</b>
	<b>Curriculum Vitae</b>	<b>129</b>

# Abstract

Over the last years, weather services have developed a new generation of high resolution mesoscale numerical weather prediction (NWP) models with the aim to explicitly predict convection. New methods are required to validate the representation of precipitation processes in these NWP models against observations. Polarimetric radar systems are especially suited for model validation as they provide information on the intensity and the microphysical characteristics of a precipitation event at a high temporal and spatial resolution. However, the observations can not be directly employed for model evaluation as polarimetric radar systems do not explicitly measure the parameters represented in microphysical parameterization schemes.

In order to establish a relationship and allow for a direct comparison between the model parameters and the observations, the polarimetric radar forward operator SynPolRad (Synthetic Polarimetric Radar) has been developed. SynPolRad simulates synthetic polarimetric radar quantities out of model forecasts which permits an evaluation in terms of observed quantities. In a first step, the synthetic reflectivity,  $L_{DR}$ , and  $Z_{DR}$  are computed from predicted bulk water quantities and in a second step, the beam propagation in the model domain is simulated under consideration of refractivity and attenuation effects. In order to successfully employ SynPolRad for model evaluation purposes, the link between the forward operator and the mesoscale model has to conform as closely as possible to the model assumptions. However, in the case of a polarimetric radar forward operator not all the input parameters are defined by the model. Within this work, these free parameters are derived on theoretical terms accordingly to the model assumptions such that the polarimetric quantities match the thresholds of a hydrometeor classification scheme. Furthermore, special care is given to the representation of brightband signatures.

The application of SynPolRad on two case studies proves the potential of the new method. A stratiform and a convective case study are chosen to assess the ability of mesoscale models to represent precipitation in different dynamical regimes. LMK (Lokal-Modell-Kürzestfrist) and MesoNH (Mesoscale Non-Hydrostatic Model) simulations considering different microphysical parameterization schemes are evaluated. The evaluation concentrates on the representation of life cycle, intensity, and the spatial distribution of synthetic reflectivity,  $L_{DR}$ , and  $Z_{DR}$ . Furthermore, hydrometeor types derived from the observed and synthetic polarimetric quantities employing a classification scheme are compared. Large discrepancies are found between the model simulations and the observations. However, the consideration of an additional ice hydrometeor category in the 3 component scheme significantly improves the performance of the LMK.

# Zusammenfassung

Um eine bessere Vorhersage von konvektiven Niederschlagsereignissen zu ermöglichen, wurde in den letzten Jahren eine Reihe von neuen, mesoskaligen Wettervorhersage-Modellen entwickelt. Dazu wurde die räumliche Auflösung der Modelle verfeinert und weitere Kategorien gefrorener Hydrometeore in den mikrophysikalischen Parameterisierungsschemata berücksichtigt. Um die Beschreibung der physikalischen Prozesse auf den kleinsten Skalen zu bewerten, müssen neue Verifikationsmethoden entwickelt werden, die sich auf Beobachtungen mit vergleichbarer zeitlicher und räumlicher Auflösung stützen. Das einzige Fernerkundungsinstrument, das hochaufgelöste Informationen über die Intensität und die mikrophysikalischen Charakteristiken eines Niederschlagsereignisses liefern kann, ist polarimetrisches Radar. Eine direkte Bewertung von Niederschlagsvorhersagen durch polarimetrische Radardaten ist allerdings nicht möglich, da die beobachteten Größen nicht explizit im Modell repräsentiert sind.

Um dennoch polarimetrische Radardaten zur Modellevaluierung zu verwenden, wurde der polarimetrische Radarwärtsoperator SynPolRad (Synthetisches Polarimetrisches Radar) entwickelt. SynPolRad simuliert synthetische, polarimetrische Radarmessungen aus Modellvorhersagen und erlaubt dadurch eine direkte Bewertung der Vorhersagegüte in denselben physikalischen Größen. Dazu werden zunächst die synthetischen Reflektivitäten,  $L_{DR}$  und  $Z_{DR}$  berechnet und dann die Ausbreitung des Radarstrahls im Modellraum unter Berücksichtigung der Refraktion und der Dämpfung simuliert. Um einen Vorwärtsoperator erfolgreich anwenden zu können, sollten alle Eingangsparameter vom Vorhersagemodell bestimmt werden. Allerdings hängen polarimetrische Radargrößen stark von den mikrophysikalischen Charakteristika der Hydrometeore ab, die im Vorhersagemodell nicht explizit beschrieben werden. Der Einfluß der einzelnen Eingangsparameter auf die synthetischen, polarimetrischen Radargrößen wurde durch Sensitivitätsstudien untersucht. Die Ergebnisse der Sensitivitätsstudien erlaubten es, die nicht spezifizierten Eingangsparameter unter Berücksichtigung der Modellannahmen so zu definieren, dass die synthetischen, polarimetrischen Größen  $L_{DR}$  und  $Z_{DR}$  immer im Bereich der Werte der entsprechenden Hydrometeorklassifikation liegen. Zusätzliche Annahmen wurden gemacht, um die typischen Signaturen in der Schmelzschicht wiederzugeben.

SynPolRad wurde zur Bewertung verschiedener Modellkonfigurationen auf eine stratiforme und eine konvektive Fallstudie angewendet. Die Bewertung konzentrierte sich auf die Wiedergabe des Lebenszyklusses, der Intensität und der räumlichen Verteilung von synthetischer Reflektivität,  $L_{DR}$  und  $Z_{DR}$ . Außerdem wurde die Niederschlagsklassifikation aus den beobachteten und synthetischen, polarimetrischen Radargrößen abgeleitet und verglichen. Die Bewertung ergab große Unterschiede zwischen den simulierten und den beobachteten Größen. Allgemein kann aber festgestellt werden, dass die Berücksichtigung einer zusätzlichen Eishydrometeor-Kategorie die Vorhersagequalität deutlich verbessert hat.



# Chapter 1

## Introduction

The weather element with the largest impact on the perception of forecast quality in the society is the amount of precipitation that will fall over a given area in a given period of time. However, a good quantitative precipitation forecast (QPF) is not only of relevance to citizens planning their spare time activities but there is a growing demand from industry, agriculture, and many other sectors for more detailed precipitation predictions. Furthermore, QPF is a prerequisite of improving forecasts of high-impact weather events such as severe storms or floods, and therefore strongly affects daily decisions in governmental activities proving the need for major advances in the quantitative precipitation forecast.

Although further developments of meteorological forecasting methods and observation systems have constantly enhanced the quality of short-range (up to 3 days) and medium-range (up to 10 days) weather forecasts for parameters like temperature and wind in the past years, quantitative precipitation forecasts generally have not shown corresponding improvements (Fritsch et al. (1998), Ebert et al. (2003)). This is partially due to the high sensitivity of the precipitation forecast on the model's predicted atmospheric and surface conditions where a good rain forecast strongly suggests a good forecast of all other atmospheric variables while a bad rain forecast can result from a number of errors including the treatment of precipitation in the model. The dependence on correct dynamical forcing is underlined by the fact that the skill of QPF is higher during winter when the precipitation is mainly stratiform and associated with synoptic scale systems which are normally well captured by the models. During the warm season however, most of the significant precipitation events are associated with convection for which operational models tend to perform poorly (Droegemeier et al. (2000), Ebert et al. (2003)). Thus, to improve especially the short range forecasts of precipitation, the understanding of convection and the representation of convective events in numerical weather prediction (NWP) models must be enhanced (Fritsch et al. (1998)). This is especially important as convective activity is often related to high-impact weather events.

In order to provide better forecasts at the convective scale, the national weather services are currently developing a new generation of mesoscale models operating at a horizontal resolution of only some kilometers and a forecast horizon of up to one day with the aim to explicitly resolve convection. Examples for this new generation of mesoscale NWP models

are the German model LMK (Lokal-Modell-Kürzestfrist, Doms and Förstner (2004)), the French model AROME (Bouttier (2005)), and the American WRF model (Skamarock et al. (2005)) which are about to become operational in the near future. However, refining the grid spacing of NWP models only improves QPF, if also the implemented model physics and especially the microphysical parameterizations are adapted to the finer resolution. Microphysical parameterization schemes have been identified by a number of studies as a principal source of error and especially the formation and distribution of precipitation has been found to extremely depend on the treatment of the ice phase hydrometeors in the model (e. g. Ferrier et al. (1995), Gilmore et al. (2004), Colle et al. (2005), Garvert et al. (2005)). The sensitivity to microphysical parameterizations will become even more important as more and more detailed storm structures are simulated because the microphysical processes are known to feed back onto the dynamics of the storm through the formation of heavily rimed ice hydrometeors as graupel and hail (Brandes et al. (2006)). Thus, a realistic simulation and forecast of convection regarding its intensity and life cycle strongly depends on the capability of the microphysical parameterization scheme to realistically represent the microphysical processes describing the formation and decomposition of the different hydrometeor types as well as their interaction.

While the high spatial resolution of NWP models is a prerequisite for an explicit description of clouds and microphysical processes, improvements in QPF can only be expected if appropriate methods for initialization and verification based on observations at comparable temporal and spatial scales become available. The operational verification of quantitative precipitation forecasts from mesoscale models is mostly based on comparisons of the model output averaged over a day and measurements from rain gauge networks. Although this data provides the most reliable information on the quantitative precipitation at the ground, no information about the temporal and spatial distribution of the precipitation in the atmosphere can be given. The potential of radar observations for the evaluation of high-resolution model forecasts was shown by Keil (2000) and Keil et al. (2003). Employing empirical formulas relating the reflectivity to the predicted precipitation, synthetic radar observations were derived that were compared to observations. Weather services are starting to use radar reflectivities for operational forecast verification and data assimilation because these are able to give routinely multi-dimensional information on relevant temporal and spatial scales. Even more information is provided by polarimetric radar which in contrast to conventional radar yields an enhanced data quality, better quantitative precipitation estimates, and additional information on the microphysical properties of the observed hydrometeors. Furthermore, combining the information content of the different polarimetric radar quantities offers the unique possibility of classifying the predominant hydrometeor type within the resolution volume (e. g. Höller et al. (1994), Vivekanandan et al. (1999), Zrníc et al. (2001)) which has been confirmed during the Joint Polarization Experiment (Ryzhkov et al. (2005)). Therefore, polarimetric radar systems provide an excellent tool for the investigation of severe weather events as they are able to observe the microphysical processes and dynamical developments simultaneously at high spatial and temporal resolution (Meischner et al. (2004)). As several countries are starting to incorporate polarimetric radar technology into their radar networks (e. g. Germany, France (Gourley et al. (2006)), Switzerland (Friedrich et al. (2006)), and the United States (Ryzhkov et al. (2005))), new methods have to be developed to fully exploit

---

the information content provided by polarimetric radar systems to improve QPF.

Over the last years, the potential of polarimetric radar observations for the verification and improvement of NWP models and especially microphysical parameterization schemes has been stressed by several authors (e.g. Fritsch et al. (1998), Vivekanandan et al. (1999), Droegemeier et al. (2000), Zhang et al. (2006), Brandes et al. (2006)). However, polarimetric observations do not provide explicit measurements of the parameters represented in microphysical equations or parameterizations and, therefore, no direct relationship between the observations and the model simulations exists. In order to employ nevertheless polarimetric radar data for model verification and assimilation, procedures must be developed that relate the observations to cloud physical quantities explicitly predicted by the NWP models (Fritsch et al. (1998), Droegemeier et al. (2000)).

In the literature, two possibilities coexist for the model evaluation using observations that are not directly linked to the model parameters. Either the observations are converted into model variables (observation-to-model approach) or synthetic observables are simulated from model output allowing comparisons in terms of the observed quantities (model-to-observation-approach, e.g. Chevallier and Bauer (2003)). In the context of model evaluation, the model-to-observation approach is generally preferred as it involves fewer assumptions and allows the full exploitation of the information content of the remote sensor. However, for this method a so called 'forward operator' has to be developed that transforms the model output into the variables of the remote sensing instrument to perform comparisons in terms of observables. This forward operator can be understood as a virtual remote sensing instrument in the model domain simulating synthetic observations from the model predictions. The advantage in the development of a forward operator is that its adjoint can be directly employed for the assimilation of the observed data.

Recently, forward operators were presented to calculate radar reflectivities from model forecasts for evaluation purposes. Haase and Crewell (2000) developed the RadarSimulations-Modell (RSM) based on model output by the LM which currently is employed for operational validation at the German weather service (Deutscher Wetterdienst (DWD)) and the Finnish Weather Service while MeteoFrance uses a similar tool presented by Caumont et al. (2006). In contrast to the work by Keil et al. (2003) where synthetic reflectivities were derived from model forecasts using empirical formulas relating reflectivity and the rain and snow water content, these forward operators compute the scattering processes explicitly employing Rayleigh or Mie theory and also consider propagation effects of the radar beam in the model domain. In the case of polarimetric radar data, first assimilation experiments employing empirical formulas to introduce the observations into the NWP models were carried out (Jung et al. (2005)). The study concentrated on the liquid phase and the authors found improved model skill but concluded that higher sophisticated polarimetric radar forward operators based on radar scattering models and T-Matrix methods (Waterman (1969)) were needed to derive more accurate relationships between the model parameters and the observed polarimetric quantities.

The development of a polarimetric radar forward operator for model evaluation purposes

forms the main objective of this thesis. This is accomplished by combining the experience of polarimetric radar modeling using T-Matrix calculations (e. g. Chandrasekar and Bringi (1987), Vivekanandan et al. (1990), Dölling (1997)) with the conventional radar forward operator RSM. The new polarimetric radar forward operator SynPolRad (Synthetic Polarimetric Radar) transforms the bulk water quantities of the different hydrometeor species prognosed by the NWP model into polarimetric radar variables as if operating a synthetic polarimetric radar in the model domain. The application of SynPolRad allows for a direct comparison of model generated polarimetric quantities to the observations by the DLR polarimetric diversity Doppler radar POLDIRAD (Schroth et al. (1988)) assessing the physical realism of the predicted precipitation structures. The intensity of the precipitation event is evaluated comparing the synthetic reflectivities to the observed ones while the polarimetric quantities give further information about the microphysical properties of the predominant hydrometeor type within the resolution volume.

Up to now, most publications studying the impact of polarimetric radar data on model skill concentrated on the liquid phase (e. g. Jung et al. (2005), Brandes et al. (2006)) due to the relatively simple relationships between the microphysical characteristics of rain and the corresponding polarimetric quantities. In the ice phase, the derivation of relationships between model parameters and observables results much more difficult. The representation of ice phase hydrometeors in the NWP models is only a crude simplification of the natural variability in densities, dielectric constants, shapes, and falling behaviour depending on the hydrometeor type while the observations are highly sensitive to these microphysical characteristics of the precipitation. Therefore, there is a mismatch between the information content of the NWP model and the polarimetric radar data which inhibits a direct relationship. However, within the development of SynPolRad, the ice phase will be explicitly considered as this is of major importance to fully assess the forecast ability of the NWP model.

The development and application of a polarimetric radar forward operator constitutes the first method to evaluate microphysical parameterization schemes not only by point measurements during intensive observation periods and experiments but also for longer time periods employing routine measurements. The advantages of this method are in the ability to assess the spatial and temporal distribution of precipitation intensity and precipitation type in the model, the possibility for long term evaluations, and the reduced costs as compared to aircraft observations. Furthermore, the development of the polarimetric radar forward operator SynPolRad provides the first step towards a future assimilation of polarimetric radar data.

Before the development of the polarimetric radar forward operator will be discussed, Chapter 2 provides the theory of precipitation formation and a summary of the microphysical characteristics of the different precipitating hydrometeor types. This introduction will be completed by a discussion of the state of the art of the representation of these processes in NWP models and their observation using polarimetric radar. In Chapter 3, the single components of the polarimetric radar forward operator will be introduced with a special focus on the simulations of polarimetric radar quantities using the T-Matrix approach. Furthermore, aspects regarding the modeling of the dielectric constant as well as propagation effects of the radar beam in the model domain will be introduced. In order to allow a successful evaluation of the model physics employing a forward operator, the link between the model and the

forward operator has to conform as closely as possible to the model assumptions. Chapter 4 summarizes the aspects regarding the interface of the polarimetric radar forward operator to the NWP model and tries to give an evaluation of its performance and capabilities. After the successful implementation and evaluation of the polarimetric radar forward operator, the tool will be employed for assessing the forecast capabilities of the NWP models regarding the representation of precipitation for different precipitation regimes. Chapter 5 focuses on a stratiform case study while the discussion in Chapter 6 concentrates on a convective event. The evaluation will be performed for different models and microphysical parameterizations schemes and the discrepancies arising from the different model configurations will be discussed.

The thesis concludes with a summary of the main results regarding the development of the polarimetric forward operator as well as the performance of the NWP models (Chapter 7). Furthermore, recommendations for the future model evaluation and a better representation of microphysical processes in NWP models will be given.

# Chapter 2

## Microphysics of Precipitation

The physical processes responsible for the formation and decay of clouds and precipitation are very complex and highly variable. Depending on the local thermodynamic conditions, different microphysical mechanisms prevail and lead to the development and growth of the corresponding hydrometeor types which influence and determine the nature, strength, and life cycle of the precipitation event. These processes are strongly interactive and also feed back on the dynamics, thermodynamics, and chemistry of the ambient air. In this section, the different microphysical processes of clouds and precipitation formation will be introduced and the main characteristics of the most important precipitating particle types will be discussed. The following section focuses on the representation of these processes in mesoscale NWP models. In the last section, the capabilities of observing these processes by polarimetric radar will be discussed.

### 2.1 Theory

#### 2.1.1 Microphysical Processes

Cloud processes are the result of the atmosphere trying to bring its thermodynamic state into equilibrium. If an air parcel becomes saturated because of adiabatic or diabatic cooling or mixing processes, small drops form when water molecules change from the gaseous to the liquid phase (**nucleation**). The newly formed water drop is unstable unless it reaches a critical diameter where the energy necessary to maintain the surface tension is smaller or in equilibrium with the energy liberated by the phase change. This critical radius is a strong function of relative humidity. The stronger the supersaturation of the air, the smaller the radius of the drop that must be exceeded can be. In the atmosphere, water drops form by **heterogeneous nucleation** with an aerosol particle acting as a **cloud condensation nucleus** (CCN). This reduces the energy needed for the process due to the higher probability of reaching the critical radius. For homogeneous nucleation by water drops theoretical values of supersaturation of 300 - 400 % would be required which do not occur in the atmosphere. The closer the chemical structure of the aerosol particle is to water, the less energy is needed for the nucleation process and can be further decreased if the aerosol is dissolvable in water.

Availability, chemical structure, and size distribution of CCNs have, therefore, a large effect on cloud formation in the atmosphere.

Once the drop exists, it can grow further by diffusion of water vapor from the air to the drop (**condensation**). The contrary process when water molecules diffuse from the drop to the air is called **evaporation**. During condensation latent heat is released from the drop to the surrounding air which has to be provided in the case of evaporation by the atmosphere. The two processes depend on the size of the single drops and the thermodynamics of the surrounding air and combine to provide thermodynamic equilibrium between the gaseous and solid phase.

Growing drops reach the point where their fall velocity is not any more negligible and particles leave the volume through **sedimentation**. The terminal falling velocity is a function of the drop diameter and is reached when the gravitational forces are balanced by the frictional forces. Drops with different diameters reach, therefore, different terminal sedimentation speeds and larger drops descending faster can collide and unite with smaller drops during their fall. This process is called **coalescence** and is an important process in the formation of the typical rain drop spectrum. During fall, large drops can become unstable because of internal oscillations generated by the interaction of the drop surface with the surrounding air. This can lead to a **break up** in smaller drops and gives an upper bound for the maximum drop diameter.

Similar to the liquid phase, ice crystals form by **heterogeneous nucleation** and grow by diffusion of ambient vapor towards the particle through **deposition**. The shape or habit adopted by an ice crystal growing by vapor diffusion is a sensitive function of the temperature and supersaturation of the air. The loss of mass of an ice particle by diffusion of vapor from the surface to the environment is called **sublimation**. Similar to coalescence, ice particles can collect other ice particles (**aggregation**) and form aggregates. Aggregation depends strongly on temperature, as the ice particles become 'sticky' for temperatures higher than  $-5^{\circ}\text{C}$  enhancing the collection efficiency. In the case that ice crystals collect liquid drops, this process is called **riming**. The different microphysical processes form a temporal sequence where nucleation precedes diffusion growth which precedes growth by collection. Measurements of ice particles within clouds often show larger particle number concentrations than would be expected for the typical concentrations of activated ice nuclei. This **ice enhancement** is believed to be due to ice fragmentation or splintering. In contrast to water drops, the terminal fall speed is more complicated to determine because it is not only a function of diameter but also depends on the particle shape, its riming degree, and its density. Ice hydrometeors falling beneath the  $0^{\circ}\text{C}$  isotherm start to **melt** and strongly alter the environmental conditions by a significant removal of latent heat. In general, every phase change is accompanied by release or removal of latent heat to or from the surrounding air. This is a prominent feedback mechanism which alters the thermal stratification within the cloud and may intensify the vertical motions due to an increase in buoyancy.

### 2.1.2 Precipitating Hydrometeor Types

A number of physical properties of a precipitation event can be described by the spectrum of precipitating particles as a function of diameter which is called the drop size distribution

(DSD) or particle size distribution (PSD). This spectrum results from the interaction of the different microphysical processes discussed previously. It strongly impacts on the further development of the cloud because most microphysical processes are highly dependent on the particle size and shape.

As a consequence of the variety of microphysical processes involved in precipitation formation, a large number of hydrometeor types exists where the differences are largest between the liquid and solid phase. While for rain the drop shape is the only parameter that changes as a function of diameter (see Equation 2.1), ice hydrometeors exist in a variety of shapes and densities depending on the prevailing growth processes. Differences in crystal shapes arise from the dependence of crystal habit on temperature and supersaturation and from the riming and aggregation of crystals in different dynamical regimes. Heavily rimed ice crystals and graupel particles can indicate convection whereas pristine ice crystals and large snowflakes are present in stratiform precipitation regions.

These parameters can assume a wide range of values which makes it particularly difficult to determine remotely the microphysical properties of the precipitating particles. This is also shown in the relatively small number of literature on ice hydrometeors where almost no recent studies are available and most of the related studies come from the 1980's. Furthermore, the classification of ice hydrometeor types is arbitrarily and the smooth transition between the different ice hydrometeors makes it difficult to define typical characteristics. In the initial stages of riming as long as the features of the original ice crystal are still well distinguishable, the ice particle is generally called a lightly or densely rimed snow crystal. When riming of an ice particle has proceeded to the stage where the features of the primary ice particle are only faintly or no longer visible, the ice particle is called a graupel particle. In the case of densely rimed ice, a particle is called a hail stone when its maximum dimension is larger than 5 mm. In the following the main characteristics of the most important precipitating hydrometeor types will be discussed.

## Rain

A rain event consists of a great number of drops with different diameters, shapes, and terminal falling velocities. During fall large rain drops become increasingly oblate because of the interactions of the drop with the surrounding air trying to balance surface tension, hydrostatic pressure, and aerodynamic pressure due to the air flow around the drop (Pruppacher and Klett (2003)). There are several publications studying the shape dependence of rain drops on theoretical terms (Green (1975)), using wind tunnel experiments (Pruppacher and Beard (1970)), numerical models (Beard and Chuang (1987), Chuang and Beard (1990)) or aircraft measurements (Chandrasekar et al. (1988)). The most popular formulation is given by Andsager et al. (1999) who derived an empirical model from observations giving the axis ratio  $\alpha$  as a simple function of diameter  $D$  and reproducing well the observations from this and previous publications:

$$\alpha = 1.012 - 0.144D - 10.3D^2. \quad (2.1)$$

This formulation is valid for drops with diameters smaller than 4.4 mm. For larger drops the axis ratio remains uncertain because of the internal circulation of drops at that size which makes measuring and defining an equilibrium axis ratio very difficult. The DSD of rain drops

is truncated at both ends of the spectrum. The reason at the upper end is that large drops are hydrodynamically unstable (even at laminar flow (Pruppacher and Klett (2003))) and tend to break up in smaller drops or are destroyed by collisional break up. These processes generally limit the drop diameter to less than 2 to 3 mm. As for the small diameters, the spectrum of rain begins where the drops have a notable falling velocity against the updrafts in the cloud. Wind tunnel experiments as well as field experiments show that drops for which the flat lower side is parallel to the ground during fall in quiet air tilt in the presence of shear. The mean canting angle is small: on the order of  $0 - 4^\circ$  with a standard deviation of up to  $20^\circ$  (Beard and Jameson (1983), Chandrasekar et al. (1988), Huang et al. (2001)). Both, the shape and sedimentation speed of a given rain drop only depend on its diameter  $D$  and, therefore, a rain event can be completely described by its DSD. The spectrum of rain drops is highly variable in time and space because of the different microphysical processes discussed previously and the different scales and drop sizes interacting (Lee and Zawadzki (2005)). Although this complicates a general theory, there are different formulations of DSD as a function of equivalent diameter. The equivalent diameter was introduced to formulate the DSD in terms of the water equivalent independently of the shape dependence of a drop and is defined as the diameter of a sphere with the same volume as the deformed drop. The most widely used formulation of the DSD of rain as a function of equivalent diameter is the Marshall-Palmer distribution (Marshall and Palmer (1948)) describing the spectrum of rain drops as a simple exponential distribution with a fixed intercept parameter  $N_o = 8000 \text{ mm}^{-1} \text{ m}^{-3}$ :

$$N(D) = N_o \exp(-\lambda D). \quad (2.2)$$

where  $N(D)$  is the total number of particles. The slope  $\lambda$  [ $\text{mm}^{-1}$ ] of the distribution is a function of rain rate  $R$  [ $\text{mm h}^{-1}$ ] and is defined by Marshall and Palmer (1948) as  $\lambda = 4.1 R^{-0.21}$ . As a further parameter characterizing the DSD of rain, the median diameter  $D_o$  was introduced by Atlas (1953) as the diameter where the liquid water content distribution is divided into equal parts. This defines  $\lambda$  as  $D_o = 3.75/\lambda$ .

A number of more detailed studies have demonstrated that the Marshall-Palmer distribution is not general enough to deal with the great variety of rain drop spectra especially because of the fixed intercept parameter  $N_o$  (e. g. Sekhon and Srivastava (1971), Pruppacher and Klett (2003)). There are other concepts of distribution functions that try to account for these deficiencies as e. g. the gamma distribution (Ulbrich (1983)), the lognormal distribution (Feingold and Levin (1986)), or the normalized distribution (Sempere-Torres et al. (1994), Testud et al. (2001)) describing different precipitation regimes better by using a third parameter to fix the DSD.

Different important rainfall parameters  $P$  are related to moments  $p$  of the DSD (Ulbrich (1983))

$$P = a_p \int_0^\infty D^p N(D) dD. \quad (2.3)$$

These are the radar reflectivity factor assuming the Rayleigh approximation ( $p = 6$ ), the rain rate ( $p = 3.67$ ), and the liquid water content ( $p = 3$ ). The coefficients  $a_p$  and the exponents  $p$  are summarized in Table 2.1.

$P$	$p$	$a_p$
Radar Reflectivity Factor [ $\text{mm}^6 \text{m}^{-3}$ ]	6	$10^6 \text{mm}^6 \text{cm}^{-6}$
Liquid Water Content [ $\text{g m}^{-3}$ ]	3	$0.524 \text{g cm}^{-3}$
Rain Rate [ $\text{mm h}^{-1}$ ]	3.67	$33.31 \text{mm h}^{-1} \text{m}^3 \text{cm}^{-3.67}$

**Table 2.1:** Coefficients  $a_p$  and exponents  $p$  for the description of rainfall parameters  $P$  as moments of the drop size distribution (Ulbrich (1983)).

## Snow

Observations show that snow crystals appear in a large variety of shapes from single pristine crystals to complex aggregates. Different growth regimes (Magono and Lee (1966), Mason (1994)) are favored depending on the prevailing thermodynamic conditions of the surrounding air. Figure 2.1 shows typical crystal types for different temperature and humidity conditions (Magono and Lee (1966)). At a large vapor density excess or supersaturation with respect to ice, the snow crystal shape changes with decreasing temperature from a needle to a column, to a plate, to a sector plate, to a dendrite, back to a sector plate, and finally back to a column. At temperatures where plate-like crystals appear, increasing supersaturation causes transitions from a very thick plate to a thick plate, to a sector plate, to finally a dendrite.

Observations have shown further, that the thickness and diameter of plate-like crystals, and

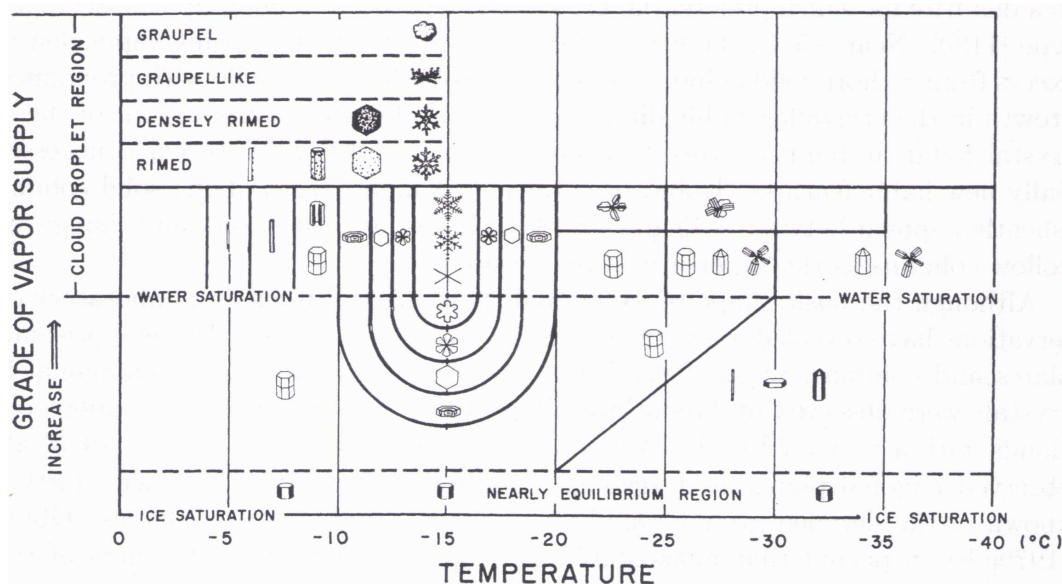


**Figure 2.1:** Temperature and humidity conditions for the growth of natural snow crystals of various types (Magono and Lee (1966)).

the length and width of columnar crystals are characteristically related to each other. With increasing diameter of plate-like crystals their thickness increases and with increasing length of columnar crystals also their width increases (Pruppacher and Klett (2003)). Observed 1-

dimensionally growing particles (needles) and 2-dimensionally growing particles (dendrites) show a different axis ratio behavior. The axis ratio of the observed 2-dimensionally growing particles remains constant for all sizes whereas 1-dimensionally growing particles show a decreasing axis ratio with size (Scheffold et al. (2002)). When certain conditions prevail in a cloud, snow crystals collide to form snowflakes which are conglomerates of ice crystals and usually have complex irregular shapes. Air temperature (i.e. temperature near 0° C) and snow crystal shape play the dominant roles in such aggregation. In the case of snowflakes there is a general decrease of the axis ratio with increasing size with the mean axis ratios being between 1 and 0.6 (Barthazy and Scheffold (2004)).

Most ice crystals have a bulk density less than that of ice which is due to small amounts of air in capillary spaces and to the tendency of snow crystals to grow in a skeletal fashion. Larger dimensions are often correlated with lower bulk densities. The density of snow flakes typically ranges between 0.005 and 0.5 g cm<sup>-3</sup> with the most frequent values ranging between 0.01 and 0.2 g cm<sup>-3</sup> (Pruppacher and Klett (2003)).

Gunn and Marshall (1957) proposed a particle size distribution for snow analogous to the Marshall-Palmer distribution for rain:

$$N(D) = N_o \exp(-\lambda D), \quad (2.4)$$

with  $N_o = 3800 R^{-0.87}$  and  $\lambda[\text{cm}^{-1}] = 25.5 R^{-0.48}$ . In case of snow,  $D$  is the equivalent diameter of the water drop to which the snow crystal would melt and  $R$  is the precipitation rate in mm h<sup>-1</sup> of water. Sekhon and Srivastava (1970) confirmed the power law but found different values for  $N_o$  and  $\lambda$  with  $N_o = 2500 R^{-0.94}$  and  $\lambda[\text{cm}^{-1}] = 22.9 R^{-0.45}$ .

## Graupel and Hail

A particle is called a graupel particle when riming has proceeded to the stage where the features of the original ice crystal are no longer visible. Rimed ice crystals and graupel are formed in clouds which contain both, ice crystals and supercooled drops. Such a particle has a white opaque and fluffy appearance due to the presence of a large number of air capillaries in the ice structure. An ice particle is called a small hail particle if it has originated as a frozen drop or ice crystal and has grown by riming to an irregular or roundish, semi-transparent particle of density 0.8 to 0.99 g cm<sup>-3</sup> (Pruppacher and Klett (2003)). In clouds with sufficiently large updrafts riming may continue until hailstones are produced which have by definition a diameter of 5 mm or more (e.g. Cheng et al. (1985)). Hailstones can also consist of spongy ice with large capillaries filled with water.

The bulk density of graupel particles varies greatly depending on the denseness of packing of the cloud drops frozen on the ice crystal from 0.05 to as high as 0.89 g cm<sup>-3</sup> (Pruppacher and Klett (2003)). Heymsfield (1978) found during in situ measurements with aircraft in north-eastern Colorado that graupel density is related to particle growth, temperature, accreted droplet sizes, environmental liquid water content, free-fall characteristics, and density of the ice particle from which the graupel particle originates. Conical graupel has a considerably higher density than lump graupel at small particle sizes ( $D < 3.5$  mm). The mean density of conical graupel is nearly constant at 0.45 g cm<sup>-3</sup> while the mean density of lump graupel increases with size. The bulk density of hailstones tends to vary radially from surface to core

with alternating concentric layers of lower and higher density. The density of such hailstone shells has been found to vary usually between 0.8 and 0.9 g cm<sup>-3</sup> (Pruppacher and Klett (2003)).

A variety of shapes has been observed for densely rimed particles including conical and oblate spheroidal shapes. Matson and Huggins (1980) found in several Colorado hail storms that the major part consisted of oblate spheroidal shapes. Regarding the axis ratio, Heymsfield (1978) differentiated between conical and lump graupel particles. For conical graupel, he found the axis ratios to range from 0.4 to 1.8 with increasing dimension while it ranged for lump graupel from 0.4 to 1. Barthazy and Schefold (2004) found an increase of axis ratio with increasing riming degree with graupel particles having the largest axis ratios of approximately 1 for all sizes. Regarding hail stones, Knight (1986) found a decreasing sphericity with increasing size with aspect ratios from 0.95 for dimensions of 1 – 5 mm to 0.6 for dimensions of 41 – 45 mm in Alberta hailstones while Oklahoma hailstones showed higher values from 0.95 – 0.7 for maximum dimensions of 51 – 55 mm. The normal falling behavior of moderate-to-large hailstones is rapid symmetrical tumbling. The tumbling behavior is critically sensitive to the surface roughness of the hail stone and its density distribution (Knight and Knight (1970)).

Cheng and English (1983) found that the particle spectra of graupel and hail particles are best fitted by an exponential distribution according to the exponential Marshall Palmer type:

$$N(D) = N_o \exp(-\lambda D), \quad (2.5)$$

with  $N_o = A\lambda^B$  and  $A$  and  $B$  varying strongly from storm to storm.

## 2.2 Representation in NWP Models

### 2.2.1 Concepts of Microphysical Parameterizations

In the previous section, the complexity and high degree of interaction of the various microphysical processes involved in cloud and precipitation formation have been discussed. These processes have to be represented in atmospheric prediction models in such a way that the general microphysical development is well reproduced without resolving all processes to the finest scales. Especially the use of numerical models in operational modes makes it necessary to find a balance between greater resolution and greater detail in the microphysical treatment and the related computational costs.

The smallest scales of physical processes that can be formulated in an explicit way are prescribed by the model resolution which in mesoscale models developed for operational use is in the order of some kilometers. All processes with time and spatial scales smaller than the model resolution can not be described explicitly and are, therefore, considered in parameterized form. A parameterization is an approximation to an unknown term by one or more known terms or factors. These factors are called parameters and are normally derived empirically from observations or calculations by explicit models. Numerical models usually include either diagnostic or prognostic parameterization schemes to represent clouds. In diagnostic schemes the parameters regarding clouds and precipitation are not prognosed explicitly but are diagnosed after each time step of integration from the other prognostic

parameters. Diagnostic schemes are computationally quicker but the clouds are largely divorced from the rest of the model because the interaction of clouds and precipitation with the other parameters is less direct. In prognostic mode budget equations for the precipitating hydrometeors are solved.

Microphysical parameterization schemes describe the evolution of the particle size spectra for different types of hydrometeors and, therefore, an accurate formulation of the PSD is essential. There exist two concepts of microphysical parameterization schemes – explicit bin-resolving or spectral cloud models (e. g. Rasmussen et al. (2002)) and bulk microphysical parameterization schemes (e. g. Lin et al. (1983)). In spectral models, the particle spectrum is divided in general in more than 20 size or mass bins. Within these specific intervals of the PSD, multiple variables are prognosed for each hydrometeor type. Theoretically, this is the more direct approach to represent cloud microphysics in a dynamical model because many microphysical principles can be applied directly to the calculation of the size distributions. However, it becomes very complex when the ice phase is considered. The detailed description of various crystal types including their interactions and their habit changes results in extreme costs in terms of computer time and memory. For this reason, spectral models are not yet available for real time NWP efforts though continued technological advances are likely to change this in the future.

Most models designed for realtime applications use so called bulk water parameterization schemes. Within these schemes, the various types of hydrometeors are grouped into several broad categories of water substance (e. g. cloud water and cloud ice, rain, snow, graupel, and hail) and conversions between the different classes are calculated in terms of mixing ratios in order to minimize the number of equations and calculations. The various categories are interactive, i. e., the increase of water mass due to a specific microphysical process in one category is at the expense of water content in another category. In the presence of phase changes such as condensation or evaporation, the potential temperature is recalculated. Figure 2.2 shows a conceptual view of the microphysical parameterization scheme of the German model LMK (Lokal Modell Kürzestfrist, see Section 2.2.2) considering 5 hydrometeor classes plus water vapor including all types of conversions between water categories as well as the loss of mass due to sedimentation.

The disadvantage of the bulk approach is in the formulation of the particle spectrum assuming that the prescribed functional form of the PSD remains valid throughout its different evolutionary stages and that the evolution of a few bulk variables is sufficient to describe the time dependence of the adjustable parameters of the PSD. Yet, in reality each process modifies the particle spectrum and their combination may be complex and leads to a large variability of the actual PSD in time and/or in space (Zawadzki et al. (1994)). Hence, the specification of a particular functional form necessarily puts artificial constraints on the conversion rates. This problem can be overcome by the prediction of more moments of the PSD to ensure that the minimum number of free parameters is sufficient to track the evolution of the particle spectrum well enough to achieve an acceptable accuracy of the quantities of interest. In double-moment schemes, the number density of particles in a water category is usually chosen as a second dependent model variable besides the mass fraction. Although, this increases drastically the computational costs compared to a single-moment scheme, because twice the number of prognostic variables and a much larger number of microphysical interactions have to be considered, this method is much cheaper than detailed spectral modeling while at the same time individual microphysical processes can be represented very

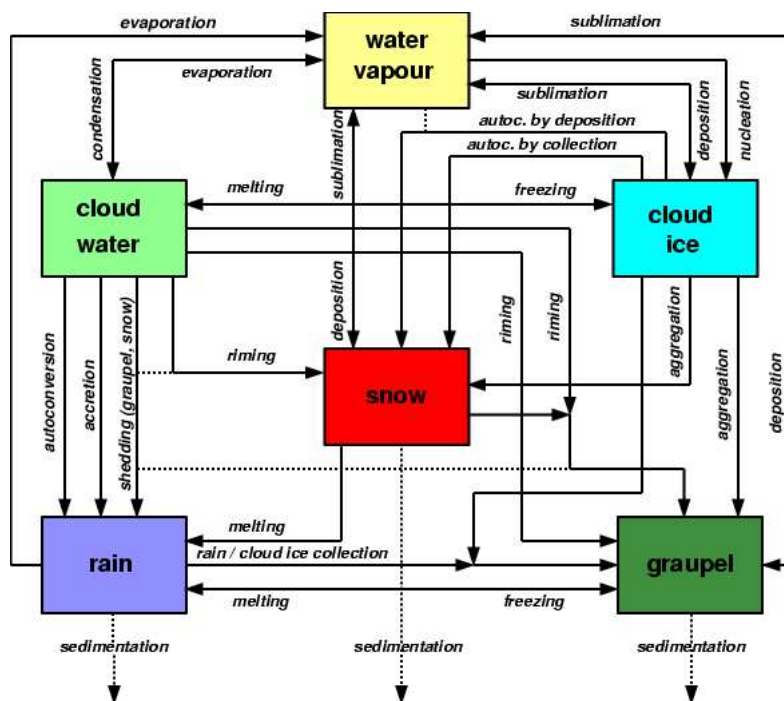


**Figure 2.2:** Conceptual view of the microphysical processes represented in the LMK 3 component ice scheme (Doms and Schättler (1999), see Section 2.2.2).

accurately.

The second problem lies in the description of the ice phase. Whereas liquid-phase particles can be assumed to be spherical drops the theoretical formulation of ice phase processes is complicated because of the wide variety of shapes and habits that ice crystals may assume. Usually, only a few categories of ice particles are taken into account and their shape parameters are prescribed. Therefore, neither the natural variety of ice particles nor their habit changes due to varying temperature or humidity conditions can be considered.

Since the first development of a bulkwater scheme by Kessler (1969) considering only warm cloud physics, a number of attempts were made to overcome these limitations by including more hydrometeor types and/or by predicting more moments of the DSD. Rutledge and Hobbs (1984), Lin et al. (1983), and Walko et al. (1995) expanded these first parameterization schemes by including ice physics with two, three, or five ice categories. Ferrier (1994) presented a 2-moment bulk scheme predicting the mixing ratios as well as the number concentrations for four categories of ice (cloud ice, snow, graupel, and frozen drops/hail). Furthermore, he considered the liquid water fraction during wet growth and melting for each of the precipitating ice species allowing for a more accurate calculation of radar products. Straka and Mansell (2005) presented a scheme with an emphasis on multiple ice categories in order to provide a smoother transition in physical characteristics including cloud droplets, rain, three habits of ice crystals, snow, graupel with three different densities, frozen drops, as well as small and large hail.

Model	Parameter	Rain	Snow	Graupel	Hail
LM	DSD	$N(D) = N_o \exp(-\lambda D)$			
	$N_o$	8000	800	4000	
	$\rho$	1	$m = 0.038 D^2$	0.2	
Thompson	DSD	$N(D) = N_o \exp(-\lambda D)$		$N(D) = N_o^g D^{(\nu-1)} \exp(-\lambda_g D)$	
	$N_o$	$f(q_r)$	$f(T)$	$f(q_g)$	
	$\rho$	1	0.1	0.4	
MesoNH	DSD	$N(D) = C \lambda^{X+1} \exp(-\lambda D)$			
	$N_o$	$N_o = C \lambda^X$			
	$\rho$	1	$m = 0.02 D^{1.9}$	$m = 19.6 D^{2.8}$	0.9

**Table 2.2:** Comparison of the assumptions regarding the assumed shape of the DSD, the intercept parameter  $N_o$  [ $\text{mm}^{-1} \text{m}^{-3}$ ], and the density  $\rho$  [ $\text{g cm}^{-3}$ ] of the different microphysical schemes. If no fixed density is assumed for an ice hydrometeor, the according mass-size relationship is given.

## 2.2.2 Mesoscale Models

In the following section, the different mesoscale models and microphysical parameterization schemes used within this work will be introduced with the focus on the different assumptions regarding the representation of hydrometeors. In mesoscale models, variables are normally given in SI-units whereas in theoretical studies as well as in radar meteorology units are often employed that are more directly connected to the physical meaning of the parameter and are, therefore, more illustrative. In order to facilitate the discussion, SI-units are only used in this section in equations directly taken from the literature or if explicitly declared. The assumptions of all microphysical parameterization schemes are summarized in Table 2.2 and the different particle size distributions for snow and graupel are illustrated in Figure 2.3.

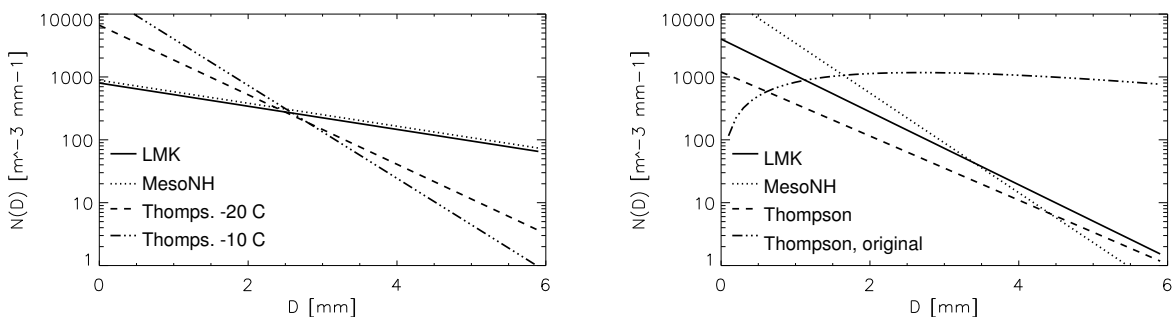


**Figure 2.3:** Particle size distributions for snow (left) and graupel (right) for the LMK, the Thompson scheme, and the MesoNH. The Thompson scheme assumes a temperature dependent intercept parameter  $N_o$  and, therefore, the PSD is given for  $-20^\circ \text{C}$  and  $-10^\circ \text{C}$ . Regarding graupel, the Thompson scheme is shown in its original version (Equation 2.13) and the formulation used within this study.

## Lokal-Modell

The non-hydrostatic Lokal-Modell (LM) (Doms and Schättler (1999)) together with the global model Global-Modell (GME) are the main instruments for the numerical weather prediction at the German weather service (DWD). This model chain is completed by the high resolution short range version of the LM, the Lokal-Modell-Kürzestfrist (LMK), which shall be run operationally in 2007.

The LM is a non-hydrostatic mesoscale model which is used operationally at a horizontal resolution of 7 km since December 1999. It has a generalized terrain-following vertical coordinate and the prognostic variables are the wind vector, temperature, pressure perturbation, specific humidity, cloud liquid water and cloud ice, as well as precipitation. The model incorporates a grid-scale cloud and precipitation scheme as well as a parameterization of moist convection. The LMK is operated at the moment in research mode at a horizontal resolution of 2.8 km using the same physical parameterization schemes as in the LM except that the parameterization of moist convection is switched off at this resolution.

The LMK includes two bulk water parameterization schemes based on the work by Lin et al. (1983) with different numbers of prognostic variables for ice species. The 2 component ice scheme has been developed originally for the LM with a horizontal resolution of 7 km focusing on a correct description of stratiform precipitation. It considers the mixing ratios of cloud water and cloud ice, rain, and snow as prognostic variables. In 2004, DWD introduced the 3 component scheme including graupel as a new frozen hydrometeor species in order to represent more realistically the cloud microphysical processes in explicitly resolved deep convection.

In the LM microphysical parameterization schemes, the particles of the different precipitating hydrometeor species  $x$  are assumed to be exponentially distributed with respect to drop respectively particle diameter  $D_x$  following Marshall and Palmer (1948):

$$N_x(D_x) = N_o^x \exp(-\lambda_x D_x). \quad (2.6)$$

For ice particles,  $D_x$  is the actual diameter of the ice particle in contrast to the equivalent diameter of the melted particle. The intercept parameters  $N_o^x$  are assumed to be constants derived empirically from observations. The slope  $\lambda_x$  of the DSD is related to the particle mixing ratio  $q^x$  [ $\text{kg kg}^{-1}$ ] via

$$\rho q^x = \rho_x \pi N_o^x \lambda_x^{-4}, \quad (2.7)$$

where  $\rho$  [ $\text{kg m}^{-3}$ ] is the density of the air,  $\rho_x$  the density of the hydrometeor, and  $N_o$  as well as  $\lambda$  are given in SI units, thus,  $\text{m}^{-4}$  and  $\text{m}^{-1}$ .

For rain,  $N_o$  is fixed at  $8000 \text{ mm}^{-1} \text{ m}^{-3}$  while for snow it is set to  $800 \text{ mm}^{-1} \text{ m}^{-3}$ . Snow is assumed to be in the form of densely rimed aggregates of dendrites with a maximum linear dimension  $D_s$ . Based on Locatelli and Hobbs (1974) the mass size relation of snow is approximated by

$$m_s = a_m^s D_s^2 \quad (2.8)$$

with the constant form factor  $a_m^s = 0.038 \text{ kg m}^{-2}$  and  $m_s$  being the mass of the particle.

Graupel is initiated from freezing of rain drops and from conversion of snow to graupel due to riming. Graupel density is assumed to be  $0.2 \text{ g cm}^{-3}$  and  $N_o$  is fixed at  $4000 \text{ mm}^{-1} \text{ m}^{-3}$  (Rutledge and Hobbs (1984)). For the mass-size relation of graupel particles the following power law is assumed (Heymsfield and Kajikawa (1987)):

$$m_g = a_m^g D_g^{3.1}, \quad (2.9)$$

where  $a_m^g = 169.6 \text{ kg m}^{-3.1}$ .

Reisner et al. (1998) presented a microphysical bulk parameterization scheme (known as option number 4 or Reisner 2 scheme) with the emphasis on ice microphysics developed for the American mesoscale model MM5 (PSU/NCAR Mesoscale Model, Grell et al. (1994)). This parameterization scheme predicts the mixing ratios of cloud water and ice, rain, snow, and graupel, as well as the number concentration of cloud ice. The DSD of the precipitating hydrometeors is approximated by an exponential distribution following Marshall-Palmer as in the LM schemes and also the equations for the calculations of the slope parameters  $\lambda_x$  are the same as in the LM. The intercept parameters of rain and graupel are fixed at  $8000 \text{ mm}^{-1} \text{ m}^{-3}$  and  $4000 \text{ mm}^{-1} \text{ m}^{-3}$ . In contrast to the LM, graupel density is fixed at  $0.4 \text{ g cm}^{-3}$ . Further differences to the LM can be found in the assumptions regarding snow. First, the snow density is fixed at  $0.1 \text{ g cm}^{-3}$  for all diameters and, second, the intercept parameter  $N_o^s$  varies with the snow mixing ratio  $q_s$  following the results from Sekhon and Srivastava (1970):

$$N_o^s = \left( 1.718 \left[ \frac{1}{\rho q_s \alpha} \left( \frac{\pi \rho_s}{\rho q_s} \right)^{b_s/4} \right]^{0.94} \right)^{\frac{4}{4-0.94b_s}}, \quad (2.10)$$

where  $1/\alpha = 6\rho_w/a_s\Gamma(4+b_s)$ .  $a_s$  and  $b_s$  are constants in the fall speed relationship for snow with  $a_s = 11.72 \text{ m}^{1-b_s} \text{ s}^{-1}$  and  $b_s = 0.41$  and  $\Gamma$  is the Gamma function.

Thompson et al. (2004) published a further development to the Reisner microphysical scheme which has been included in the LMK as a reference to test the performance of the LMK microphysical parameterization schemes. The Thompson scheme modifies the assumptions regarding the DSD of the different precipitating hydrometeors to adapt these to the meteorological situation. In order to describe drizzle accurately, the intercept parameter of rain is defined as a function of rain mixing ratio:

$$N_o^r = \left( \frac{N_1^r - N_2^r}{2} \right) \tanh \left[ \frac{4(q_{ro} - q_r)}{q_{ro}} \right] + \frac{N_1^r + N_2^r}{2}, \quad (2.11)$$

where  $N_1^r = 1 \times 10^{10} \text{ m}^{-4}$  is an upper limit and  $N_2^r = 8 \times 10^6 \text{ m}^{-4}$  is a lower limit for the intercept parameter  $N_o$ . For low rain mixing ratios, the intercept parameter and the slope of the DSD are increased such that the rain event consists mainly of small drizzle-size drops. For higher mixing ratios, the intercept parameter and the slope of the DSD decrease to the original values of the Marshall-Palmer formulation. In the formulation of rain DSD, the transition between these two regimes is defined to be at  $q_{ro} = 1 \times 10^{-4} \text{ kg kg}^{-1}$ .

The snow intercept parameter is formulated as a function of temperature in order to reproduce the effect of aggregation for increasing temperatures where the mean particle diameter

typically increases while the intercept parameter and the slope of the DSD decrease:

$$N_o^s = \min \left( 2 \times 10^8, 2 \times 10^6 \exp[-0.12 \min(0.001, T - T_o)] \right), \quad (2.12)$$

where  $T_o = 0^\circ \text{ C}$  and  $T$  is the ambient temperature.

In the original paper, the DSD of graupel is given by a generalized gamma distribution and the intercept parameter is defined as a function of graupel mixing ratio  $q_g$ :

$$N(D) = N_o^g D^{(\nu-1)} \exp(-\lambda_g D), \quad (2.13)$$

where

$$\lambda_g = 1.32 \left( \frac{\pi \rho_g N_o^g}{\rho q_g} \right) \quad (2.14)$$

and

$$N_o^g = 2.38 \left( \frac{\pi \rho_g}{\rho q_g} \right)^{0.92}. \quad (2.15)$$

Later studies showed that this PSD strongly overestimates larger particles (Figure 2.3). Therefore, in the LMK an exponential distribution is assumed (similar to the assumptions in the 3 component scheme) and only the intercept parameter  $N_o^g$  is considered in the original notation (A. Seifert, personal communication). The density of graupel is fixed at  $0.4 \text{ g cm}^{-3}$  and  $\nu = 2$ . Because of  $N_{o,g} \rightarrow \infty$  as  $q_g \rightarrow 0$  the magnitude of  $N_o^g$  is limited not to exceed a fixed maximum value of  $5 \times 10^7 \text{ m}^{-4}$  while also imposing a lower limit of  $1 \times 10^4 \text{ m}^{-4}$ .

## MesoNH

The MesoNH (Mesoscale Non-Hydrostatic Model, Lafore (1998)) is the non-hydrostatic mesoscale atmospheric model of the French research community. It has been jointly developed at the Laboratoire d'Aerologie (Toulouse) and MétéoFrance. The model is intended to be applicable to all scales ranging from large (synoptic) to small (large eddy) scales and it is coupled with an on-line atmospheric chemistry module. MesoNH is the test bed of the AROME model (Application of Research to Operations at Mesoscale, Bouttier (2005)), which will be the operational forecasting model at Météo-France in 2008.

The MesoNH microphysical parameterization scheme (Caniaux et al. (1994)) considers cloud ice and cloud water, rain, aggregates, graupel, as well as hail (Pinty et al. (2002)). It is mainly based on the work by Lin et al. (1983) and Rutledge and Hobbs (1984). The size distribution of the precipitating ice hydrometeors and rain are assumed to follow a modified Marshall-Palmer distribution:

$$N(D) = C \lambda^{X+1} \exp(-\lambda D), \quad (2.16)$$

where  $N_o$  as well as the slope parameter  $\lambda$  depend on the precipitation amount of the hydrometeor class. The intercept parameter  $N_o$  and  $\lambda$  are related to each other by  $N_o = C \lambda^X$  where the constants  $C$  and  $X$  depend on the hydrometeor type  $x$ . The slope parameter is

Parameters	Rain		Snow	Graupel	Hail
$\alpha$	1		1	1	1
$\nu$	1		1	1	1
a	524		0.02	19.6	470
b	3		1.9	2.8	3
c	842		5.1	124	207
d	0.8		0.27	0.66	0.64
C	$10^7$		5	$5 \times 10^5$	$5 \times 10^{-4}$
X	-1		1	-0.5	2

**Table 2.3:** Parameters of the DSD in the MesoNH microphysical parameterization scheme (Caniaux et al. (1994)).

given by

$$\lambda_x = \left( \frac{\rho q_x}{a C G(b)} \right)^{\frac{1}{x-b}}, \quad (2.17)$$

with  $G$  representing a generalized Gamma-law:

$$G(p) = \frac{\Gamma(\nu + p/a)}{\Gamma(\nu)}. \quad (2.18)$$

The density of hailstones is fixed at  $0.9 \text{ g cm}^{-3}$ . For the other ice hydrometeors the following power law relationship is assumed:

$$m(D) = a D^b. \quad (2.19)$$

The different constants used in this formulation of DSD are specified for each precipitating hydrometeor type and are summarized in Table 2.3.

## 2.3 Observation by Polarimetric Radar

The temporal and spatial evolution of precipitation events can be observed by radar and especially polarimetric radar systems. A polarimetric radar in contrast to conventional systems is capable of controlling the polarization state of the transmitted and received electromagnetic wave. Because most precipitating particles are not spherical in shape and, therefore, appear differently in the two polarization planes polarimetry gives additional information on the characteristics of the precipitation. Polarimetric signatures of precipitation are among others dependent on the size, shape, thermodynamic phase, and falling behavior of the individual particles present in the observed volume. Combining the information content of the different polarimetric variables allows for the discrimination of the predominant hydrometeor type within the scanned volume which gives insight into the microphysics of the system. Furthermore, knowing what precipitation type is reaching the ground is a fundamental prerequisite for an accurate determination of the precipitation amount. Using the additional information of polarimetry, improved quantitative rain estimates in comparison

to conventional radar systems can be obtained. Data quality is enhanced because the measurements discriminate among ground targets, biological scatterers (insects and birds), and precipitation. Polarimetry can be used for the recognition of anomalous propagation as well as for the correction for attenuation. Consistency among the different polarimetric variables helps to verify radar hardware calibration.

Within this work, observations by the DLR polarimetric diversity Doppler radar POLDIRAD (Schroth et al. (1988)) will be employed as a reference for the evaluation of the synthetic polarimetric radar quantities. POLDIRAD operates at C band (5.5027 GHz, 5.45 cm) and in contrast to most polarimetric radar systems developed for routine measurements, it is fully polarized. This means that besides the standard linear polarization, it can also be driven at circular or elliptical polarizations. Furthermore, POLDIRAD measures, both, the polar as well as the crosspolar signals allowing for the observation of the linear depolarization ratio ( $L_{DR}$ ) which normally is not routinely included and has to be substituted by  $\rho_{HV}$  (Section 2.3.2). The capabilities of POLDIRAD were demonstrated in a number of projects investigating the formation and life cycle of severe weather events including fronts and deep convective systems (e.g. Meischner et al. (1991), Höller et al. (1994), Dotzek et al. (2001)). The technical specifications of POLDIRAD are summarized in Appendix A.

### 2.3.1 Radar Detection of Precipitation

A meteorological radar measures precipitation by transmitting and receiving pulsed electromagnetic waves. With each pulse, a radar resolution volume is illuminated and energy is backscattered to the radar by the precipitation particles within this volume. The mean received power  $\overline{P}_r$  at the antenna is a function of radar constants, the distance  $r$  to the scanned volume, and the sum of powers backscattered by the precipitating particles within the resolution volume. It can be described by the radar equation (Battan (1973)):

$$\overline{P}_r = \frac{P_t G^2 \lambda^2}{(4\pi)^3 r^4} \sum_i^n \sigma_i, \quad (2.20)$$

where  $P_t$  is the transmitted power,  $G$  is the antenna gain,  $\lambda$  is the wavelength of the transmitted electromagnetic wave, and  $\sigma_i$  is the backscatter cross-section of the single scatterer  $i$ . In order to retrieve the information content of the received signal, the returned power must be related to the physical characteristics of the precipitation particles. In the case that the Rayleigh approximation is valid ( $D \leq \lambda/16$ ), the backscattering cross-section  $\sigma$  of a single water drop increases with the sixth power of the diameter  $D$  (Doviak and Zrnicek (1984)):

$$\sigma = \frac{\pi^5}{\lambda^4} |K|^2 D^6, \quad (2.21)$$

with  $|K|^2$  being the complex index of refraction (see Section 3.3). For drops with diameters larger than  $\sim \lambda/16$ , the Rayleigh approximation is not anymore applicable and Mie or optical scattering occurs resulting in fluctuations of the backscattered power as the size of the scatterer increases because of resonance effects.

The radar volume  $V$  can be described as a function of range  $r$ , the horizontal ( $\Theta$ ) and vertical

( $\Phi$ ) widths of the radar beam in radians, as well as the transmitted pulse length  $h$ :

$$V = \pi \left( r \frac{\Theta}{2} \right) \left( r \frac{\Phi}{2} \right) \frac{h}{2}. \quad (2.22)$$

$h$  is defined as  $h = c\tau$  with  $c$  being the speed of light and  $\tau$  being the pulse duration. Within the volume of interest  $V$ , hydrometeors are assumed to be randomly positioned. This allows to formulate the total backscattering cross section in Equation 2.20 as the backscattering per unit volume multiplied by the volume  $V$  from which the radar measurements are obtained. Combining Equations 2.20 and 2.22 gives (Battan (1973)):

$$\overline{P_r} = \frac{P_t G^2 \lambda^2 \Theta \Phi h}{512 (2 \ln 2) \pi^2 r^2} \sum_{Vol} \sigma_i. \quad (2.23)$$

The term  $(2 \ln 2)$  is a factor that adjusts the halfpower beamwidths assuming a Gaussian distribution to an effective beamwidth which has a constant distribution of power. Including the information about the radar characteristics as well as the numerical constants in the so called 'radar constant'  $C$  and substituting Equation 2.21 into 2.23 gives:

$$\overline{P_r} = C \frac{|K|^2}{r^2} \sum_{Vol} D_i^6, \quad (2.24)$$

where the summation is done for the scatterers distributed in a unit volume. In order to relate the received power  $\overline{P_r}$  to the physical characteristics of the precipitation the radar reflectivity factor  $z$  is introduced. It is given by the summation of the backscattered cross-sections from back scatterers in a unit volume:

$$z = \sum_{Vol} D^6 = \sum_i n_i D_i^6 = \int N(D) D^6 dD, \quad (2.25)$$

where  $n_i$  is the number of drops per unit volume. In variables measured by the radar and the constants of the radar the reflectivity factor can be written as

$$z = \frac{\overline{P_r} r^2}{C |K|^2}. \quad (2.26)$$

$z$  is given in  $\text{mm}^6 \text{m}^{-3}$  but it is more convenient to use the logarithmic radar reflectivity factor  $Z$  which is defined as

$$Z = 10 \log_{10} \left( \frac{z}{1 \text{ mm}^6 \text{m}^{-3}} \right). \quad (2.27)$$

$Z$  is the logarithmic radar reflectivity factor measured in units of  $\sigma$  thus dBZ (i. e. decibels relative to a reflectivity of  $1 \text{ mm}^6 \text{m}^{-3}$ ) and it is common usage to refer to  $Z$  as 'radar reflectivity'.

The choice of the frequency respectively the wavelength  $\lambda$  of a radar system is normally driven by practical aspects. It is a tradeoff between accuracy and a number of constraints such as size, weight, and costs. The beam width for a circular antenna is proportional to

$\lambda/d$  where  $d$  is the diameter of the antenna. Therefore, longer wavelengths need a larger antenna to obtain a focused beam that are heavier, require more powerful motors to rotate them, and are more expensive than smaller antennae. The advantage of longer wavelengths as S band (2 – 4 GHz, 8 – 15 cm) or C band (4-8 GHz, 4 – 8 cm) lies in the reduced attenuation. Furthermore, the larger the wavelength more scattering occurs in the Rayleigh regime reducing resonance effects in the optical regime. However, the trend goes towards a denser network of X band systems (8-12 GHz, 2.5 – 4 cm) in combination with existing S or C band networks. The denser network of a great number of lowcost X band systems allows for a better sampling of especially the lowest atmospheric layers (e.g. the CASA project (Collaborative Adaptive Sensing of the Atmosphere, <http://www.casa.umass.edu/>) in the United States).

In the next section, the observation of microphysical properties of precipitation by polarimetric radar will be introduced and a summary of the most important observables and hydrometeor classification schemes will be given.

### 2.3.2 Polarimetric Radar Quantities

In the following dual, linear switchable polarization systems with reception of both, copolar and cross-polar components will be considered. During operation, the polarimetric radar alternately transmits a horizontally and vertically polarized electromagnetic wave on a pulse-to-pulse basis while receiving the two polarization states for each pulse. Thus, in addition to reflectivity there are a number of additional parameters available. These are the intrinsic variables providing information about backscatter from hydrometeors in the resolution volume and the propagation variables providing information about hydrometeors between the radar and the resolution volume. This work will focus on the intrinsic variables but the propagation variables will be discussed shortly in order to provide a complete picture of polarimetry.

#### Reflectivity

The radar reflectivity factor  $z$  at a horizontal and vertical polarization for a unit volume can be expressed according to Equations 2.21 and 2.25 as

$$z_{HH,VV}[\text{mm}^6\text{m}^{-3}] = \frac{\lambda^4}{\pi^5 |K|^2} \int \sigma_{H,V}(D)N(D)dD. \quad (2.28)$$

The subscripts refer to the horizontally (H) or vertically (V) transmitted (second index) and received (first index) waves and accordingly  $\sigma_{H,V}(D)$  gives the particle radar backscattering cross section at horizontal and vertical polarizations. The equivalent reflectivity factor is a measure of the intensity of a precipitation event. As shown in Equations 2.21 and 2.25, it is the sum of the contributions from all scatterers each with its own back scatter cross-section  $\sigma_i$ . However, it depends not only on the distribution of shapes and sizes but also on the type of hydrometeors present within the pulse volume. For a particle of a given size, ice produces lower reflectivity because of lower dielectric effects. The dielectric constant is about 20 % that of liquid for high-density ice and can be less than 5 % that of liquid for low density

ice (e. g. Straka et al. (2000), see Section 3.3). Furthermore, reflectivity is sensitive to radar calibration, as well as affected by attenuation in heavy precipitation (e. g. Zrníc et al. (2000), Bringi and Chandrasekar (2001)).

### Differential Reflectivity

The differential reflectivity ( $Z_{DR}$ ) has been introduced by Seliga and Bringi (1976) as a measure of the mean axis ratio and the preferred orientation of non spherical hydrometeors. It is obtained from the ratio of reflected power at horizontal and vertical polarizations:

$$Z_{DR} [\text{dB}] = 10 \log \frac{z_{HH}}{z_{VV}}. \quad (2.29)$$

Following Jameson (1983),  $Z_{DR}$  is interpreted in terms of the reflectivity weighted mean axis ratio of the precipitation particle. Positive ( $z_{HH} > z_{VV}$ ) or negative ( $z_{HH} < z_{VV}$ ) values of  $Z_{DR}$  result from a preferred horizontal or vertical alignment of the larger axis of the particles. Positive values of  $Z_{DR}$  are caused by the oblate shape of large rain drops whose major axes are highly oriented horizontally. Because the number of large drops gives information about the rain DSD, combining the information of reflectivity and  $Z_{DR}$  provides an improved rainfall rate (Seliga and Bringi (1976)). Negative values of  $Z_{DR}$  can arise from large oblate hail stones with their major axis aligned around the vertical. Canting affects  $Z_{DR}$  because the particle appears with a different effective length in the polarization plane. In case of melting ice, the dielectric constant and also  $Z_{DR}$  increase producing the typical enhanced signatures of melting snow in the brightband. Differential reflectivity is independent of calibration and total concentration but can depend on the distribution of concentration among various sizes as numerous larger-size hydrometeors produce large reflectivities influencing  $Z_{DR}$  (Straka et al. (2000)). Furthermore,  $Z_{DR}$  is not immune to propagation effects (Bringi and Chandrasekar (2001)).

### Linear Depolarization Ratio

When non spherical particles are illuminated by the radar beam, a portion of the incident horizontally polarized wave is depolarized and scattered into the vertical direction. This depolarization can be measured by transmitting horizontally polarized radar signals and measuring both, horizontally and vertically polarized echoes. The linear depolarization ratio ( $L_{DR}$ ) is then defined as the logarithm of the ratio of the cross-polar power ( $z_{VH}$ ) to the copolar power ( $z_{HH}$ ) received:

$$L_{DR} [\text{dB}] = 10 \log \frac{z_{VH}}{z_{HH}}. \quad (2.30)$$

In general both,  $Z_{DR}$  and  $L_{DR}$  depend on the asymmetry of the shapes of the scatterers and on the orientation of the symmetry axes relative to the direction of the incident beam. While  $Z_{DR}$  is maximum for nonspherical particles aligned in the polarization planes,  $z_{VH}$  and, therefore,  $L_{DR}$  increase to maximum values for nonspherical particles oriented at canting angles near  $45^\circ$ . The factors determining the amount of depolarization are, thus, the mean

shape of the particles and their mean canting angle but also the precipitation phase. Wet ice particles (melting or growing in wet mode) can lead to an increase of  $L_{DR}$  due to the enhanced refractive index as compared to pure ice. Therefore,  $L_{DR}$  is especially useful for the detection of graupel and hail above the melting level as these particles often consist of a small portion of water increasing the dielectric constant. Moreover, densely rimed ice hydrometeors exhibit a typical tumbling falling behavior, thus, increasing  $L_{DR}$ . The highest values of  $L_{DR}$  of about  $-15$  dB are associated with melting snowflakes (Illingworth (2004)) and found within the region of the brightband.  $L_{DR}$  is independent of the number concentration of particles and radar calibration but it is not immune to propagation effects (Bringi and Chandrasekar (2001)). Furthermore,  $L_{DR}$  tends to be more susceptible to noise than other polarimetric radar variables because the cross-polar signal is typically two to three orders of magnitude smaller than the copolar signal. Straka et al. (2000) estimated the lowest observable values of  $L_{DR}$  for the American polarimetric radar S-Pol (Bringi et al. (1993)) to be in the order of  $-30$  dB while for the DLR polarimetric diversity Doppler radar POLDIRAD this value is about  $-35$  dB (Schroth et al. (1988)).

### More polarimetric variables

Electromagnetic waves propagating through a medium experience changes in amplitude, polarization, and phase because of interactions with the constituents of the medium. These propagation effects affect the intrinsic quantities through attenuation (see Section 3.5) but they can also be quantified and related to the characteristics of the precipitation between the scanned volume and the radar.

In rain, the horizontally polarized waves experience larger phase shifts and propagate slower than the vertically polarized waves because rain drops are oblate and have a preferential orientation. These phase shifts can be easily measured and are quantified by the differential phase shift  $\Phi_{dp}$ . The specific differential phase  $K_{dp}$  is the range derivative of the differential phase and is a good indicator of liquid water and rain rate along the propagation path. In mixtures of statistically isotropic and anisotropic particles (like tumbling hail),  $K_{dp}$  is affected by the anisotropic hydrometeors only. Therefore,  $K_{dp}$  can be used to estimate the rain part in mixed phase precipitation (Zrníc and Ryzhkov (1996)). Another useful parameter is the cross correlation  $\rho_{HV}(0)$  between horizontally and vertically polarized echoes at zero time lag. It is a measure for the homogeneity of a mixture of hydrometeors (Balakrishnan and Zrníc (1990a)). Large values of  $\rho_{HV}(0)$  close to 1 can be expected for a highly oriented medium with only little variation in the canting angle distribution. On the other hand, a mixture of different types or shapes of particles causes a decrease of  $\rho_{HV}(0)$  values.

### Hydrometeor Classification

Because of their extensive information content, multiparameter radar measurements have emerged as leading discriminators of precipitation type and retrieving microphysical information from polarimetric radar observations has become an active topic of research. Seliga and Bringi (1976) introduced the differential reflectivity  $Z_{DR}$  as a measure of the oblateness of rain drops in order to improve rain estimation. Combining reflectivity and differential reflectivity, Aydin et al. (1986) derived a hail signal showing that the hail probability increases

with increasing reflectivity and zero  $Z_{DR}$ . Bringi et al. (1986) used T-Matrix calculations for the computation of  $L_{DR}$  for graupel particles which reproduced reasonably well the radar measurements in convective clouds. Balakrishnan and Zrnic (1990b) proposed the specific propagation phase  $K_{dp}$  to discriminate water from ice particles. The kinematics and precipitation formation in a German squall line was studied with a focus on microphysics by Meischner et al. (1991) using observations from POLDIRAD. Brandes et al. (1995) studied the microphysics in a Colorado thunderstorm using both, polarimetric radar observations as well as aircraft measurements.

These studies proved the potential of polarimetric radar variables for studying the microphysics of convective events. Höller et al. (1994) combined the observations of  $L_{DR}$  and  $Z_{DR}$  to derive information about the dominating precipitation type in the radar resolution volume. Straka et al. (2000) synthesized the a-priori knowledge about polarimetric radar measurements of the prevailing hydrometeor types and provided the relevant information to deduce bulk hydrometeor types and bulk amounts from polarimetric radar data. Furthermore, he stressed the potentials of fuzzy logic schemes for hydrometeor classification as polarimetric radar signatures for different hydrometeors are not mutually exclusive and unique.

This promoted a number of publications extending the decision tree method used by Höller et al. (1994) based on Boolean logic to fuzzy logic approaches (Vivekanandan et al. (1999), Keenan (2003)), and neuro-fuzzy logic methods (Liu and Chandrasekar (2000)). Zrnic et al. (2001) presented a fuzzy classification scheme for S band radars based on the work by Liu and Chandrasekar (2000) which has been implemented on the NCAR's S-Pol radar (Vivekanandan et al. (1999)) using  $Z_{HH}$ ,  $Z_{DR}$ ,  $K_{dp}$ ,  $\rho_{HV}(0)$ ,  $L_{DR}$ , and corresponding altitude for the discrimination of hydrometeor types.

While in the USA most radars are operated at S band in Europe C band is most commonly used. This causes problems in transferring the American classification schemes to Europe due to the increased magnitude of attenuation and Mie scattering effects at these wavelengths (Baldini et al. (2004)). Nevertheless, Keenan (2003) presented an empirically based fuzzy logic classification scheme for C band radars based on the phase space defined by Straka et al. (2000). Several propositions were made to adapt the hydrometeor classification scheme by Zrnic et al. (2001) with a reduced set of input parameters ( $Z_{HH}$ ,  $Z_{DR}$ , temperature) to C band radar (Cremonini et al. (2004), Baldini et al. (2004), Marzano et al. (2006)).

In the following the hydrometeor classification according to Höller et al. (1994) will be discussed and used later. This classification scheme employs a decision tree method with fixed thresholds for partitioning the  $L_{DR}$  and  $Z_{DR}$  space and has been derived in a semiempirical manner including T-Matrix simulations at 5 cm wavelength. The advantage of using the  $L_{DR}$  -  $Z_{DR}$  space consists in the independence of the two parameters on the maximum particles size (except for Mie scatterers) or particle concentrations. This is also the reason why reflectivity is not considered in this scheme as  $Z_{HH}$  strongly depends on the particle spectrum. The third parameter employed for the classification is the height of the melting layer to minimize some unreasonable ambiguities in the polarimetric radar parameters. The thresholds of the classification scheme are summarized in Table 2.4.

In case of small rain drops, the thresholds for  $Z_{DR}$  and  $L_{DR}$  are very low because these drops are nearly spherical in shape or only slightly deformed. This changes with increasing size of the rain drops where larger positive  $Z_{DR}$  values can be expected because of the

increasing oblateness of the drop with diameter. The drops are assumed to be canted by a few degrees which also increases the values of  $L_{DR}$ . Snow or small, dry graupel particles are characterized by  $Z_{DR}$  around 0 dB and very low  $L_{DR}$ . As small graupel or snow can produce the same  $Z_{DR}$  -  $L_{DR}$  characteristic as light rain, the height of the melting level is used to discriminate between the solid and liquid phase. For growing (in the wet mode) or melting graupel particles, the dielectric constant is increased and, therefore, the thresholds are shifted towards higher values of  $L_{DR}$  in comparison to dry graupel. Hail stones tend

Hydrometeor Type	Parameter Range		
Small Rain Drops	$Z_{DR} < +1$	$LDR < -35$	$H \leq H_{MELT}$
Large Rain Drops	$Z_{DR} \geq +1$	$LDR < -25$	
Graupel (dry, small), snow	$Z_{DR} \leq +1$	$LDR < -35$	$H > H_{MELT}$
Graupel (wet, melting, small) Graupel(dry, large) Hail(dry, small)	$-1 \leq Z_{DR} < +1$	$-35 < LDR \leq -25$	
Hail (dry)	$-1 \leq Z_{DR} \leq +1$	$-25 < LDR \leq -20$	
Hail (wet)	$-1 < Z_{DR} \leq +1$	$-20 < LDR \leq -15$	
Large wet hail	$Z_{DR} \leq +1$	$LDR > -15$	
Rain + small hail (wet)	$Z_{DR} \geq +1$	$-25 < LDR \leq -20$	
Rain + large hail (wet)	$Z_{DR} \geq +1$	$LDR > -20$	

**Table 2.4:** Thresholds partitioning the  $L_{DR}$ - $Z_{DR}$  space for the hydrometeor classification according to Höller et al. (1994).

to tumble while falling causing  $Z_{DR}$  to be relatively small and  $L_{DR}$  to be quite high.  $L_{DR}$  can be further increased in the case that wet hail stones are present. The largest values can be expected for particle distributions containing relatively high concentrations of large particles.

Straka et al. (2000) found these values to be in good agreement with the values derived for S band radars. However, evaluating polarimetric radar data and hydrometeor classification schemes is not an easy task because comprehensive in situ measurements of hydrometeor types and amounts are very difficult to obtain. Sometimes, there are in situ observations of rain, small hail, ice crystals, and graupel available from aircraft. But the comparison between these point measurements and the radar sampling volumes that are often several orders of magnitude larger than the typical particle probes contains a lot of uncertainty. Nevertheless, attempts were made to use aircraft measurements for validation purposes. Hagen et al. (1994) used aircraft equipped with PMS-2D cloud and precipitation probes for the verification of the hydrometeor classification after Höller et al. (1994). While they were unable to observe large graupel or hail for safety reasons, they found consistency of the observed polarimetric parameter clusters with the classification for the lighter ice phase hydrometeors. Liu and Chandrasekar (2000) tested the performance of their classification algorithm successfully for three summer and one winter storm against a hail chase van and aircraft high-volume particle spectrometers. However, in most cases the evaluation of classification schemes relies on spatial continuity, height above ground, and comparisons with conceptual models. Only recently May and Keenan (2005) proposed a very promising method comparing vertically looking radars and polarimetric radars. In these measurements the resolution volume

sizes are compatible and Doppler spectra from the vertically looking radars can reveal the distribution of drops, hail, and perhaps some ice crystals.

## Chapter 3

# Synthetic Polarimetric Radar

The last chapter showed that polarimetric radars yield multi-dimensional information closely related to the microphysical properties of a precipitation event. As polarimetric radar is the only remote sensing instrument capable of providing this information over longer time and larger space intervals, it is especially suited for the evaluation of the representation of microphysical processes in mesoscale NWP models. However, these observables can not be easily compared because they are not directly connected to the model variables. Therefore, either the observations have to be converted to model variables ('observation-to-model-approach') or synthetic observations have to be computed from the model parameters ('model-to-observation approach'). In the model-to-observation method, a so called 'forward operator' is employed to transform the model output into the variables of the remote sensing instrument and perform comparisons in terms of observables. For model evaluation purposes this approach tends to be favored because in the observation-to-model approach retrieval errors are usually difficult to characterize and, therefore, both elements of the comparison may be erroneous or at least seriously biased (Chevallier and Bauer (2003)).

Recently, conventional radar forward operators were presented to calculate radar reflectivities from model forecasts for evaluation purposes. Haase and Crewell (2000) developed the 'RadarSimulationsModell' (RSM) based on model output by the LM which currently is employed for operational validation at DWD and the Finnish Weather Service while Météo-France uses a similar tool presented by Caumont et al. (2006). Modeling of polarimetric radar quantities has been used in several studies for a better understanding of polarimetric radar measurements. Chandrasekar and Bringi (1987) studied the influence of varying rain drop-size distributions on the relation between radar reflectivity and the surface rain rate ( $Z - R$  relationship). Bringi et al. (1986) simulated polarimetric observations at S- and X band from a Colorado convective storm for melting graupel particles using the T-Matrix approach (Waterman (1969), Barber and Yeh (1975), see Appendix B). This work was extended by Vivekanandan et al. (1990) to modeling and observations of melting ice in general. Detailed scattering simulations of melting ice by Dölling (1997) showed the sensitivity of the simulated polarimetric radar parameters on the mixing ratio and the falling behaviour of the hydrometeors. Vivekanandan et al. (1993) studied the impact of mixtures of precipitation particles, while Zrníc et al. (2000) used the T-Matrix approach to study the sensitivities of polarimetric variables at C band in rain. Anagnostou and Krajewski (1997) and Capsoni

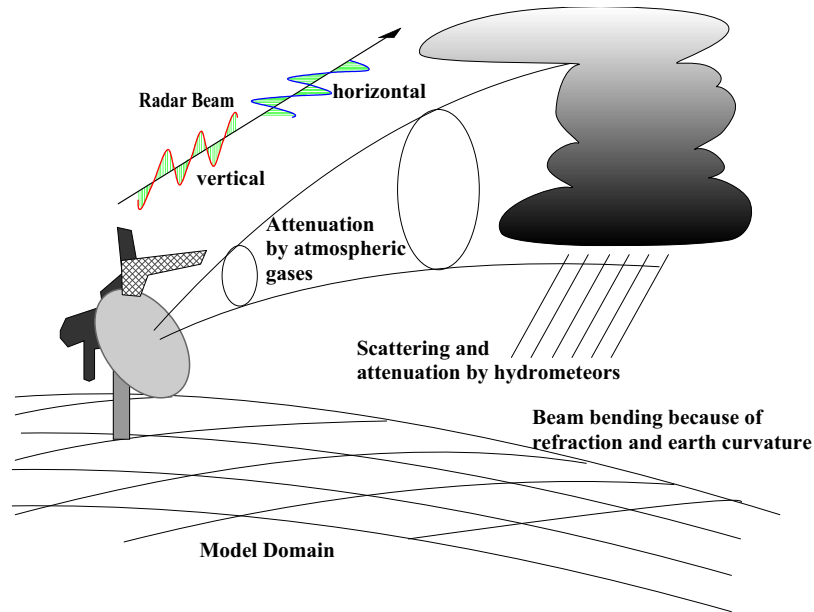


**Figure 3.1:** Conceptual view of the physical processes represented by the polarimetric radar forward operator SynPolRad (Synthetic Polarimetric Radar).

et al. (2001) presented polarimetric radar forward operators however only concentrating on rain with a statistically generated DSD.

### 3.1 Concept of a Polarimetric Radar Forward Operator

Combining the conventional radar forward operator RSM with the experience of polarimetric radar modeling, the polarimetric radar forward operator SynPolRad (Synthetic Polarimetric Radar, Pfeifer et al. (2004)) has been developed. SynPolRad simulates reflectivity and polarimetric radar quantities from model forecasts and, therefore, constitutes a further development of conventional radar forward operators. In contrast to the polarimetric radar forward operators proposed by Anagnostou and Krajewski (1997) and Capsoni et al. (2001), it explicitly focuses on the ice phase and the precipitation fields are taken from routine model forecasts. Therefore, SynPolRad provides a novel tool for the evaluation of microphysical parameterization schemes in NWP mesoscale models employing polarimetric radar data. SynPolRad transforms the bulk water quantities of the different hydrometeor species prognosed by the NWP model into polarimetric radar variables as if operating a synthetic polarimetric radar in the model domain (Figure 3.1). This is achieved simulating the main processes relevant to polarimetric radar observations. The energy received at a radar basically depends on two physical processes. First, the interaction of the transmitted electromagnetic wave with the hydrometeors determining the amount of energy that is scattered back to the antenna by the scattering particle. Second, the propagation and attenuation processes between the scatterer and the radar antenna depending on the electromagnetic

characteristics of the medium that has to be crossed. Within SynPolRad, the different processes relevant to radar observations are simulated in separate tools. The beam propagation is computed following the conventional radar forward operator RSM while the scattering processes are calculated employing the T-Matrix code in the version by Bringi et al. (1986).

The 'RadarSimulationsModell' (RSM, Haase and Crewell (2000)) has been originally developed to simulate reflectivities from LM model forecasts. Within the RSM, the volume backscattering and the extinction by the hydrometeors are computed accordingly to Mie. Then, the propagation of the radar beam in the model domain is simulated considering beam bending and attenuation processes. For the attenuation, the RSM computes both the extinction by hydrometeors as well as gaseous attenuation. The latter one is due to the presence of molecular oxygen, water vapor, and nitrogen, and can be calculated employing the millimeter-wave propagation model by Liebe et al. (1993). The consideration of attenuation processes constitutes the main difference to the French radar forward operator developed by Caumont et al. (2006) where these processes are not included. Within the RSM, the beam propagation is calculated considering, both, beam bending due to the earth curvature as well as refraction in the earth atmosphere. The RSM offers two possibilities to consider refractive effects: First, the explicit calculation of the refractive index and, second, the 4/3 earth radius approximation (see Section 3.4). Meetschen et al. (2000) introduced the antenna pattern into the RSM to include effects due to beam broadening into the synthetic radar scans. Up to now, the antenna pattern has not been integrated into SynPolRad because of the massively increasing computational costs.

The improvement of SynPolRad in comparison to the RSM consists in the higher sophisticated computation of the interaction of the radar beam with the hydrometeors employing the T-Matrix approach. The T-Matrix method is a powerful technique for computing light scattering by nonspherical particles based on solving Maxwell's equations. It is applicable to nonspherical particles and, therefore, allows for the simulation of polarimetric signatures. The method was initially developed by Waterman (1969) and further developed for multiple applications related to the simulation of light scattering (For an overview see Mishchenko and Travis (1998)). The T-Matrix method is applicable to randomly oriented particles but particles are normally assumed to be rotationally symmetric in order to save computational time. A fundamental feature of the T-Matrix approach is that it is independent on the incident and scattered fields and only depends on the shape, size and refractive index of the scattering particles as well as its orientation. A detailed discussion of the T-Matrix approach can be found in Appendix B.

SynPolRad employs the T-Matrix code in the version by Bringi et al. (1986) which also considers Rayleigh or Mie scattering if the assumptions are valid to reduce computational costs. The original scattering model is an extensive code written in Fortran77. For the use within SynPolRad it was translated and optimized to Fortran90. Furthermore, for the calculation of the dielectric constant of ice, SynPolRad employs the model developed by Warren (1984) instead of Ray (1972) (see Section 3.3).

Figure 3.2 gives a schematic overview of the single operations SynPolRad exerts onto the model and radar data. In a first step, the electromagnetic interactions (scattering and attenuation) of the radar beam with the hydrometeors are computed at every model grid point using the T-Matrix approach. In a second step, the propagation of the radar beam in the

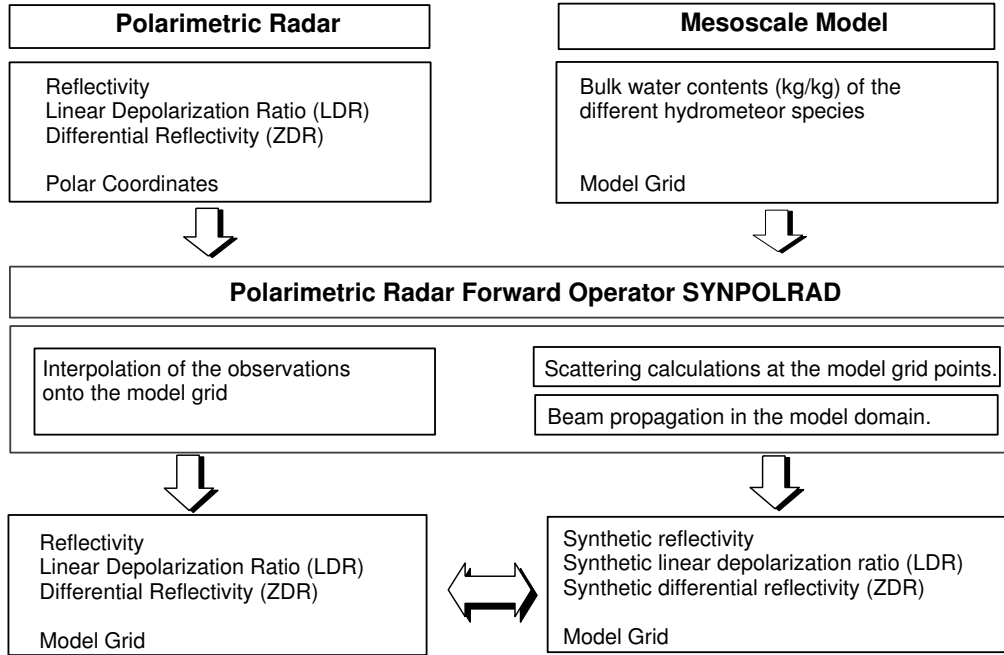


**Figure 3.2:** Flow chart of the processing of model and radar data by SynPolRad.

model domain is calculated including beam attenuation and refraction following the RSM. Finally, the observations are interpolated onto the model grid allowing comparisons of the simulated and observed polarimetric radar quantities in terms of the same physical units and the same spatial resolution. In the following, the single processes considered by SynPolRad will be discussed separately.

## 3.2 Calculation of the Polarimetric Quantities

The intrinsic polarimetric variables  $Z_{HH}$ ,  $L_{DR}$ , and  $Z_{DR}$  were defined in Section 2.3.2 as different combinations of the backscattered energy in the two orthogonally polarized channels of the polarimetric radar. In case of linear polarization, the transmitted wave  $\mathbf{E}^i$  as well as the scattered wave  $\mathbf{E}^s$  can be expressed as a linear combination of two vectors in an orthonormal polarization basis:

$$\mathbf{E}^i = E_V^i \mathbf{e}_V + E_H^i \mathbf{e}_H, \quad (3.1)$$

$$\mathbf{E}^s = E_V^s \mathbf{e}_V + E_H^s \mathbf{e}_H, \quad (3.2)$$

where  $\mathbf{e}_V$  is the unit vector in the vertical and  $\mathbf{e}_H$  in the horizontal. The scattering particle is assumed to be located at the origin of a Cartesian coordinate system and the incident wave propagates in the  $\mathbf{X}$ - $\mathbf{Z}$  plane (see Figure 3.3). The conventional radar elevation angle  $\Psi$  is then given by the angle between the incidence direction and the  $\mathbf{X}$  axis. Unless the target is very close to the radar, elevation angles are small ( $< 10^\circ$ ) and the model calculations are not very sensitive to  $\Psi$  (Vivekanandan (1986)). Thus, it is assumed that  $\Psi = 0$  and that, therefore, the radar (located at  $\mathbf{X}$ ) transmits an incident wave propagating along the  $-\mathbf{X}$

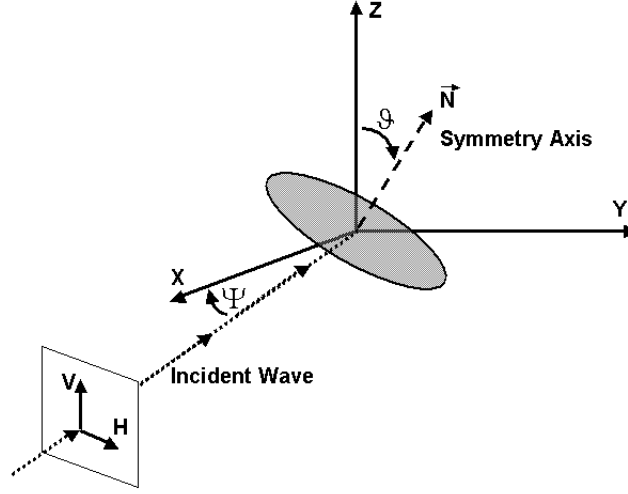


**Figure 3.3:** Scattering geometry where  $\vec{N}$  is the symmetry axis of the scatterer.  $\Psi$  is the conventional radar elevation angle,  $\mathbf{V}$  and  $\mathbf{H}$  are the linear polarization base vectors, and  $\vartheta$  is the canting angle of the scatterer. The incident wave is assumed to propagate along the  $-\mathbf{X}$  direction (see also Vivekanandan (1986)).

axis. The polarization base vectors  $\mathbf{V}$  and  $\mathbf{H}$  are then equal to  $\mathbf{Z}$  and  $\mathbf{Y}$ , respectively. The backscattered field  $\mathbf{E}^s$  can be related to the incident field  $\mathbf{E}^i$  using the symmetric backscatter matrix  $\mathbf{S}$

$$\begin{bmatrix} E_V^s \\ E_H^s \end{bmatrix} = \mathbf{S} \begin{bmatrix} E_V^i \\ E_H^i \end{bmatrix} = \begin{bmatrix} S_{VV} & S_{VH} \\ S_{HV} & S_{HH} \end{bmatrix} \begin{bmatrix} E_V^i \\ E_H^i \end{bmatrix}, \quad (3.3)$$

where the first index of the matrix elements  $S_{ij}$  describes the received and the second index the transmitted polarization state of the waves. The scattering matrix  $\mathbf{S}$  characterizes the microphysical properties of the scatterer relevant for the scattering process and depends on particle's size relative to wavelength, particle shape, orientation, and dielectric constant. Assuming that the scattering particle is rotationally symmetric,  $\mathbf{S}$  can be simplified to:

$$\begin{bmatrix} E_V^s \\ E_H^s \end{bmatrix} = \begin{bmatrix} S_{VV} & 0 \\ 0 & S_{HH} \end{bmatrix} \begin{bmatrix} E_V^i \\ E_H^i \end{bmatrix}. \quad (3.4)$$

Hydrometeors falling in the atmosphere tend to tumble depending on their shape and their spatial distribution of water interacting with the air flow and, thus, the particles principle axes are not necessarily aligned horizontally or vertically. In order to account for this canting of the particle,  $S_{VV}$  and  $S_{HH}$  are changed to  $S_{11}$  and  $S_{22}$  denoting the principal plane backscatter matrix elements for an axisymmetric scatterer independent from the polarization basis  $\mathbf{H}$  and  $\mathbf{V}$ . The canting angle  $\vartheta$  of the particle is then defined by the angle between the symmetry axis  $\vec{N}$  and the  $\mathbf{Z}$  axis. If the hydrometeor is canting to the principal polarization plane with an angle  $\vartheta$ , the polarization axes have to be rotated (Vivekanandan (1986)):

$$\begin{bmatrix} e'_V \\ e'_H \end{bmatrix} = \begin{bmatrix} \cos \vartheta & \sin \vartheta \\ -\sin \vartheta & \cos \vartheta \end{bmatrix} \begin{bmatrix} e_V \\ e_H \end{bmatrix} = \mathbf{R}(\vartheta) \begin{bmatrix} e_V \\ e_H \end{bmatrix}, \quad (3.5)$$

and the scattered field can then be described as

$$\begin{bmatrix} E_V^s \\ E_H^s \end{bmatrix} = \mathbf{R}^{-1}(\vartheta) \begin{bmatrix} S_{11} & 0 \\ 0 & S_{22} \end{bmatrix} \mathbf{R}(\vartheta) \begin{bmatrix} E_V^i \\ E_H^i \end{bmatrix}. \quad (3.6)$$

In order to obtain the energy  $\mathbf{E}^s$  that is backscattered by a given particle, the elements of the backscattering matrix  $\mathbf{S}$  have to be computed. This is done within SynPolRad employing the T-Matrix approximation or if the assumptions are valid, Rayleigh or Mie scattering theory in order to save computational time. Within the T-Matrix approach, the scattered electromagnetic fields are related to the incident fields and the physical characteristics of the scatterer using the extended boundary condition. A detailed introduction to the T-Matrix approach is given in Appendix B.

Adapting these findings to an ensemble of hydrometeors with a given DSD filling the radar volume,  $z_{HH}$ ,  $z_{VV}$ , and  $z_{HV}$  can be written analogous to 2.28 as (Holt (1984)):

$$z_{HH} = \frac{\lambda^4}{\pi^5 |K|^2} \int_D N(D) dD \int_{\vartheta} |S_{11} \sin^2 \vartheta + S_{22} \cos^2 \vartheta|^2 p(\vartheta) d\vartheta, \quad (3.7)$$

$$z_{VV} = \frac{\lambda^4}{\pi^5 |K|^2} \int_D N(D) dD \int_{\vartheta} |S_{11} \cos^2 \vartheta + S_{22} \sin^2 \vartheta|^2 p(\vartheta) d\vartheta, \quad (3.8)$$

$$z_{HV} = \frac{\lambda^4}{\pi^5 |K|^2} \int_D N(D) dD \int_{\vartheta} |S_{11} - S_{22}|^2 \cos^2 \vartheta \sin^2 \vartheta p(\vartheta) d\vartheta. \quad (3.9)$$

$p(\vartheta)$  gives the distribution function of canting angles  $\vartheta$  for the ensemble of hydrometeors in the radar volume. Normally, a Gaussian distribution is assumed with a mean canting angle  $\bar{\vartheta}$  which is normally set to 0 (Vivekanandan (1986)). Within SynPolRad, this Gaussian distribution of canting angles is specified by its maximum canting angle and its standard deviation. The scattering processes are computed for the different hydrometeor types in discrete intervals of the DSD and the distribution of canting angles. From  $z_{HH}$ ,  $z_{VV}$ , and  $z_{HV}$ , the differential reflectivity  $Z_{DR}$  and the linear depolarization ratio  $L_{DR}$  can be calculated following Equations 2.29 and 2.30.

### 3.3 Calculation of the Complex Dielectric Constant

The complex dielectric constant  $K$  has already been mentioned several times related to the polarimetric radar quantities (i. e. Section 2.3.2) because of the great differences for liquid

and solid phase hydrometeors and its implications on the interpretation of radar measurements.  $K$  is a constant describing the electromagnetic properties for a given substance. It is derived from the refractive index  $m$  as:

$$|K|^2 = \left| \frac{m-1}{m+2} \right|^2. \quad (3.10)$$

The complex refractive index  $m$  of the substance

$$m = n - ik, \quad (3.11)$$

describes the propagation of the electromagnetic wave in the medium with the real part  $n$  while the imaginary part  $\text{Im}(-k)$  gives the absorption coefficient of the medium.  $n$  is called the ordinary refractive index. It is defined as the ratio of the speed of light in a vacuum  $c$  to the speed of light in the medium  $\nu$ :

$$n = \frac{c}{\nu}. \quad (3.12)$$

Apart from the dependence on the substance, the complex index of refraction depends also on temperature and wavelength. The refractive indices of water (Ray (1972)) and ice (War-

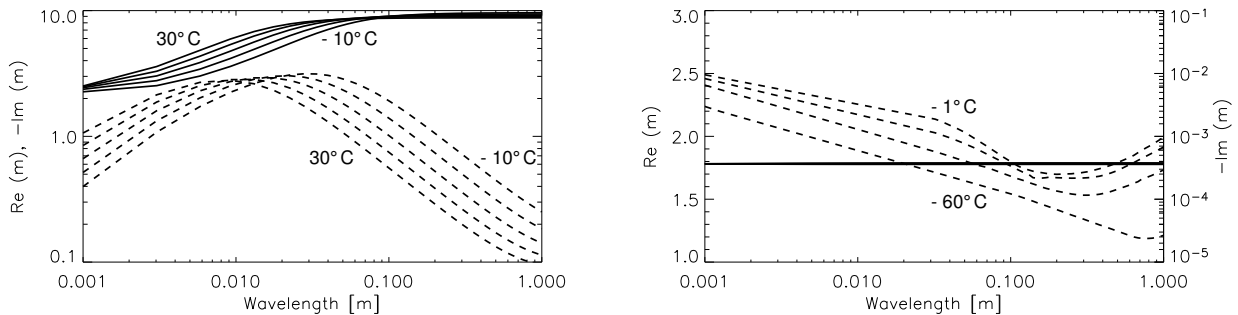


**Figure 3.4:** Refractive index  $m$  of water (left, Ray (1972)) and ice (right, Warren (1984)) as a function of wavelength (m) and temperature ( $^{\circ}$  C). The real part of the refractive index  $Re(m)$  is given by the solid and the imaginary part  $-Im(m)$  by the dashed lines. For water, the refractive index is shown for temperatures ranging from  $-10^{\circ}$  C to  $30^{\circ}$  C in intervals of  $10^{\circ}$  C. The refractive index of ice is shown for  $-1^{\circ}$ ,  $-5^{\circ}$ ,  $-20^{\circ}$ , and  $-60^{\circ}$  C.

ren (1984)) are shown in Figure 3.4 as a function of wavelength and temperature.

The dielectric constant of pure ice is almost five times smaller than the one for water and can be further reduced for very light ice particles such as snow (Straka et al. (2000)). The dielectric constant of ice depends on the ratio of pure ice to air or water content where air reduces and water enhances the dielectric constant. As ice hydrometeors normally do not consist of pure ice nor is the structure of the material homogeneous, the dielectric constant of hydrometeors is highly variable. These variations in dielectric constants result in significant differences in reflectivity for the same amount of precipitating water and cause prominent features such as the brightband where a sudden increase in reflectivity is observed mostly

due to the enhanced dielectric constant of melting snow. Furthermore, high dielectric constants cause larger depolarizations while polarimetric signature are reduced for low density ice hydrometeors through the dielectric constant (Matrosov et al. (1996)).

Because of this large variability and its impact on radar quantities, an accurate simulation of the dielectric constant is very important. Fabry and Szyrmer (1999) compared several models for the calculations of the dielectric constant of melting hydrometeors to be used for the simulation of reflectivities from an advanced cloud microphysical model. They found that the computed reflectivity changed significantly with the model for the dielectric constant and the snowflake density. The best results in comparisons with observations were obtained for a model that treated the melting snowflake with an inner core of a high density water/air/ice mixture and an outer low density shell with a sharp density break in between. Nevertheless, in this work a simpler model is employed assuming, like it is done in NWP models, homogeneous particles. Within SynPolRad, the ice particles are treated as a mixture of pure ice and air consistent with the density assumed by the mesoscale model. The dielectric constant is then calculated by describing the particle's structure as randomly oriented elliptical inclusions of ice inside an air matrix as proposed by Bohren and Battan (1982) using the Maxwell Garnet formula (Maxwell Garnet (1904)). Then the average dielectric constant of such a mixture of different substances can be formulated as

$$K = \frac{(1 - f)K_M + f\beta K_I}{1 - f + f\beta}, \quad (3.13)$$

where  $K_I$  is the complex dielectric constant of the intrusions,  $K_M$  the one of the surrounding matrix,  $f$  gives the volume of the intrusions, and  $\beta$  is a form factor describing the shape of the intrusions. For the calculations of the complex dielectric constant for water the model of Ray (1972) is used while the values for pure ice are derived from Warren (1984). In the case of melting or soaked particles, the Maxwell-Garnet formula is used twice. The dielectric constant of a mixed phase hydrometeor is then calculated as a water inside an ice matrix inside an air matrix, thus, first calculating the dielectric constant of a water and ice mixture and then in a second step the water/ice/air mixture.

### 3.4 Beam Propagation

For the simulation of the different radar scans, a model for the beam propagation in the atmosphere has to be integrated in SynPolRad. Two effects have to be considered governing the propagation of the radar beam and especially its height in the atmosphere: First, the curvature of the earth and, second, the refraction in the atmosphere. Using geometrical optics, the height  $H$  of the radar beam assuming a constant refractive index and linear propagation is (Figure 3.5)

$$R^2 + r^2 = (r + H)^2, \quad (3.14)$$

$$H = \sqrt{r^2 + R^2} - R, \quad (3.15)$$

where  $R$  is the earth radius and  $r$  the range. With the same assumptions, the curvature  $d\Phi/ds$  of the radar beam relative to the earth surface is given by

$$\frac{d\Phi}{ds} = \frac{1}{R}. \quad (3.16)$$

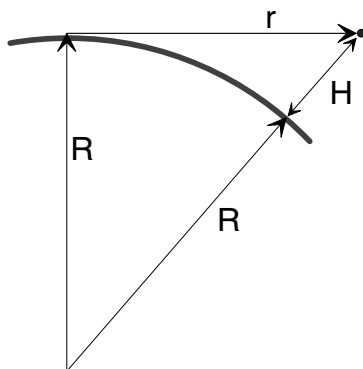


**Figure 3.5:** Geometry of the radar beam assuming linear propagation.  $\mathbf{H}$  is the height above ground,  $\mathbf{r}$  the range of the radar beam in the atmosphere, and  $\mathbf{R}$  is the earth radius.

However, the refractive index of air  $n$  is not a constant and the path of the radar beam depends principally on the change with height of the atmosphere's refractive index. Near sea level it is approximately 1.0003 to 1.0004. Since the important part of  $n$  is in the fourth, fifth, and sixth decimal places at microwave frequencies, it becomes convenient to introduce a new parameter  $N$  being the refractivity of the atmosphere:

$$N = (n - 1) \cdot 10^6. \quad (3.17)$$

$N$  is a function of temperature, pressure, and vapor pressure and can be computed as (Bean and Dutton (1968))

$$N = \frac{77.6}{T} \left( p + \frac{4810 e}{T} \right), \quad (3.18)$$

where  $T$  is the temperature in Kelvin,  $p$  is the atmospheric pressure in hPa, and  $e$  is the vapor pressure of the moist air in hPa. Both, pressure and temperature usually decrease with height above sea level and as in the troposphere the fractional decrease in pressure is larger than that of temperature,  $N$  normally decreases with altitude as well. According to the definition of the ordinary refractive index in Equation 3.12 and in case of 'normal conditions' with  $N$  decreasing with altitude, the velocity of the wave increases with height and the waves are bent downwards. The values of refractivity gradients attributed to normal conditions range between 0 and  $-78 \text{ km}^{-1}$  (Bech et al. (2000)).

Since the distribution of temperature and water vapor in the atmosphere is highly variable, different regimes for the propagation of the radar beam exist. In the case that the actual refractivity gradient of the atmosphere is larger than normal conditions, subrefraction occurs. The beam is bent upwards and targets near the ground can not be recognized anymore. Severe departures from normal refractivity exist in case of strong temperature inversions or large moisture gradients. If temperature increases with height, the slope  $dN/dz$  decreases which leads to superrefraction. The beam is bent more strongly towards the earth and more ground clutter is recognized which is also known as anomalous propagation (anaprop). In extreme cases if the rate of decrease in  $N$  exceeds a certain value (i. e.  $dN/dz \leq -157 \text{ km}^{-1}$

(Rinehart (2004)) electromagnetic waves are bent towards the surface of the earth and are reflected there. Then, the energy may travel trapped in layers for long distances.

Similar to Equation 3.16, beam bending in the atmosphere because of variations in the atmosphere's refractive index can be written as

$$\frac{d\Phi}{ds} = \frac{dn}{dz}, \quad (3.19)$$

which gives the total curvature of a ray relative to the earth surface as

$$\frac{d\Phi}{ds} = \frac{1}{R} + \frac{dn}{dz}. \quad (3.20)$$

For the interpretation of radar measurements, it is necessary to have some information about the position and especially the height of the scanned volume in the atmosphere. As in most applications no detailed information about the thermodynamical conditions and, thus, the atmosphere's refractive index is available, simpler models for the calculation of beam propagation have been developed. One of these is the 4/3 earth radius model which is employed in SynPolRad in order to save computational time by not calculating the refractivity explicitly. In radar meteorology, it is convenient to consider the ray path of the radar beam as a straight line. This can be reached assuming a fictitious earth with an effective radius equal to  $R'$  given by (Doviak and Zrnic (1984)):

$$\frac{1}{R'} = \frac{1}{R} + \frac{dn}{dz}, \quad (3.21)$$

from which

$$R' = \frac{R}{1 + R (dn/dz)}. \quad (3.22)$$

Further assuming that the standard vertical gradient of the refractive index  $dn/dz$  is nearly linear and equal to about  $-4 \times 10^{-8} \text{ m}^{-1}$ , the effective radius of the earth for propagation problems can be determined to be about 4/3 of the actual earth radius. Employing this effective radius, the radar beam can be treated as a straight line and beam height can be conveniently determined as a function of range. The 4/3 earth radius model is broadly used in radar meteorology although its main limitations need to be discussed. A detailed derivation of the 4/3 earth radius model can be found in Doviak and Zrnic (1984).

The first assumption deriving the 4/3 earth radius model was the linear dependence of refractivity on height which is not given in the atmosphere because of the variations in temperature and water vapor distributions. Nevertheless, severe departures from normal refractivity causing anomalous propagation only exist in regions with strong inversions and moisture gradients as they are typical for sea sites. Bech et al. (2000) analyzed the variability of refractivity using 653 radiosonde profiles covering the seasonal variability in the Barcelone region. They found that the gradient in refractivity within the first kilometer above sea level behaved predominantly as normal. Only in less than 10% of the days superrefractive conditions were found. As SynPolRad is to be used for the simulation of observations by the polarimetric radar POLDIRAD in the Alpine Foreland even less superrefraction can be expected especially as the focus of this work will be on convective events with a well mixed boundary layer.

In the derivation by Doviak and Zrnic (1984) a second assumption  $dH/dr \ll 1$  is employed which imposes a theoretical limit on the use of an effective earth's radius making it only valid for small elevation angles. In reality, it can be also successfully employed for larger elevation angles, as the path length through the critical atmospheric layers, especially inversions, diminishes with larger elevation and, therefore, deviations from the actual refractivity of the atmosphere become less important. Furthermore, Haase and Crewell (2000) showed that differences between the parameterized form of the 4/3 earth radius model and an actual calculation of the atmosphere's refractive index are only significant for elevation angles smaller than  $1^\circ$ . Therefore, these small elevation angles will not be used within SynPolRad.

### 3.5 Attenuation

Any electromagnetic wave passing through a medium experiences losses in power due to attenuation. This loss in power  $dP$  between the radar and the target depends on the material of the present medium, its density, and the path of the radar beam and can be described as (Battan (1973))

$$dP = 2 k P_o dr, \quad (3.23)$$

where  $P_o$  is the power which would have been received had there been no attenuation,  $r$  is the range, and  $k$  is the attenuation coefficient having dimensions  $\text{km}^{-1}$ . The attenuation coefficient  $k$  has already been defined in Equation 3.11 as the imaginary part of the dielectric constant of the substance. Total attenuation is given by integration over the whole path  $r$  times 2 because the attenuating media has to be crossed twice. Integration and conversion yields

$$10 \log \frac{P}{P_o} = -2 \int_0^r k dr. \quad (3.24)$$

In this form the reduction of  $P_o$  is expressed in decibels and  $k$  is given in decibels per length ( $\text{dB km}^{-1}$ ). Employing this formulation of  $k$ , losses by various causes can simply be added to give the total attenuation in decibels per kilometer.

Total attenuation is the combination of energy absorption by the medium and scattering of energy out of the radar beam. Since attenuation of microwaves can be caused by atmospheric gases, clouds, and precipitation, Equation 3.24 can be written as (Battan (1973))

$$10 \log \frac{P}{P_o} = -2 \int_0^r (k_g + k_c + k_p) dr, \quad (3.25)$$

where  $k_g$ ,  $k_c$ , and  $k_p$  represent the attenuation by gases, clouds, and precipitation, respectively. The only atmospheric gases that need to be considered as absorbers are water vapor and oxygen. This gaseous attenuation rate  $k_g$  is not negligible when targets are far away ( $r \geq 60$  km) and beam elevation is low. Within SynPolRad, gaseous attenuation is calculated using the model after Liebe et al. (1993). The attenuation of electromagnetic waves by hydrometeors in the atmosphere may result from both, absorption and scattering depending on the size, shape, and composition of the particles. At wavelengths from 5 to 10 cm attenuation by clouds can be safely neglected (Battan (1973)). For heavy rain or very dense ice

particles as for example hail, attenuation also plays an important role for C band systems. For the polarimetric quantities, differences in attenuation between the horizontal and vertical channel because of oriented hydrometeors such as rain drops or ice crystals have to be considered. While the specific attenuation  $k$  gives the attenuation of the horizontal channel, the specific differential attenuation  $A_{dp}$  ( $\text{dB km}^{-1}$ ) is defined as the difference in attenuation in the horizontal and vertical channel. The attenuated polarimetric quantities can then be calculated as (Bringi and Chandrasekar (2001))

$$Z_{HH} = Z_{HH}^o - 2 k r, \quad (3.26)$$

$$Z_{DR} = Z_{DR}^o - 2 A_{DP} r, \quad (3.27)$$

$$L_{DR} = L_{DR}^o + 2 A_{DP} r. \quad (3.28)$$

Within SynPolRad, the specific and the specific differential attenuation are calculated together with the polarimetric quantities by the scattering module solving the equations for the transmission matrix (Oguchi (1983), Vivekanandan (1986)). For the simulation of the beam propagation in the model domain, total attenuation and total specific attenuation are applied on the synthetic polarimetric quantities following Equations 3.26 to 3.28.

## 3.6 Interpolation of the Observations

Typically, a radar samples the atmosphere by so-called PPI scans (plan position indicator) varying the azimuth angle at a fixed elevation angle or RHI scans (range height indicator) varying the elevation angle at a fixed azimuth angle. If a complete volume is scanned, this is normally done by executing several PPI scans at different elevations. The spatial resolution of the radar is very fine in the surroundings of the instruments while the scanned volume increases with range because of beam broadening. According to the scanning technique and the irregular spatial resolution, the radar observations are executed and stored in polar coordinates. In order to simulate PPI and RHI scans, SynPolRad computes the polarimetric quantities as introduced in Section 3.2 at the grid points of the model. Then, the variables are interpolated to a polar coordinate system for the simulation of beam propagation (Section 3.4) including attenuation (Section 3.5) along its path. Finally, both, the observed and the synthetic polarimetric radar data, are transferred back to the model grid for evaluation.

This is done because successful and fair comparisons of observations and simulations are only possible in the same spatial resolution allowing the application of the same statistical methods on the two fields. There are several reasons for transferring the radar data back to the model grid. The resolution of the radar is finer than the model resolution and, therefore, by averaging from the finer to the coarser resolution, the sub-grid variability as well as extreme values of the radar measurements are smoothed. A further advantage of the model grid lies in its regular horizontal resolution which allows to do statistics on the number of pixels.

Choosing the right grid for RHI scans is more difficult because both, the observations and the model data, are given at an irregular vertical resolution. The resolution of the model is very fine in the first thousand meters in order to describe well the processes of the planetary boundary layer. This is also true for the radar with a fine resolution near the radar becoming

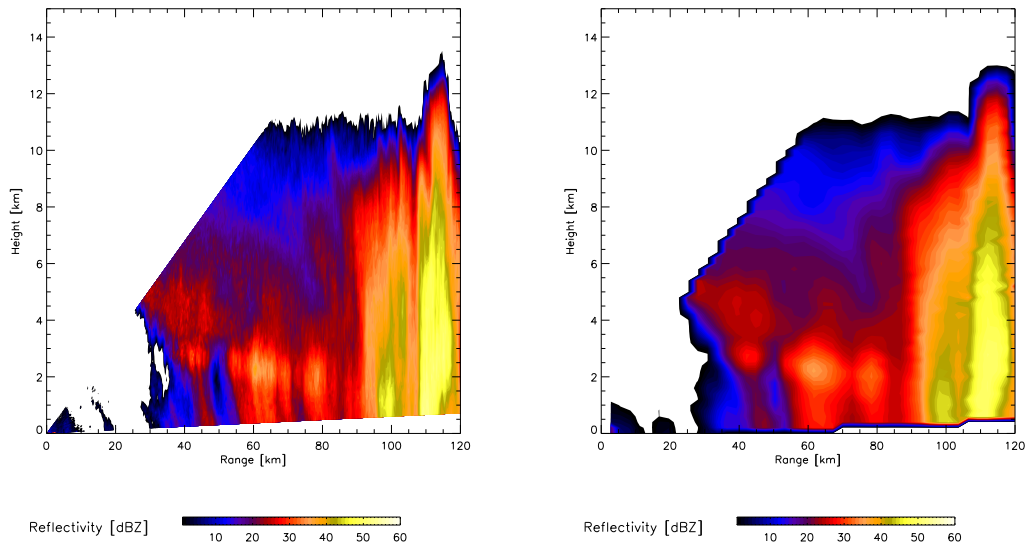


**Figure 3.6:** Comparison of POLDIRAD RHI scan in its original resolution (left) and interpolated on a vertical resolution of 200 m (right).

coarser due to beam broadening. Therefore, looking at RHI scans both, observations and simulations are interpolated at grid boxes with a constant height of 200 m. Figure 3.6 shows an example of a POLDIRAD RHI scan in its original resolution on the left and averaged on the 200 m vertical resolution on the right where the fine structures and extreme values are smoothed due to the averaging.

## Chapter 4

# Linking SynPolRad to the NWP Model

In the last chapter, the polarimetric radar forward operator SynPolRad has been introduced as a novel tool for the evaluation of microphysical processes in NWP models. However, a successful evaluation of the model physics is only achievable if the link between the model and the forward operator conforms as closely as possible to the model assumptions. Ideally, all the input variables of the forward operator are determined by the weather forecast model and if this is not the case these free parameters have to be defined such that no artifacts are included in the synthetic observables endangering a successful evaluation. Section 2.3.2 showed that polarimetric signatures depend on the spectrum of particle sizes relative to wavelength, particle shapes, particle dielectric constants, and particle falling behavior which affects the orientation of the particle relative to the direction of the incident wave and its polarization state. In order to successfully simulate polarimetric quantities out of model forecast, information on these quantities has to be provided by the NWP model to SynPolRad.

NWP models predict precipitation in bulk quantities of a given number of hydrometeor types where microphysical properties are derived using fixed assumptions regarding DSD and ice density. For the simulation of polarimetric quantities, SynPolRad requires information on the drop size distribution, the particle shape and falling behavior, as well as its dielectric constant given by the composition of the hydrometeor regarding the portions of ice, air, and water. Thus, there exists a number of free input parameters that are neither predicted nor defined by the mesoscale model but have significant importance for the simulations of polarimetric radar quantities. These are the parameters describing the shape and falling behavior of the particle as well as in the case of ice the degree of melting determining the dielectric constant. The link between the mesoscale model and SynPolRad is summarized as a conceptual overview in Figure 4.1.

In the case of rain, SynPolRad can easily be applied because the free parameters can be defined as a function of diameter. The problems simulating polarimetric radar signatures arise in the ice phase due to the natural variability in density, shape, and falling behavior for the different ice hydrometeor types. In order to overcome these problems and, nevertheless, simulate polarimetric radar parameters out of model forecasts, strategies of defining the free parameters will be discussed. This will be done on theoretical terms studying the impact of

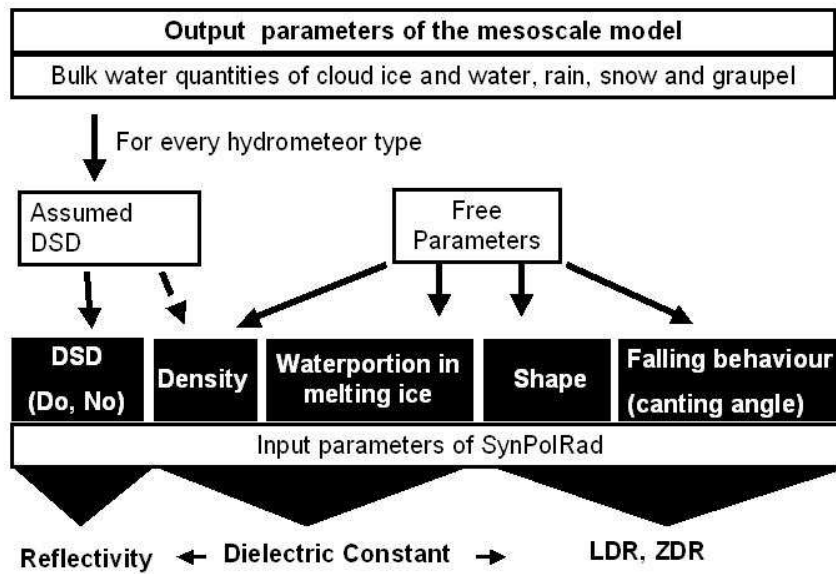


**Figure 4.1:** Conceptual view of the link between the NWP model and the polarimetric radar forward operator SynPolRad showing the input parameters defined by the model as well as the free parameters.

the single input parameters on the simulation of the polarimetric quantities using sensitivity studies. The results will be employed to determine the free parameters such that they represent physical considerations accordingly to the model assumptions. In the following, the input parameters of SynPolRad for rain and the determination of the free parameters for the ice hydrometeors will be discussed. Then, the focus will be set on the representation of brightband aspects and the chapter will finish with an evaluation of the polarimetric radar forward operator SynPolRad.

## 4.1 Input Parameters for Rain

In the case of rain, the simulation of the polarimetric quantities can easily be performed. The information on DSD is directly given by the mesoscale model. The dielectric constant for water is well defined (Ray (1972)). The shape dependence is given as a function of diameter by Andsager et al. (1999) (Equation 2.1) and the maximum canting angle  $\vartheta$  is set to  $10^\circ$  with a standard deviation of  $5^\circ$  according to Chandrasekar et al. (1988) and Straka et al. (2000).

Variable	Range	Intervals
$N_o$ [ $\text{mm}^{-1} \text{m}^{-3}$ ]	40 – 10 000	6
$D_o$ [mm]	1 – 10	7
Density [ $\text{g cm}^{-3}$ ]	0.01 – 0.9	10
Axis Ratio	0.3 – 1.8	16
Max. Canting Angle [ $^\circ$ ]	0 – 90	10

**Table 4.1:** Range of input parameters used within the sensitivity study for dry ice.

## 4.2 Sensitivities of Polarimetric Quantities to Microphysical Properties of Ice

Regarding the ice phase, the simulation of polarimetric quantities is more difficult than in the case of rain because of the number and the high natural variability of the free parameters that are not specified by the NWP model. To facilitate the discussion and the derivation of the free parameters, the sensitivities of the polarimetric quantities to the microphysical properties of ice will be studied on theoretical terms to investigate the importance of the single input parameters for the polarimetric variables. This will be done using sensitivity studies with the aim of finding relations or dependencies within the input parameters that can be used later to simplify the derivation of the free parameters.

The set of input parameters of the sensitivity study (Table 4.1) was chosen to represent the whole range of ice phase hydrometeors in the atmosphere. The values for the intercept parameter  $N_o$  ranged from  $40 \text{ mm}^{-1} \text{m}^{-3}$ , the value for hail by Cheng and English (1983), over  $400 \text{ mm}^{-1} \text{m}^{-3}$ , the lower bound for snow from Pruppacher and Klett (2003), to 800, 4000, and  $8000 \text{ mm}^{-1} \text{m}^{-3}$ , the intercept parameters of the LMK distributions for snow, graupel, and rain, to finally  $10000 \text{ mm}^{-1} \text{m}^{-3}$ , the upper bound for small hail and graupel by Straka et al. (2000). The median diameter  $D_o$  was varied from 1 – 10 mm. For ice hydrometeors,  $D$  describes the actual diameter regarding the maximum spatial extension of the particle and not the equivalent diameter giving the diameter of the equivalent water drop. Density ranged from 0.01 to  $0.9 \text{ g cm}^{-3}$  covering very light particles as aggregated snow flakes as well as heavily rimed ice as i. e. hail. The axis ratio was varied from 0.3 to 1.8 where 1 describes spherical shape, axis ratios smaller than 1 oblate particles, and larger than 1 prolate particles. Smaller axis ratios which would be true for ice plates or dendrites could not be considered because of the T-Matrix method becoming numerically unstable approaching these extreme values (see Appendix B). The maximum canting angle was varied from 0 to  $90^\circ$  and its standard deviation was fixed at half the maximum canting angle. Using data base operations, sets of all possible combinations of parameters were created and used as input for the T-Matrix calculations. The sensitivity study was calculated for a C band radar at a wavelength of 5.45 cm according to the technical specifications of the DLR polarimetric radar POLDIRAD (see Appendix A). In the following the general findings of the sensitivity study will be discussed.

First, the influence of the particle size distribution on reflectivity,  $L_{DR}$ , and  $Z_{DR}$  will be studied. Figure 4.2 shows the radar quantities as a function of  $N_o$  and  $D_o$  for particles with a fixed density of  $0.3 \text{ g cm}^{-3}$ , an axis ratio of 0.4, and a fixed maximum canting angle of  $40^\circ$ .

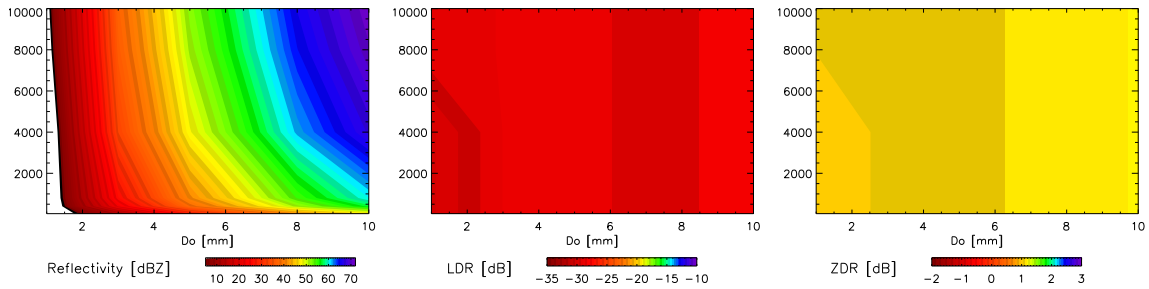


**Figure 4.2:** Reflectivity [dBZ],  $L_{DR}$  [dB], and  $Z_{DR}$  [dB] as a function of mean diameter  $D_o$  [mm] and intercept parameter  $N_o$  [ $\text{mm}^{-1} \text{m}^{-3}$ ] for dry ice particles with a fixed density of  $0.3 \text{ g cm}^{-3}$ , an axis ratio of 0.4, and a maximum canting angle of  $40^\circ$ .

Reflectivity increases strongly from 0 to 71 dBZ with both,  $D_o$  and  $N_o$ . The variations in  $N_o$  become more important for large  $D_o$  describing very broad PSD's. For small  $D_o$ , varying  $N_o$  doesn't have a large effect because the variation of  $N_o$  only affects the smaller size bins where the influence on reflectivity is less important because of  $Z \sim D^6$ .  $L_{DR}$  and  $Z_{DR}$  show only a very small dependence on  $D_o$  but no dependence on  $N_o$ . The variations with  $D_o$  range for  $L_{DR}$  from  $-29$  to  $-28$  dB and for  $Z_{DR}$  from 1.04 to 1.17 dB.

Figure 4.3 shows the dependence of reflectivity,  $L_{DR}$ , and  $Z_{DR}$  on axis ratio and maximum

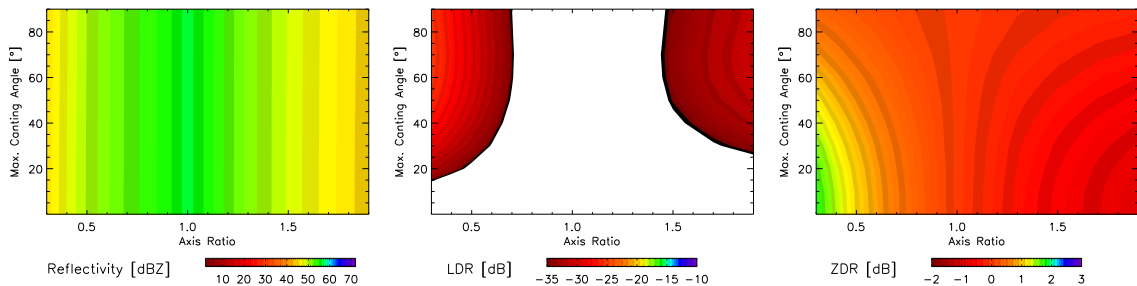


**Figure 4.3:** Reflectivity [dBZ],  $L_{DR}$  [dB], and  $Z_{DR}$  [dB] as a function of axis ratio and maximum canting angle for dry particles with  $N_o = 4000 \text{ mm}^{-1} \text{m}^{-3}$ ,  $D_o = 5 \text{ mm}$ , and density  $\rho = 0.3 \text{ g cm}^{-3}$ .

canting angle. The other parameters were held fixed at  $D_o = 5 \text{ mm}$ ,  $N_o = 4000 \text{ mm}^{-1} \text{m}^{-3}$ , and density  $\rho = 0.3 \text{ g cm}^{-3}$ . Reflectivity exhibits a relatively small dependence on axis ratio ranging from 44.7 to 56.6 dBZ. The remaining variability of reflectivity is due to the fact that for a given diameter particles with a smaller axis ratio do not fill the radar beam as well as spherical parameters with the same diameter and, therefore, deviations from spherical shape decrease reflectivity. If on the other hand, two particles with the same amount of water with different axis ratios would be compared, the flat particle would give larger reflectivities because its maximum dimension would be increased and, therefore, appear to be larger in the radar beam. However, the effect on reflectivity is quite small.  $L_{DR}$  and  $Z_{DR}$  show large variations with minimum values for both quantities for spherical particles ( $\alpha = 1$ ).  $L_{DR}$  increases with deviating axis ratio from 1 and increasing canting angle symmetrical for oblate and prolate particles up to  $-25$  dB.  $Z_{DR}$  is zero for spherical particles but increases

with decreasing axis ratio (oblate particles) to values up to 1.8 dB and decreases to  $-0.9$  dB for prolate particles ( $\alpha > 1$ ). Maximum values of  $Z_{DR}$  are reached in both cases for small maximum canting angles.

In the next section, the impact of varying dielectric constant due to variations in the ice

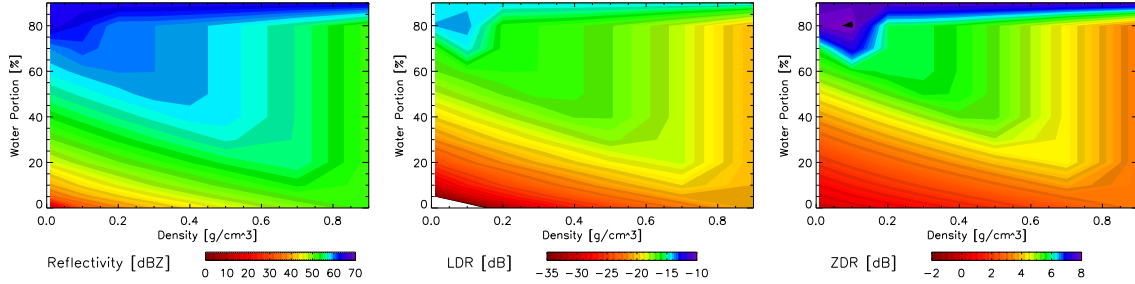


**Figure 4.4:** Reflectivity [dBZ],  $L_{DR}$  [dB], and  $Z_{DR}$  [dB] as a function of density [ $\text{g cm}^{-3}$ ] and water portion [%] in melting ice for  $N_o = 800 \text{ mm}^{-1} \text{ m}^{-3}$ ,  $D_o = 5 \text{ mm}$ ,  $\vartheta = 40^\circ$ , and  $\alpha = 0.3$ .

density and the water content of soaked ice particles will be studied. In order to do so, another sensitivity study has been performed where the water portion in melting ice was varied from 0 to 100% in intervals of 10%. The density of ice was varied with the same range of parameters as in the previous sensitivity study and the other parameters were fixed at  $N_o = 800 \text{ mm}^{-1} \text{ m}^{-3}$ , the value for snow in the LM,  $D_o = 5 \text{ mm}$ , a maximum canting angle  $\vartheta = 40^\circ$ , and an axis ratio  $\alpha = 0.3$ . Figure 4.4 shows reflectivity,  $L_{DR}$ , and  $Z_{DR}$  as a function of ice density and water content. All three parameters strongly increase with density and water portion where the increase with water portion is more important than the increase with density.  $Z_{HH}$  varies from 11.1 to 63.6 dBZ,  $L_{DR}$  from  $-58$  to  $-14$  dB, and  $Z_{DR}$  from 0.4 to 8.1 dB. All three quantities reach for a given density a point of saturation where increasing water amount doesn't have any effect. The higher the density of the ice hydrometeor is, the earlier this stage is reached. The explanation is that by calculating the dielectric constant of melting ice, the portions of air are exchanged to portions of water accordingly to the total water portion in the particle. At the moment where all air inclusions are filled with water, the dielectric constant does not change any more. This stage is obviously reached earlier for higher densities with less air inclusions. If this representation of melting ice is reasonable for high water portions is of no further importance for this work because such high water contents will not be used in SynPolRad and are only discussed here theoretically.

Summarizing the sensitivity studies, reflectivity only depends on the PSD and the dielectric constant being a function of ice density and the degree of melting of the particle. Further,  $Z_{HH}$  is almost unaffected by varying axis ratio and canting angle. Only extremely oblate and tumbling particles appear to be smaller in the radar beam giving a slight decrease in reflectivity for the same PSD in comparison to spherical particles. The sensitivity study showed further that once the density of the ice hydrometeor is fixed, the polarimetric variables  $L_{DR}$  and  $Z_{DR}$  only depend on the axis ratio and the canting angle but vary little with varying  $D_o$  or  $N_o$ . The polarimetric variables as well as reflectivity show a great dependence on dielectric constant.  $L_{DR}$  and  $Z_{DR}$  increase with the ice density, the water amount in melting ice, and

deviations from spherical shape.  $Z_{DR}$  is greatest for non spherical hydrometeors aligned in the horizontal whereas  $L_{DR}$  is greatest for non spherical hydrometeors aligned at an angle of  $45^\circ$ . The results of the sensitivity study are independent of the meteorological conditions apart from the calculations of the dielectric constant of ice which features a slight temperature dependence. This temperature dependence is more important for the imaginary part of the complex dielectric constant describing the absorption by the hydrometeor but less for the scattering processes. Therefore, the results of the sensitivity study, concentrated on the backscatter cross-section of hydrometeors, are not influenced by the fixed temperature. For the simulations of model output, the actual predicted temperature fields will be used.

### 4.3 Determination of the Free Parameters for Ice

The sensitivity study in the last section showed that reflectivity only depends on the particle spectrum and dielectric constant while the polarimetric variables  $L_{DR}$  and  $Z_{DR}$  only depend on the dielectric constant, the axis ratio, and the falling behavior. Thus, the input parameters that are not specified by the mesoscale model are especially important for the computation of the polarimetric signatures. In order to allow the use of SynPolRad for the evaluation of microphysical parameterization schemes these free parameters have to be defined such that the resulting synthetic observables are consistent with typical observed values for the given hydrometeor types respecting the assumptions of the NWP model. Therefore, three different sources of information are available to constrain the free parameters. First, the assumptions of the mesoscale model regarding the density of the ice particle which is normally given in order to compute its terminal falling velocity. Second, the ranges and thresholds of the polarimetric quantities  $L_{DR}$  and  $Z_{DR}$  provided by a hydrometeor classification scheme for the determination of the predominant hydrometeor type within a radar volume (Höller et al. (1994), see Section 2.3.2). And, third, the findings of the sensitivity study discussed in the last section. The idea in the following derivation of the free parameters is to constrain the free parameters for a given hydrometeor type using the assumptions of the NWP model regarding density and the information from the sensitivity study to match the thresholds of the classification scheme.

As stated previously, the free parameters only impact the simulation of the polarimetric quantities. The sensitivity study showed further that  $L_{DR}$  and  $Z_{DR}$  only depend on the dielectric constant, the shape, and the falling behaviour of the particle but not on the particle spectrum. Assuming that snow and graupel are dry, the dielectric constant is only a function of ice density which is defined by the NWP model. Then, the remaining free parameters in the simulations of the polarimetric quantities are the axis ratio and the falling behavior of the hydrometeor. Assuming now that the axis ratio of a given hydrometeor type is constant and doesn't vary with diameter, a pair of fixed values for the axis ratio and the maximum canting angle can be defined such that the resulting values of synthetic  $L_{DR}$  and  $Z_{DR}$  will always range within the thresholds of the hydrometeor classification. This will be accordingly to the model assumptions regarding the prescribed ice density for the given hydrometeor type. Thus, for every ice hydrometeor type, the free parameters can be defined such that the resulting synthetic polarimetric parameters will always match the hydrometeor

classification independently on the amount of the bulk water quantity or the surrounding meteorological conditions. This is possible because both, the hydrometeor classification scheme as well as the method for the determination of the free parameters are only based on  $L_{DR}$  and  $Z_{DR}$ , which are independent of the particle spectrum and, therefore, the strength of the precipitation event. Possible sets of input parameters for a given hydrometeor type can be extracted easily from the output of the sensitivity study using data base queries. In the following the derivation of the free parameters for the precipitating ice hydrometeors in the LM will be discussed for illustration.

### Graupel

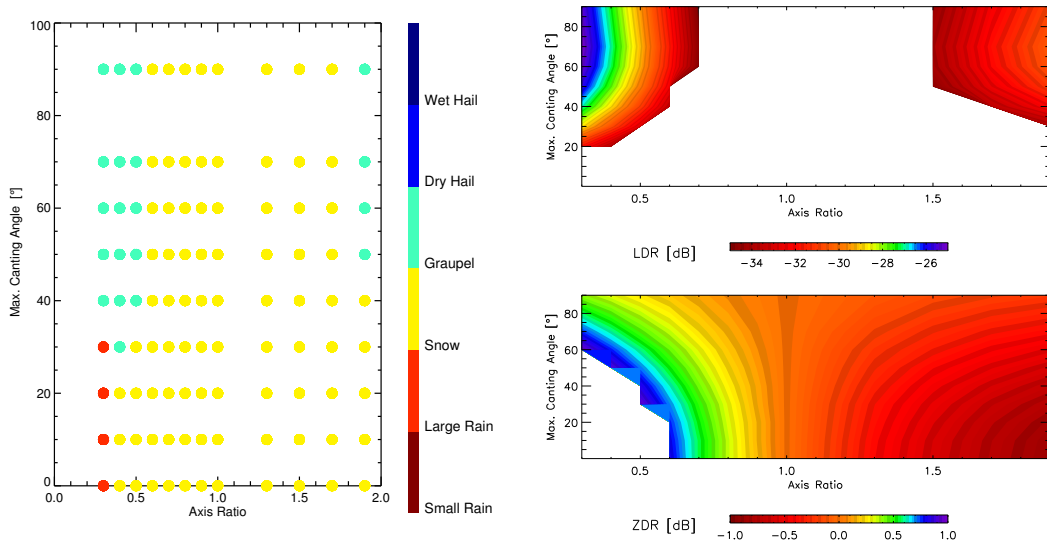


**Figure 4.5:** Left: Classification of hydrometeors as a function of axis ratio and maximum canting angle for a fixed density of  $\rho = 0.2 \text{ g cm}^{-3}$ . Right: Variability of  $L_{DR}$  and  $Z_{DR}$  as a function of axis ratio and maximum canting angle. Shown are only values within the thresholds for graupel from the hydrometeor classification scheme.

The input parameters of the sensitivity study in the last section were chosen to represent the whole range of ice hydrometeors in the atmosphere and can, therefore, be used for the determination of the free parameters. In the LMK, graupel is described as an ice hydrometeor with a fixed density of  $0.2 \text{ g cm}^{-3}$ . Extracting from the database all simulations of the sensitivity study performed for this prescribed density gives the ranges of  $L_{DR}$  and  $Z_{DR}$ , a graupel particle can assume accordingly to the LMK specifications. These values of  $L_{DR}$  and  $Z_{DR}$  only depend on the shape and the maximum canting angle of the particle because both quantities are independent of PSD and the dielectric constant is defined through the density assuming that the particle is dry. Applying the hydrometeor classification to the results of the sensitivity study for the prescribed density, possible combinations for the free parameters resulting in a classification as a graupel particle can easily be derived from Figure 4.5. The hydrometeor classification is given as a function of maximum canting angle  $\vartheta$  and axis ratio  $\alpha$  derived from the sensitivity study for the prescribed graupel density of  $0.2 \text{ g cm}^{-3}$ . For

illustration the variability of the related values of  $L_{DR}$  and  $Z_{DR}$  are also shown within the thresholds of the classification as a graupel particle. Only particles with an axis ratio of 0.5 or smaller and a canting angle of at least  $30^\circ$  were classified as graupel. For smaller canting angles or more spherical particles, thus, larger axis ratio, the particle is classified as rain because the values of  $L_{DR}$  are too small. For future simulations of graupel, an axis ratio of 0.4 and a maximum canting angle of  $40^\circ$  (similar to the  $45^\circ$  used by Vivekanandan (1986)) were chosen.

## Snow

In the LMK, snow is characterized as a densely rimed aggregate of dendrites with a maximum linear dimension  $D_s$ . In order to calculate the density of a single snow crystal, the following mass size relationship according to the LMK microphysical scheme (Doms and Schättler (1999)) is used:

$$m_s = a_m^s D_s^2. \quad (4.1)$$

This mass size relationship gives a decreasing density of the aggregate with increasing diameter using the constant form factor  $a_m^s = 0.038 \text{ kg m}^{-2}$ . Defining an axis ratio  $\alpha$  and assuming cylindrical shape allows for the calculation of the snow density via the volume of the cylinder:

$$\rho = \frac{4}{\pi \alpha D} a_m^s. \quad (4.2)$$

In the hydrometeor classification, the thresholds for snow are quite low with  $Z_{DR} \leq +1 \text{ dB}$  and  $L_{DR} < -35 \text{ dB}$  and can be reached by a large combination of input variables. This is due to the fact that the dielectric constant of snow is so small that almost no polarimetric signatures are produced and, therefore, the shape of the particles is of minor importance. In order to describe snow as a relatively flat particle, an axis ratio of 0.3 and a maximum canting angle of  $20^\circ$  were chosen. These values resulted in all combinations with densities smaller than  $0.2 \text{ g cm}^{-3}$  and for all  $D_o$  and  $N_o$  in a classification as snow particles.

In the last Section, the free parameters for the calculation of polarimetric quantities from ice hydrometeors were derived for the LMK. The determination of the free parameters was based on three sets of different information namely the ice density from the NWP model, the typical thresholds for the polarimetric radar quantities from the hydrometeor classification, and the results from the sensitivity study presented in Section 4.2. Furthermore, it was assumed that the particles are dry and that the axis ratio doesn't vary with diameter. This method for determining the free parameters has been applied on all microphysical schemes introduced in Section 2.2.2. In the case of wet particles as for example the hail class predicted in the MesoNH, another sensitivity study has been carried out varying the water content of the particle and, thus, its dielectric constant. The free parameters were then determined in the same way as in the case of dry particles. The parameters used for the computation of synthetic polarimetric radar variables out of LMK forecasts are summarized in Table 4.2 while the results for the other microphysical schemes can be found in Appendix B.

	Rain	Snow	Graupel
$N(D)$	$N_o \exp(-\lambda D)$		
$N_o$ [ $\text{mm}^{-1} \text{m}^{-3}$ ]	8000	800	4000
$\lambda$	$\left(\frac{\pi \rho_w N_o}{\rho q_r}\right)^{1/4}$	$\left(\frac{\pi \rho_s N_o}{\rho q_s}\right)^{1/3}$	$\left(\frac{\pi \rho_g N_o}{\rho q_g}\right)^{1/4}$
Axis Ratio	f(D)	0.3	0.5
Maximum Canting Angle	10°	20°	40°
$\Delta\vartheta$	5°	10°	20°
Brightband			
Water portion [%]		36	36
Maximum Canting Angle		60°	60°
$\Delta\vartheta$		45°	40°

**Table 4.2:** SynPolRad input parameters for the computation of synthetic polarimetric quantities from LMK forecasts.

## 4.4 Melting Ice and Brightband Effects

A prominent feature in radar meteorology is the so called bright band describing a rapid increase of reflectivity and polarimetric variables within the region of the melting layer. Figure 4.6 shows measurements (Hagen et al. (1993)) of a typical vertical cross section of polarimetric radar quantities throughout the melting level with large discontinuities in reflectivity,  $L_{DR}$ , and  $Z_{DR}$ . The bright band results from the enhanced dielectric constant

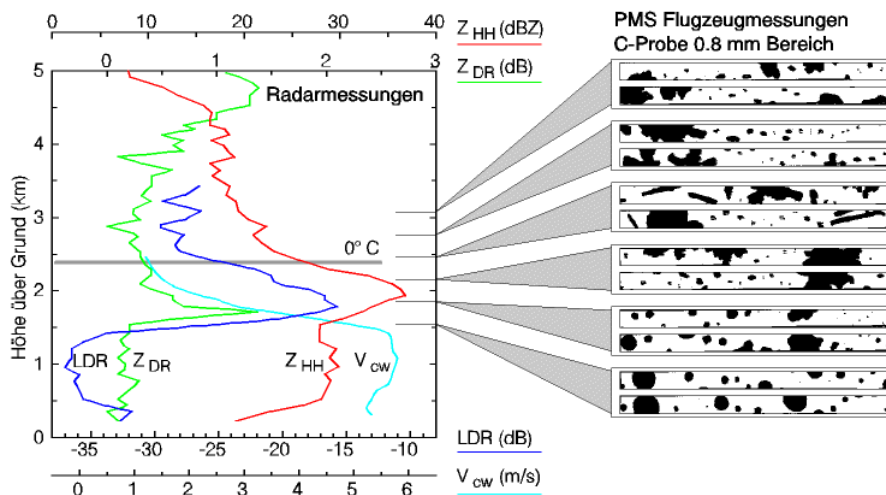


**Figure 4.6:** Vertical profiles of  $Z_{HH}$  [dBZ],  $L_{DR}$  [dB],  $Z_{DR}$  [dB], and terminal falling velocity  $V_{cw}$  [ $\text{m s}^{-1}$ ] measured by POLDIRAD together with particle images recorded by the PMS 2D cloud particle probe measurements (0.8 mm range) on board of the DLR Falcon aircraft (Hagen et al. (1993)).

of melting ice. Ice particles falling beneath the 0° C isotherm start to melt slowly. A water coat evolves around the ice crystal increasing the dielectric constant massively while the crystal size diminishes very slowly through melting. This gradient in reflectivity is further

Variable	Range	Intervals
$N_o$ [ $\text{mm}^{-1} \text{m}^{-3}$ ]	800	1
$D_o$ [mm]	1 – 8	7
Density [ $\text{g cm}^{-3}$ ]	0.2	1
Axis Ratio	0.3	1
Max. Canting Angle [ $^\circ$ ]	0 – 90	10
$\Delta\vartheta$ [ $^\circ$ ]	10 – 45	5
Water portion [%]	10 – 40	16

**Table 4.3:** Range of input parameters used within the sensitivity study for melting ice hydrometeors.

enhanced due to changes in the snow spectrum above the melting layer because of aggregation and below the melting layer because of the rapid outfall of the smaller and heavier rain drops. This results in higher precipitation fluxes in this zone below the melting layer which diminishes reflectivity. The vertical profile shows that the peak values of  $Z_{HH}$ ,  $L_{DR}$ , and  $Z_{DR}$  appear at different heights. Maximum  $Z_{HH}$  is caused by the largest particles. Maximum  $L_{DR}$  indicates heavy tumbling wet ice particles whereas maximum  $Z_{DR}$  is reached when oblate particles are orientated horizontally. The  $L_{DR}$  peak is observed at higher altitudes than the  $Z_{DR}$  peak. This indicates that melting particles are first tumbling and later fall horizontally aligned. The fall velocity is increasing through the melting layer until all particles have been melted and only drops are present.

There are already many studies coupling a melting model with a cloud model and simulating reflectivity in order to better understand the microphysical processes within the melting layer (e.g. Klaassen (1988), Szyrmer and Zawadzki (1999), Fabry and Szyrmer (1999), Olson et al. (2001)). In contrast to these process studies, SynPolRad aims to evaluate the model microphysical schemes and, therefore, no extra melting model is included in the forward operator. Nevertheless, melting has to be considered to reproduce the typical radar signals especially in  $L_{DR}$  and reflectivity within the regions of the brightband.

In the LMK, melting is described as a transition from snow to rain with coexisting snow and rain phase. This means that no extra hydrometeor class for melting snow is included and that the model assumptions for the PSD of snow are still valid below the  $0^\circ \text{C}$  isotherm. Therefore, the free parameters of snow were newly defined in the case that snow exists below the  $0^\circ \text{C}$  isotherm to reproduce the typical brightband signatures. To reach  $L_{DR}$  values of  $-15 \text{ dB}$ , either the axis ratio can be decreased, the canting angle can be increased, and/or a water portion can be added to the ice hydrometeor. Decreasing the axis ratio would contradict observations. Fujiyoshi (1986) found that the axis ratio of melting snow should increase towards lens-shape. For that reason, the axis ratio of melting snow was not changed but a water portion was added to the ice particle. Furthermore, the maximum canting angle and its standard deviation were increased to consider that melting ice hydrometeors tumble more strongly because of the changing interactions of the water shell with the surrounding flow.

In order to determine the best volume fraction of water as well as the best canting angle for the representation of polarimetric radar quantities in the region of the melting layer, another sensitivity study was carried out with the focus of explaining  $L_{DR}$  values up to  $-15 \text{ dB}$ . The water portion was changed from  $10 - 40\%$  in increments of  $2\%$ , the maximum canting angle

from  $20 - 90^\circ$  in increments of  $10^\circ$ , and the standard deviation from  $10 - 45^\circ$ . The results from Section 4.2 showed a slight dependence of  $L_{DR}$  on mean diameter and, therefore,  $D_o$  has also been varied within the range from the previous sensitivity study. The other parameters were held fixed at typical values for snow with  $N_o$  at  $800 \text{ mm}^{-1} \text{ m}^{-3}$ , a density of  $0.2 \text{ g cm}^{-3}$ , and an axis ratio of 0.3 (see also Table 4.3).

Figure 4.7 shows  $L_{DR}$  as a function of the maximum canting angle  $\vartheta$  and its standard deviation  $\Delta\vartheta$  at the left, and  $L_{DR}$  as a function of water portion and maximum canting angle at the right. Due to the fact that  $L_{DR}$  is the cross correlation of  $Z_{HH}$  and  $Z_{VV}$ , it will be maximum per definition if most part of the hydrometeors of the ensemble are aligned at or near a canting angle of  $45^\circ$ . This is achieved for maximum canting angles  $\vartheta$  of  $60 - 70^\circ$ , and  $\Delta\vartheta = 45^\circ$  (Figure 4.7, left). The right figure shows that  $L_{DR}$  increases with the water portion but that its maximum values are reached for a given water portion for the same range of maximum canting angles  $\vartheta = 60 - 70^\circ$ . Therefore, in the future, the combination of  $\vartheta = 60^\circ$  and  $\Delta\vartheta = 45^\circ$  will be used to maximize  $L_{DR}$  in the region of the brightband.

Figure 4.8 shows reflectivity and  $L_{DR}$  as a function of  $D_o$  and the water portion in melting

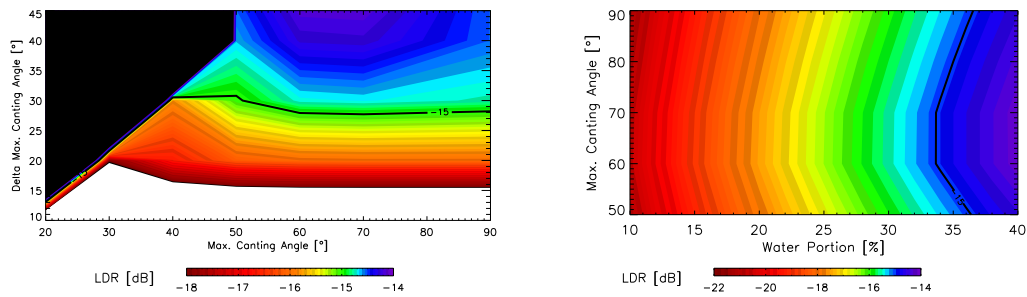


**Figure 4.7:** Left:  $L_{DR}$  [dB] as a function of the maximum canting angle  $\vartheta$  and its standard deviation  $\Delta\vartheta$  for a fixed water portion of 40%. Right:  $L_{DR}$  [dB] as a function of maximum canting angle  $\vartheta$  and the water portion [%] in melting ice. The chosen threshold of a  $L_{DR}$  value of  $-15$  dB is given as a black graph.

ice. Both,  $Z_{HH}$  and  $L_{DR}$  increase significantly with the water portion of the melting snow particle while  $L_{DR}$  is almost independent of the mean diameter in contrast to reflectivity. In order to reach values of  $L_{DR}$  up to  $-15$  dB, the water portion has to be at least 36%. At the same time, it should be chosen as small as possible in order to avoid unnatural high values of reflectivity. These high values of reflectivity are possible because the PSD of snow is not adapted to melting processes including for example break up processes and, therefore, large particles contribute strongly to reflectivity without affecting  $L_{DR}$ . Therefore, in the future the free parameters of melting ice hydrometeors are set to a maximum canting angle  $\vartheta$  of  $60^\circ$  with a standard deviation of  $45^\circ$ , and the particles are assumed to consist of 36% of water.

## 4.5 Evaluation of SynPolRad

Before employing the polarimetric radar forward operator SynPolRad for model evaluation purposes, its reliability has to be discussed especially regarding the consistency of the assumptions made in the derivation of the free parameters. Assessing the performance of

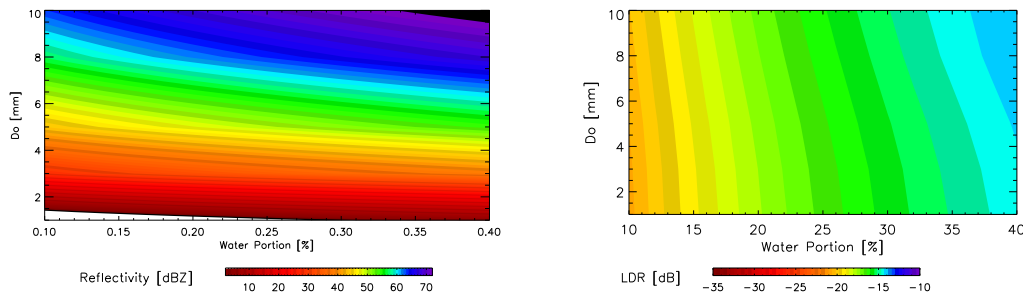


**Figure 4.8:** Reflectivity [dBZ] and  $L_{DR}$  [dB] as a function of the mean diameter [mm] and the water portion [%].

SynPolRad is a difficult task because a forward operator doesn't try to reproduce the true world but rather the model's reality which depends on the model's perception and description of nature. Thus, the forward operator creates a synthetic image of a synthetic reality which can not be compared against real observations as already the model's reality doesn't match the truth. The only way to evaluate SynPolRad is to assess the reliability of its single components (see Chapter 3) and test the consistency of the assumptions employed in the development of the forward operator comparing the synthetic observables against the truth of the model.

The heart of SynPolRad consists of the T-Matrix scattering code which has been evaluated against polarimetric radar observations and in-situ aircraft measurements during several campaigns. Vivekanandan (1986) compared simulations of polarimetric signatures of melting graupel to aircraft measurements by the Wyoming King Air penetrating convective storms during the MAYPOLE experiment held in Colorado in 1983. The same scattering code was employed by Dölling (1997) for the simulations of polarimetric quantities from ensembles of tumbling and melting ice particles. The results of the simulations were compared against polarimetric radar measurements by POLDIRAD as well as aircraft measurements by the DLR Falcon during the CLEOPATRA experiment in summer 1992 over southern Bavaria. During the two experiments, the aircrafts were equipped with a pair of orthogonally mounted 2D-PMS precipitation probes providing information on particle type, size, shape, and phase. The comparisons of the modeling results showed good correspondence with both, polarimetric radar as well as aircraft observations for reflectivity and polarimetric parameters. This was especially true for the particle shapes derived from the application of the modeling results to the polarimetric observations in comparison to the ones observed by the aircraft.

For the description of beam propagation and attenuation in the model domain, SynPolRad employs the methods developed for the conventional radar forward operator RSM which are discussed and evaluated by Haase (1998) and Haase and Crewell (2000). The correct implementation of the T-Matrix scattering module into SynPolRad was tested comparing synthetic reflectivities derived from the RSM to the ones provided by SynPolRad. For rain, the synthetic reflectivities agreed well, while the intensities simulated from ice hydrometeors showed larger discrepancies due to the more sophisticated treatment of the dielectric constant in SynPolRad. Applying the same dielectric constants to the two forward operators

gave again a good correspondence proving that the T-Matrix scattering module was correctly implemented and that the assumptions concerning the free parameters did not disturb the simulations of reflectivity.

Regarding the synthetic polarimetric quantities, an evaluation as in the case of reflectivity is not possible because of missing references for comparisons. However, the consistency of the assumptions employed in SynPolRad can be tested. The polarimetric signatures strongly depend on the free parameters which were defined earlier on theoretical terms demanding that the resulting synthetic polarimetric quantities match the thresholds provided by the

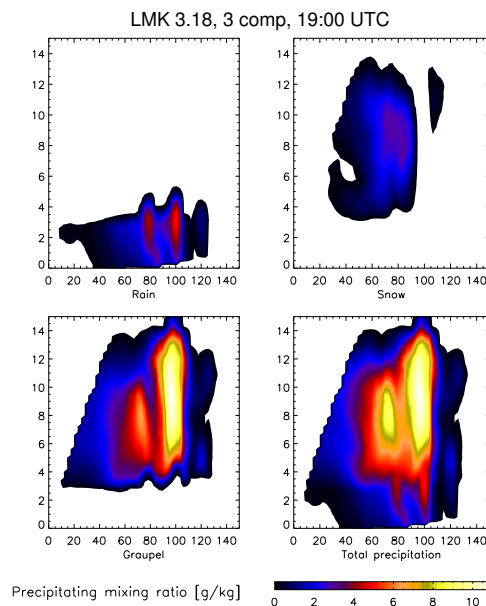


**Figure 4.9:** Vertical cross section of precipitation mixing ratios [ $\text{g kg}^{-1}$ ] for the single hydrometeor types and total precipitation at 19:00 UTC on August 12th, 2004 (LMK 3.18, 3 component scheme).

hydrometeor classification under consideration of the model assumptions. The derivation of the free parameters was possible because the sensitivity study had shown the independence of the polarimetric parameters on DSD and, therefore, the meteorological conditions in the case that the axis ratio of the particles is fixed. The validity of this hypothesis and the other assumptions regarding the derivation of the free parameters of the single hydrometeor types can be proved applying SynPolRad on a case study and simulating the synthetic polarimetric parameters only considering one hydrometeor type at the same time setting the other hydrometeor types to zero. If the assumptions are valid, the resulting synthetic parameters will match the thresholds of the classification scheme for the given hydrometeor type.

This consistency test of SynPolRad is performed simulating synthetic polarimetric radar quantities from a convective case study including significant amounts of rain, snow, and graupel. Figure 4.9 shows the precipitation mixing ratios for a vertical cross section derived from the LMK 3.18 forecasts considering the 3 component scheme at 19:00 UTC on August 12th, 2004. Details about the model set up and a detailed discussion of the case study can be found in Chapter 6. The mixing ratios of the three precipitating hydrometeor types rain, snow, and graupel are shown separately as well as the sum of these mixing ratios giving the

total precipitation. The precipitation shows a convective event with two cores of enhanced precipitation especially visible in the mixing ratios of graupel and rain. In the following the simulations for the single hydrometeors will be discussed separately starting with rain. Cloud water and cloud ice are not considered within SynPolRad as its impact on the radar quantities is very small at C band. This is confirmed for the given model run where a maximum cloud water content of  $2.42 \text{ g kg}^{-1}$  was produced by the model. This corresponds for the given wavelength of the radar to a reflectivity of  $-10.7 \text{ dBZ}$  and can, therefore, be safely neglected.

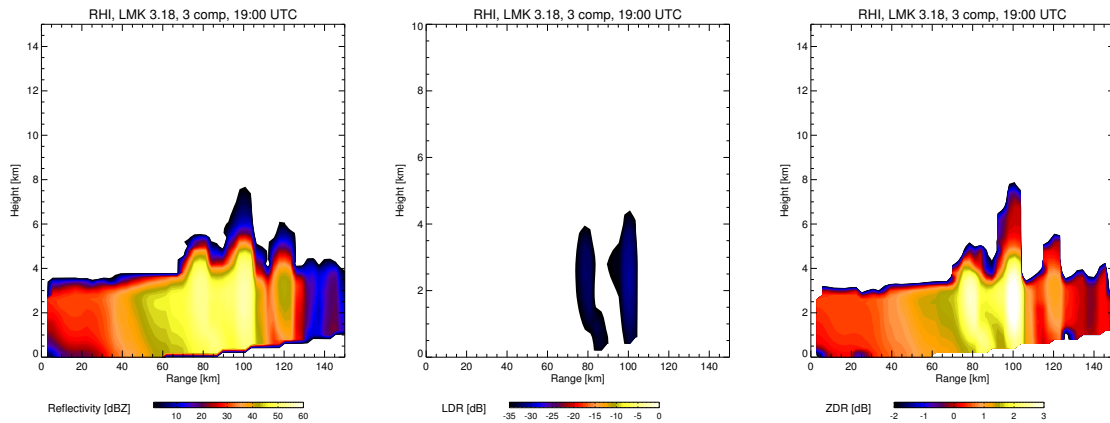


**Figure 4.10:** Synthetic RHI of reflectivity [dBZ],  $L_{DR}$  [dB], and  $Z_{DR}$  [dB] for rain.

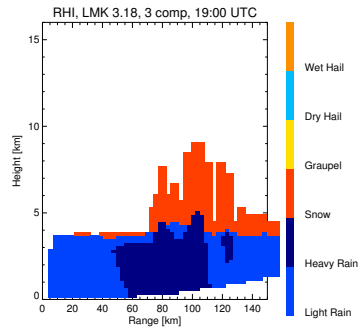


**Figure 4.11:** Hydrometeor classification derived from the synthetic polarimetric quantities for the SynPolRad simulations only considering rain.

Figure 4.10 shows the synthetic  $Z_{HH}$ ,  $L_{DR}$ , and  $Z_{DR}$  derived from the simulations only considering rain. The two cores of heavy precipitation appear in all synthetic radar parameters reaching values of  $55 \text{ dBZ}$  in reflectivity,  $-25 \text{ dB}$  in  $L_{DR}$ , and more than  $3 \text{ dB}$  in  $Z_{DR}$ . Within the convective cores of heavy precipitation, rain also exists above the melting layer because of the large updrafts in this part of the storm. Figure 4.11 shows the corresponding hydrometeor classification derived from the synthetic polarimetric quantities which result mainly in a classification as light rain. Within the convective core some signatures of heavy rain appear accordingly to the enhanced values of all synthetic radar parameters in

this region of the precipitation. The rain existing above the  $0^\circ$  C isotherm in the updrafts of the convective cores is classified as snow, as the hydrometeor classification scheme only differentiates between rain and snow via the height of the melting layer.

Regarding the snow phase, the vertical cross section of precipitation mixing ratios shows

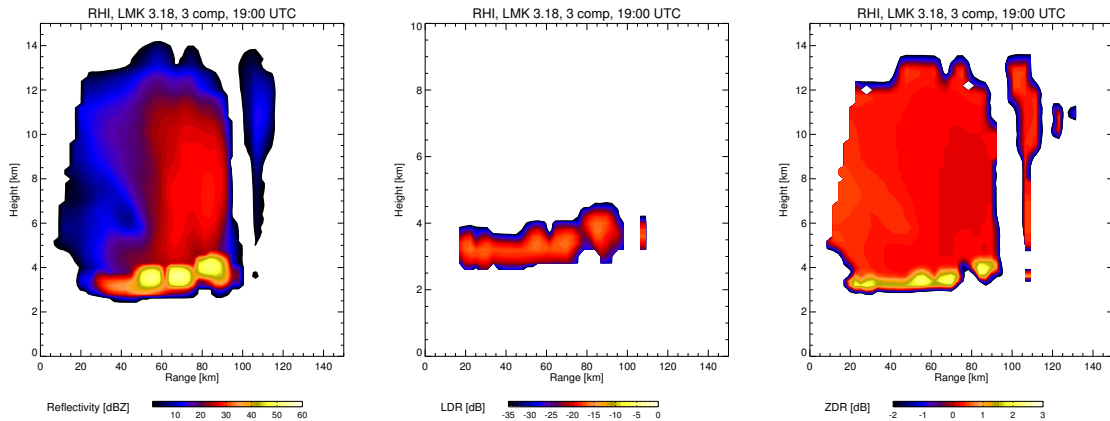


**Figure 4.12:** Synthetic RHI of reflectivity [dBZ],  $L_{DR}$  [dB], and  $Z_{DR}$  [dB] for snow.

significantly smaller maximum mixing ratios of snow as compared to rain. This is also true for reflectivity (Figure 4.12) where the intensities are decreased with values about 30 dBZ above the melting layer while the reflectivities within the brightband are in the same order as the maxima in rain reaching 50 dBZ. For the polarimetric radar quantities, the maximum values are also found in the region of the brightband reaching values of  $-15$  dB in case of  $L_{DR}$  and 2.5 dB in case of  $Z_{DR}$ . Thus, the synthetic values of  $L_{DR}$  reproduce well

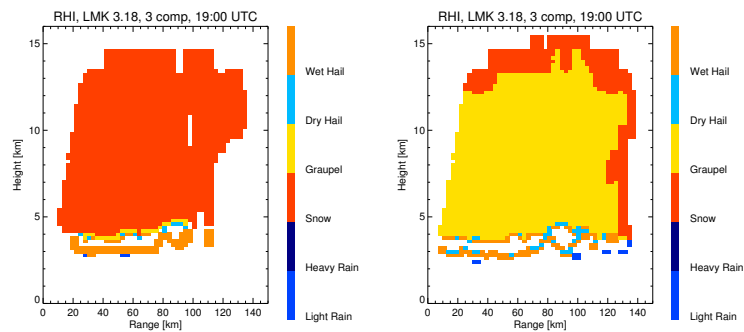


**Figure 4.13:** Hydrometeor classifications derived from the synthetic polarimetric quantities for the SynPolRad simulations only considering snow (left) and graupel (right).

the observed brightband signatures which proves that the SynPolRad assumptions regarding the representation of the melting layer are sensible. Comparing the hydrometeor classification to the actual precipitation fields and the synthetic radar quantities, the precipitation is classified everywhere as snow apart from the region of the brightband which is classified as graupel or wet hail due to the enhanced polarimetric quantities for melting snow. The remaining unclassified regions are due to missing definitions in the  $L_{DR} - Z_{DR}$  space of the

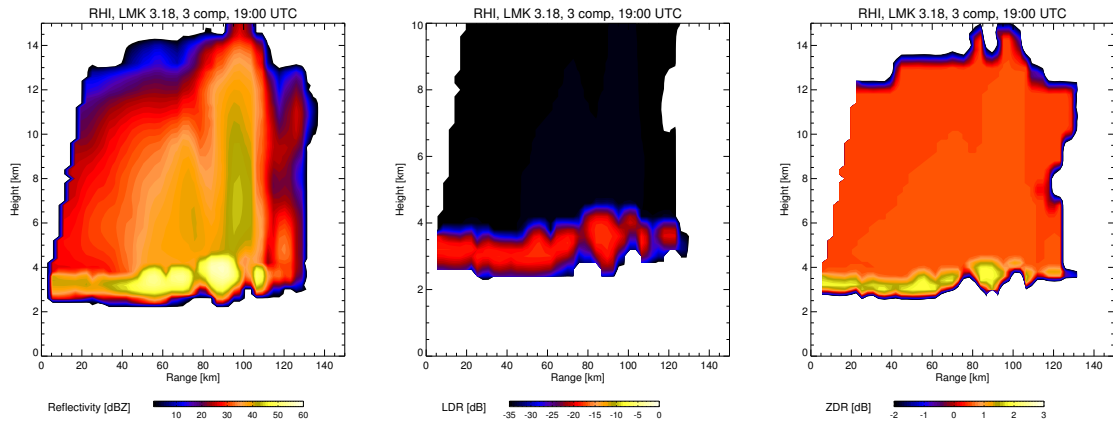


**Figure 4.14:** Synthetic RHI of reflectivity [dBZ],  $L_{DR}$  [dB], and  $Z_{DR}$  [dB] for graupel.

classification scheme.

The synthetic reflectivities derived from the simulations only considering graupel (Figure 4.14) reach intensities of 45 dBZ in the region above the melting layer. These are smaller than for rain although the graupel category produces the highest mixing ratios of all hydrometeor types, exceeding  $10 \text{ g kg}^{-1}$ . This is due to the dielectric constant of graupel which is smaller than the one for rain in the case of dry particles while it increases drastically for melting particles explaining the enhanced reflectivities in the brightband with values exceeding 50 dBZ. Regarding the polarimetric parameters, the values within the melting layer are comparable or slightly smaller as in case of snow. However, in the regions above the melting layer,  $L_{DR}$  and  $Z_{DR}$  show a notable increase due to the higher density of graupel and, therefore, the larger dielectric constant. According to the increased polarimetric quantities, the main part of the precipitation is classified as graupel (Figure 4.13) with signatures of heavier ice hydrometeors in the region of the brightband as it has already been shown in case of snow. Near the boundaries of the cloud, the precipitation is classified as snow which is due to the interpolation of the synthetic observables onto the model grid. Caused by the integration of empty cells into the interpolation, the polarimetric quantities are decreased resulting in a classification as a less densely rimed ice hydrometeor. As this procedure can be compared to radar measurements with only partial beam filling, the incorporation of empty model boxes and, hence, this misclassification is not inhibited artificially.

The simulations of the synthetic polarimetric quantities in the last section confirmed the consistency of the assumptions regarding the free parameters for the different hydrometeor types in a real case study. Now, the full precipitation field will be simulated considering all precipitating hydrometeors. Then, the impact of attenuation effects on the synthetic radar parameters and the hydrometeor classification will be discussed in detail. Figure 4.15 shows the resulting radar parameters with and without attenuation effects. In case of considering attenuation, all synthetic radar quantities are affected by the attenuation which is especially strong in the regions of heavy rain within the convective core and in the brightband. Behind these zones of enhanced attenuation, reflectivity and  $Z_{DR}$  are significantly decreased as compared to the synthetic RHI without attenuation effects while  $L_{DR}$  is significantly increased

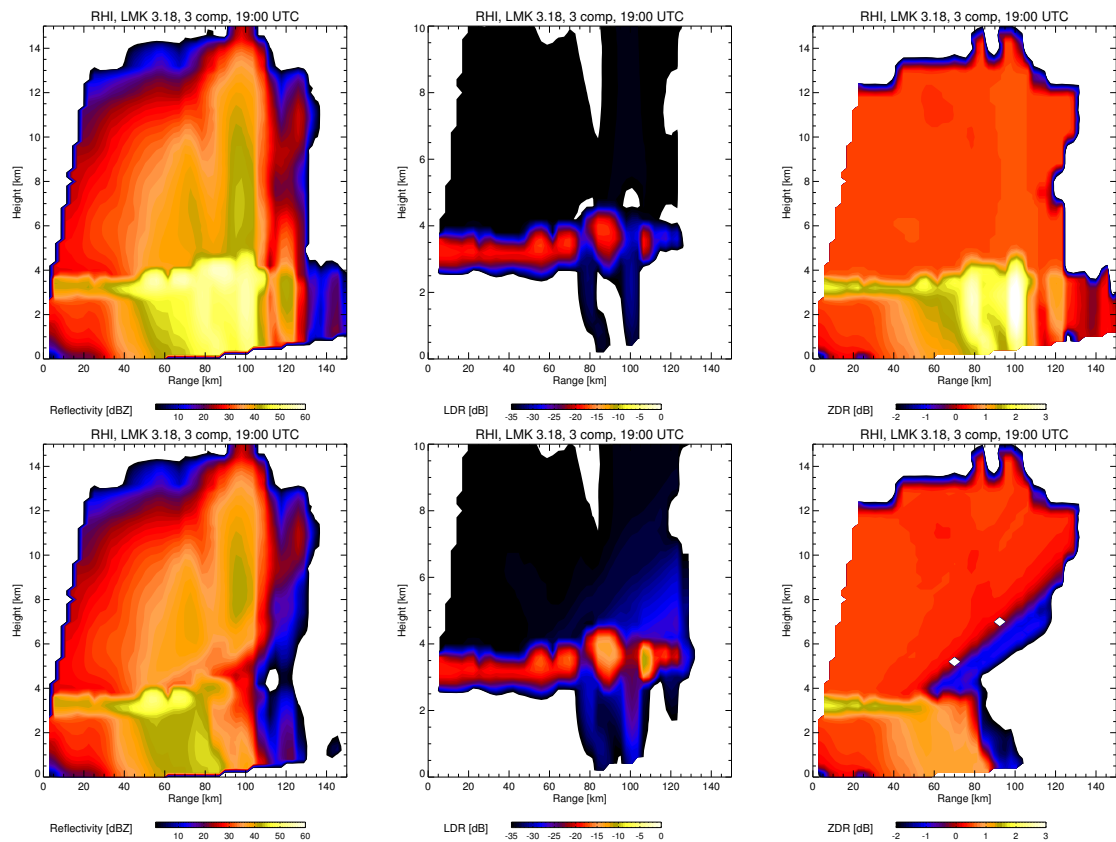


**Figure 4.15:** Synthetic RHI of reflectivity [dBZ],  $L_{DR}$  [dB], and  $Z_{DR}$  [dB] considering all precipitating hydrometeors in the upper row without and in the lower row with attenuation effects on August 12th, 2004 at 19:00 UTC.

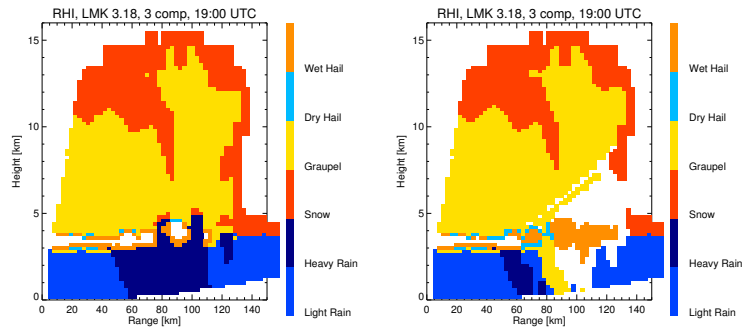


**Figure 4.16:** Hydrometeor classification derived from the simulations considering all precipitating hydrometeors (Figure 4.15) without (left) and with (right) attenuation effects at 19:00 UTC on August 12th, 2004.

according to Equations 3.26 – 3.28. Regarding the hydrometeor classification in Figure 4.16 major differences appear in the regions affected by the attenuation. The increased values of  $L_{DR}$  in rain result in a misclassification of heavy rain as graupel. Furthermore, large parts of the precipitation above the melting layer are not classified due to missing definitions in the classification scheme.

The last section tried to provide an evaluation of the polarimetric radar forward operator SynPolRad as far as this is possible for a virtual tool. The sensitivity study showed that polarimetric radar quantities are almost independent of PSD (Figure 4.2) and are, therefore, independent of the meteorological situation if a constant axis ratio is assumed as it is done in the assumptions regarding the ice phase in SynPolRad. This assumption was confirmed by a case study, where the application of the hydrometeor classification scheme on the synthetic polarimetric quantities proved the consistency and validity of the hypothesis applied in SynPolRad. Remaining discrepancies from the expected hydrometeor classification were explained with the enhanced polarimetric intensities in the brightband and decreased polarimetric quantities at the boundary of the precipitation field caused by the interpolation of the data onto the model grid. Finally, attenuation effects on the polarimetric data and the hydrometeor classification were discussed showing the possibility to produce signatures of highly rimed ice hydrometeors due to strongly attenuated and, therefore, enhanced  $L_{DR}$ . Concluding, the ability of the polarimetric radar forward operator SynPolRad to produce polarimetric quantities accordingly to the model assumptions was confirmed. Therefore, SynPolRad can be applied for the evaluation of microphysical parameterization schemes of NWP models. However, it also has to be stated that SynPolRad, because of the assumptions employed in the derivation of the free parameters, will not be able to simulate the natural variability of the polarimetric quantities as observed unless more of the free parameters are explicitly described by the NWP mesoscale model.

# Chapter 5

## Stratiform Case Study – 5 July 2005

After the successful implementation and evaluation of the polarimetric radar forward operator SynPolRad, the tool will be employed for assessing the forecast capabilities of the NWP models regarding the representation of precipitation for different meteorological situations. In this chapter, this will be done for a stratiform precipitation event because of the easier microphysical processes while the next chapter will concentrate on a convective case study. Stratiform comes from the Latin word 'stratus' meaning 'spread out' and is used in the meteorological context for spatially and temporarily homogeneous precipitation in contrast to convective precipitation. Stratiform precipitation is normally driven by large scale dynamics as for example fronts and is characterized by relatively small vertical motions. These small vertical velocities do not allow formation of heavily rimed ice species and therefore the microphysical processes involved in the formation of stratiform precipitation are relatively easy. Furthermore, the small vertical velocities and the spatial homogeneity of the precipitation fields allow the observation of brightband signatures in all radar quantities resulting from the transition from snow to rain in the region of the melting layer. The relatively easy microphysical processes together with the characteristics of the brightband make a stratiform precipitation event a perfect test case for a first look at the microphysical parameterization schemes in mesoscale models evaluating the radar signatures in snow and rain as well as the representation of the melting layer in the model and in SynPolRad.

The discussion will start with an evaluation of the representation of the life cycle and strength of the system. Then, major discrepancies between the observations and simulations will be discussed in more detail looking at  $1^\circ$  PPI scans. In the following section, the focus will be on the vertical distribution of reflectivity and polarimetric quantities with a special interest in the representation of the brightband. In general, the mesoscale model is expected to reproduce well a stratiform precipitation event because of the relatively easy microphysical processes. As no heavier ice species are expected to appear in the model forecasts due to the small vertical velocities, the differences between the LMK 2 and 3 component scheme should be marginal. However, larger discrepancies can be expected for the Thompson scheme as this microphysical parameterization scheme adapts the DSD of rain and snow to the meteorological situation.

## 5.1 Synoptic Overview, Observations, and Model Configuration

The morning of July 5th, 2005 was dominated by a stratiform rain event related to a cold front crossing Germany. Figure 5.1 shows the precipitation over Germany as observed by the German Radar composite at 8:00 UTC. The system was persistent during several hours without great variations in intensities and started to decay at noon. The observations showed enhanced brightband signatures in all polarimetric quantities. Later in the day, single convective cells evolved and the system began to decay. The POLDIRAD observations started with PPI overview scans at 1° elevation at 6:04 UTC and stopped at 14:39 UTC because of the already weak precipitation at that time. Dual polarization scans with elevations from

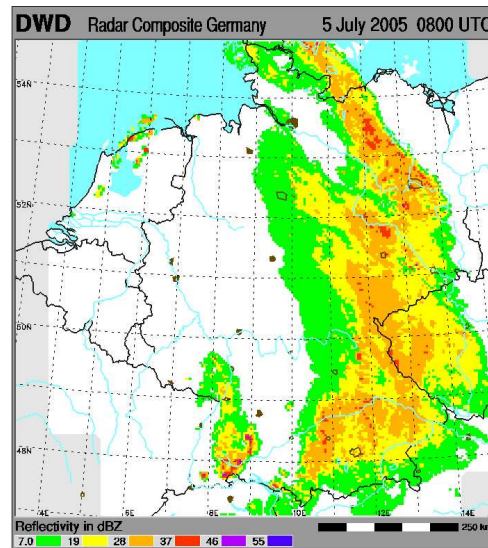


**Figure 5.1:** The distribution of precipitation shown in reflectivities [dBZ] on July 5th, 2005 over Germany as observed by the German radar composite at 8:00 UTC.

1–11° and a maximum range of 120 km were performed from 8:01 to 14:30 UTC. Within this case study, hourly simulations with the LMK test versions 3.16 and 3.17 will be evaluated considering the LMK 2 and 3 component as well as the Thompson scheme (only available for LMK 3.17). The main differences between the model versions are in the newly implemented shallow convection scheme in the model version 3.17. The simulations were initialized at 0:00 UTC with boundary conditions from the LM driven by the GME. The LMK was operated at a horizontal resolution of 2.8 km on a domain encompassing 100 x 100 x 40 grid points centered over Munich airport.

## 5.2 Evaluation of the Life Cycle and Intensity

The temporal evolution and intensity of the precipitation event will be evaluated in terms of histograms of reflectivities derived from 1° PPI scans. This is possible because the observed

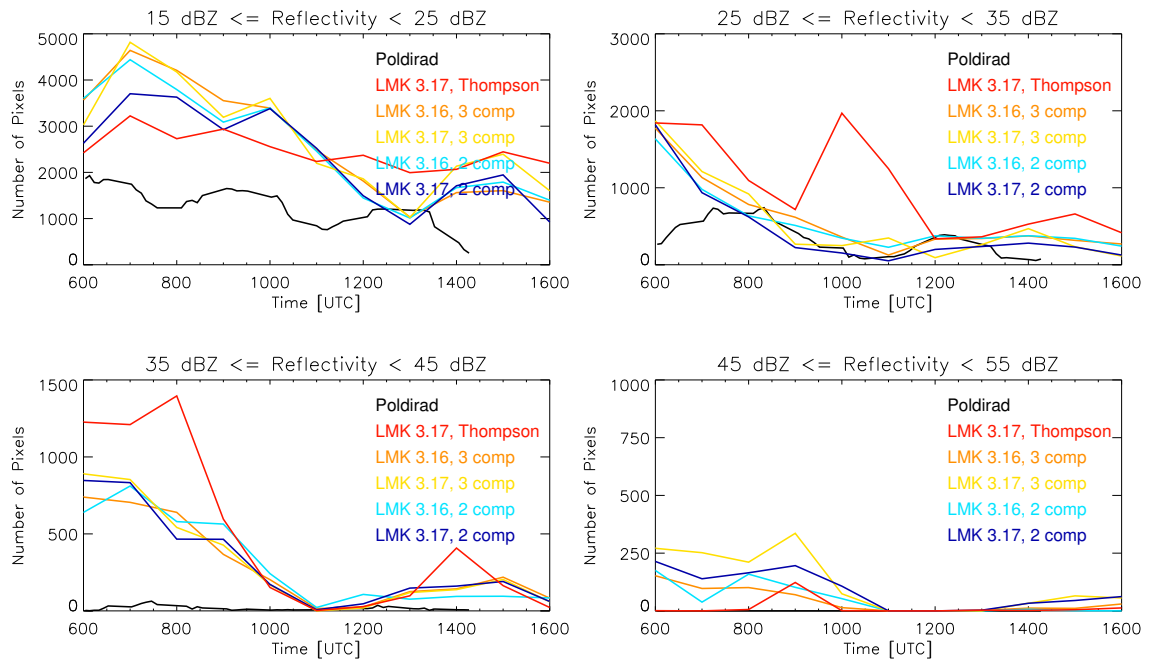


**Figure 5.2:** Time series of histograms of observed and simulated  $1^\circ$  PPI scans in different classes of reflectivity [dBZ] for July 5th, 2005.

and simulated  $1^\circ$  PPI scans are given on the same model grid and, therefore, the same spatial resolution which allows a direct comparison of the simulated and observed intensities looking at the numbers of pixels within a predefined reflectivity class. The formation and decay of the precipitation event can then be represented by the temporal evolution of the total numbers of observed and simulated pixels for the different classes of reflectivity given as time series of histograms. The reflectivity classes discussed in the following range from 15 – 25 dBZ having typical values for heavy snow or light rain, 25 – 35 dBZ for heavy rain, 35 – 45 dBZ for brightband values or smaller convective cells, and 45 dBZ and more for convective cells including graupel or hail. There will be no discussion of lower values of reflectivities due to the uncertainties in the observations at such small reflectivities and the small information content of this reflectivity class.

Figure 5.2 shows the time series of histograms derived from observed and simulated  $1^\circ$  PPI scans in different classes of reflectivity starting at 6:00 UTC with the begin of the POLDIRAD observations until 16:00 UTC when the system had totally decayed in the observations. The life cycle of the system is especially well documented in the lower reflectivity classes while almost no observations with reflectivities higher than 35 dBZ occurred. The reflectivity class of 15 – 25 dBZ is the class with the most pixels in the observations. Starting at 6:00 UTC with nearly 2000 pixels, the number decreases almost steadily as the system decays reaching less than 500 at 14:20 UTC when the observations stopped. In the reflectivity class from 25 – 35 dBZ, the numbers of pixels observed by POLDIRAD are substantially smaller increasing slightly from 300 to 800 from 6:00 to 8:00 UTC and later decaying to less than 500 for the rest of the period.

In the simulations, during almost the whole period, the total numbers of pixels are strongly overestimated for all classes of reflectivity and all model configurations. This is especially

true for the higher reflectivity classes where practically no observations occurred. However, for the lower reflectivity classes the simulated and observed graphs behave quite similarly showing that the decay of the system is captured by the model and that only its spatial extent is overestimated. This overestimation of spatial extent can be due to technical problems regarding the simulation of reflectivities at larger distances from the radar where smaller intensities in the observations are possible due to only partial beam filling which is not considered within SynPolRad.

Comparing the slopes of the curves, the numbers of pixels in the lowest reflectivity class derived from the LMK simulations considering the 2 and 3 component scheme decrease faster than seen in the observations apart from two peaks at 7:00 and 10:00 UTC. The Thompson microphysical scheme reproduces the observed slope of the curve almost perfectly. Regarding the higher reflectivity class from 25 – 35 dBZ, all simulations overestimate strongly the number of pixels until 8:00 UTC. However, in the following the simulations and observations almost coincide apart from a single peak produced at 10:00 UTC by the simulations considering the Thompson scheme. For the reflectivities between 35 and 45 dBZ, there is a strong overestimation from 6:00 to 10:00 UTC for all schemes. Furthermore, the very high reflectivities are only reproduced by the LMK schemes apart from a single peak at 9:00 UTC for the Thompson scheme. Concluding, the life cycle of the precipitation event with the decay in the early afternoon is well reproduced by the different model configurations. The major differences appear in the reflectivity classes from 25 – 35 dBZ and 35 – 45 dBZ between 6:00 and 8:00 UTC with strong overprediction by the model. As for the reflectivity class 25 – 35 dBZ, the peak in the Thompson scheme at 10:00 UTC and for the higher reflectivities the overprediction of the LMK schemes strikes most. The differences between the individual LMK versions remain small as compared to the differences resulting from the microphysical parameterization schemes and, therefore, the discussion will concentrate in the following on the LMK 3.17 model version. In order to understand the performance of the individual model configurations better, the 1° PPI scans at 8:00 and 10:00 UTC will be discussed in detail in the following section.

In the simulations, the early morning of July 5th, 2005 was characterized by a strong overprediction of intensities as compared to the observations. This has been already discussed in the last section and can also be seen in the 1° PPI at 8:00 UTC (Figure 5.3). The observation shows a stratiform precipitation event with a clear brightband signature. In the rain, the reflectivities range from 20 – 30 dBZ with increasing intensities in the region of the brightband reaching values of 35 – 40 dBZ. In the snow region, reflectivity diminishes to about 15 – 25 dBZ with smaller values at larger distances from the radar due to attenuation, beam height, and beam filling. In the observations, the maximum number of pixels is found at 5 dBZ reaching 220 pixels and the total number of pixels decreases almost steadily to higher reflectivities. Regarding the simulations, the three different model versions produce a stratiform precipitation event with a well defined brightband. However, there are substantial differences between the microphysical parameterization schemes and the observations. The precipitation in the models covers a larger area and for all model simulations applies that the height of the 0° C isotherm is overestimated and, therefore, the brightband appears at larger ranges from the radar and with a larger radius than in the observation. This overprediction of the spatial extent can also be seen in the histograms of reflectivity in Figure 5.3 showing

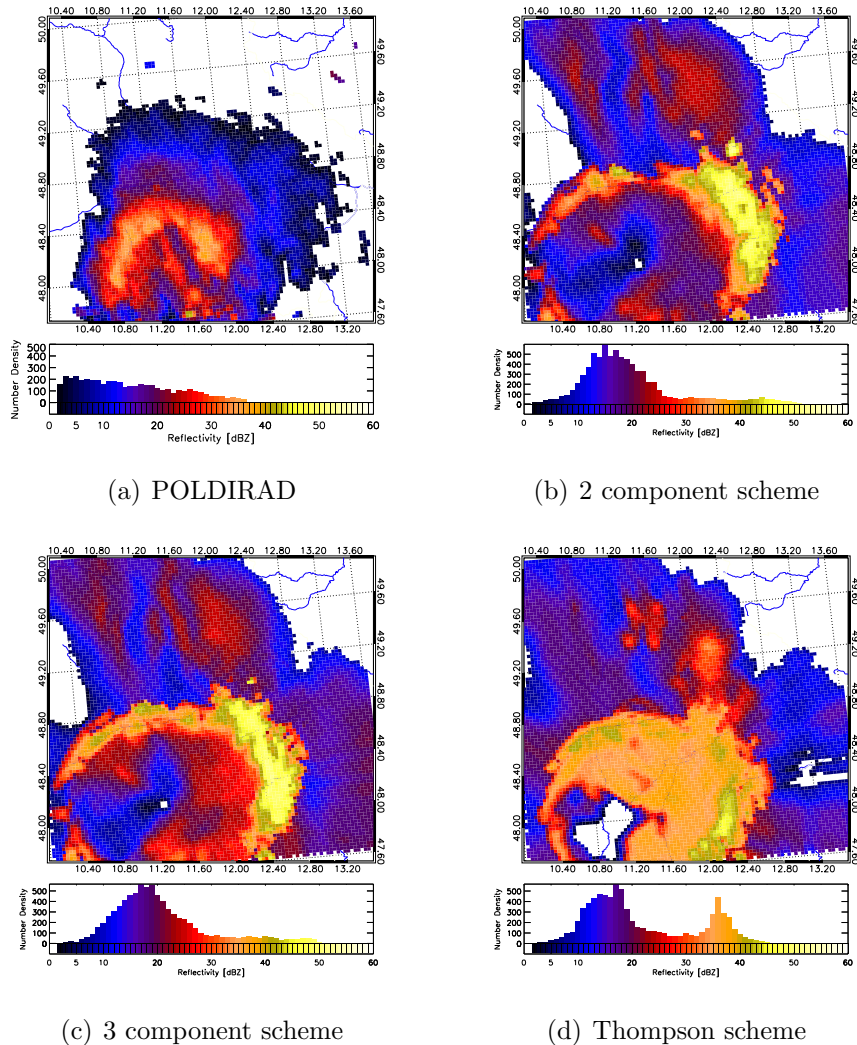


**Figure 5.3:** Observed and simulated  $1^\circ$  PPI scans of reflectivity [dBZ] at 8:00 UTC for July 5th, 2005 derived from simulations of the LMK 3.17 considering the 2 component, the 3 component, and the Thompson scheme. Below the figures, the legend gives colour coded reflectivity levels in dBZ as well as the number of pixels within the given reflectivity interval as a histogram.

an unimodal distribution for the LMK schemes with a two times larger number of pixels in the maximum reaching 500 pixels at 15 dBZ for the 2 component. The 3 component scheme produces a similar maximum at 18 dBZ while the Thompson scheme produces besides the same maximum at 18 dBZ, a second maximum at 36 dBZ.

Regarding the spatial distribution of reflectivities, the 2 component scheme underestimates  $Z_{HH}$  in the rain region while it reproduces well the intensities in snow and the brightband apart from a cell with enhanced reflectivities north east of the radar. In the simulations considering the 3 component scheme, the intensities in rain and the brightband are increased in comparison to the 2 component scheme, therefore, better reproducing the observed reflectivities in rain but overestimating the reflectivities in the brightband. The Thompson scheme represents well the intensities in the snow and the brightband but produces extreme reflectivities in the rainy region with more than 35 dBZ. The problems of the individual

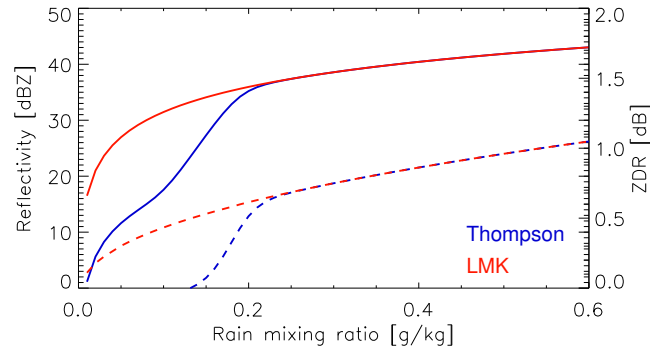


**Figure 5.4:** Reflectivity [dBZ] (solid line) and  $Z_{DR}$  [dB] (dashed line) for the LMK and the Thompson schemes as a function of rain mixing ratio [ $\text{g kg}^{-1}$ ].

parameterization schemes in reproducing the observed PPI scan explain for the discrepancies between the schemes already discussed in the time series of histograms of reflectivity. The overestimation of the spatial extent of the system which can be due to an overestimation of the height of the precipitation event as well as technical problems within SynPolRad regarding beam filling accounts for the increased number of pixels in the lower reflectivity classes appearing for all model versions. As for the higher reflectivity classes, the enhanced numbers of pixels result from the overpredicted intensities in the brightband for the LMK scheme and from the unnatural high reflectivities in rain for the Thompson scheme.

The extreme reflectivities in rain produced by the Thompson scheme are striking because these large discrepancies between the different microphysical parameterization schemes only emerge in the rain phase while the intensities in the snow and the brightband behave quite similarly for all model configurations. Two different explanations appear to be possible. Either the enhanced reflectivities in rain result from a different formulation of the rain DSD in the Thompson scheme which could have a major impact on  $Z_{HH}$  due to its dependence on the sixth power of diameter ( $Z_{HH} \sim D^6$ ) or the Thompson scheme produces substantially higher rain mixing ratios resulting in enhanced reflectivities in comparison to the LMK schemes. In the latter case, the question arises where these enhanced rain water contents originate as they do not appear to result from enhanced snow mixing ratios because of the comparable reflectivities in the ice phase for all microphysical schemes. Furthermore, the intensities in the brightband only appear to be overestimated for the LMK schemes and, therefore, the Thompson scheme seems to produce lower precipitation mixing ratios as compared to the LMK simulations.

In order to answer these questions, the formulation of the different microphysical parameterization schemes has to be reviewed (Section 2.2.2). Comparing the formulations and assumptions for the LMK and the Thompson schemes, major differences were found in the formulation of the DSD of rain and snow regarding the intercept parameter  $N_o$ . While in the LMK the intercept parameter is fixed at  $8000 \text{ mm}^{-1} \text{ m}^{-3}$  following Marshall and Palmer (1948), in the Thompson scheme  $N_o$  is defined as a function of the rain mixing ratio  $q_r$ . For  $q_r \geq 0.2 \text{ g kg}^{-1}$ , the formulation of the DSD is the same for the two schemes but for smaller values of  $q_r$  the Thompson scheme tries to reproduce the typical spectrum of drizzle

with extreme numbers of very small drops increasing  $N_o$ . To determine the impact of the different formulations of the rain DSD, reflectivity, and  $Z_{DR}$  were simulated as a function of rain mixing ratio following the assumptions of the Thompson and the LMK schemes (Figure 5.4). For  $q_r \leq 0.2 \text{ g kg}^{-1}$ , the Thompson scheme produces significantly smaller reflectivities and  $Z_{DR}$  values than the LMK scheme because  $N_o$  is increased and, therefore, the number of large drops is strongly reduced in this scheme. For  $q_r \geq 0.2 \text{ g kg}^{-1}$  which corresponds to a reflectivity of 36 dBZ, the assumptions regarding the DSD of rain and, thus, also the simulated values of  $Z_{HH}$  and  $Z_{DR}$  are the same for both microphysical parameterization schemes.

Figure 5.5 shows once again the  $1^\circ$  PPI scan of reflectivity for the 3 component and the

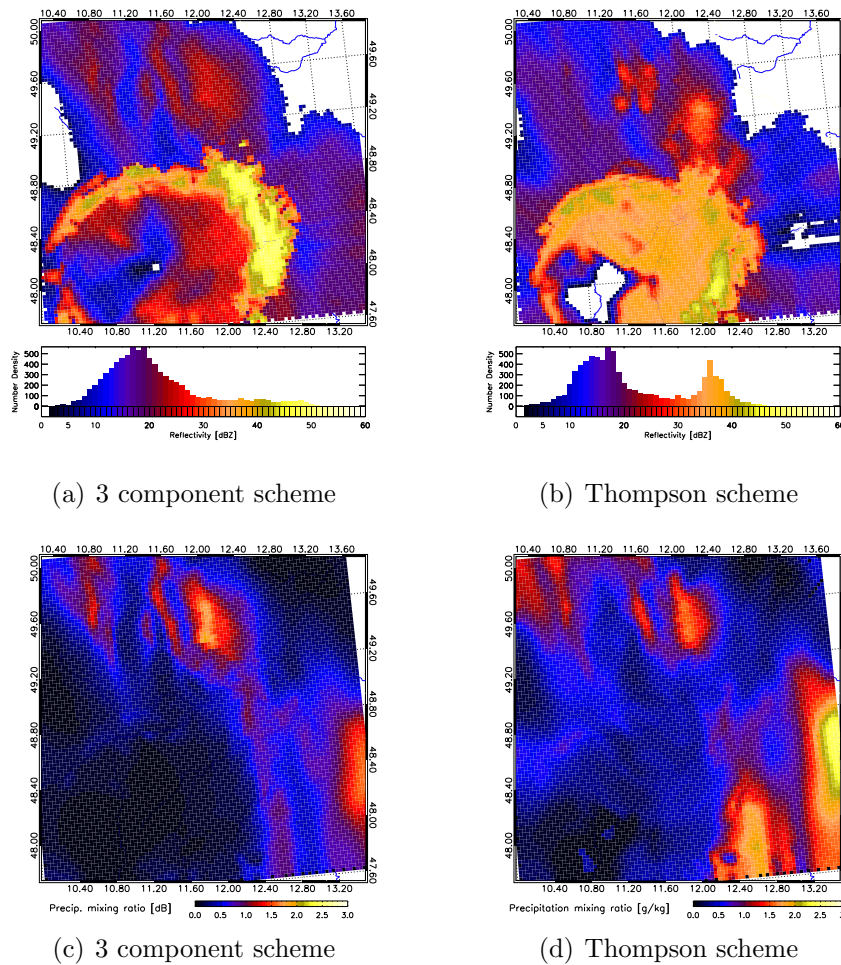


**Figure 5.5:** Synthetic  $1^\circ$  PPI scan of reflectivity [dBZ] (upper row) for the LMK 3.17 considering the 3 component and the Thompson scheme and the precipitating water mixing ratio [ $\text{g kg}^{-1}$ ] along the path of the radar beam for the two model configurations at 8:00 UTC.

Thompson scheme together with the precipitation mixing ratio along the path of the radar beam. For the Thompson scheme, the reflectivities in rain are larger than 36 dBZ marking the transition between the two formulations of  $N_o$ . Therefore, the differences in intensity between the LMK and the Thompson scheme can not result from differences in the formulations of DSD but are due to higher rain mixing ratios in the Thompson scheme. This is confirmed

by the  $1^\circ$  PPI scans of precipitation mixing ratios showing the sum of the mixing ratios of the different precipitating hydrometeors along the path of the radar beam. The Thompson scheme not only produces enhanced values in rain but also in the ice phase proving that the overestimation of the intensities in rain has its origin in the assumptions and source terms of the ice phase. New questions arise from this information regarding the synthetic reflectivities produced by the Thompson scheme. If the mixing ratios appear to be enhanced in the ice phase, why is this not the case for the reflectivities in snow and especially the brightband where even smaller intensities were reached as compared to the LMK schemes?

As it was stated in the beginning of this chapter, in stratiform precipitation no heavier ice hydrometeors are expected due to the small vertical velocities. Therefore, the differences between the microphysical parameterization schemes should be explained with the different assumptions regarding the representation of snow in the model. However, the assumption that only snow exists as a precipitating ice hydrometeor has to be proved because the smaller intensities in the brightband could also be a indicator for a more densely rimed ice particle falling faster than snow through the melting layer and, therefore, contributing less to reflectivity. To do so, the hydrometeor classification along the path of the radar beam derived from the synthetic polarimetric variables is shown in Figure 5.6. In the 3 component scheme, the precipitation is classified as rain and snow as expected for a stratiform precipitation event. Parts of the brightband are not classified by the scheme which is due to missing definitions in the  $L_{DR} - Z_{DR}$  space of the hydrometeor classification. In the Thompson scheme, most of the precipitation is classified as rain and snow but there also exist two cells attributed to graupel which are related to the regions of increased reflectivities in the  $1^\circ$  PPI scans. Furthermore, a large area east of the radar behind the brightband is classified as hail which is due to a misclassification.  $L_{DR}$  is increased because of attenuation effects in the melting layer and, therefore, graupel is classified as a more densely rimed ice particle. However, mainly it can be concluded that also in the Thompson scheme the snow dominates and that differences between the LMK and Thompson schemes should be explained with the different assumptions regarding the snow phase.

Two major differences exist in the description of snow in the LMK and the Thompson microphysical parameterization schemes. The first difference results in the formulation of density. While the LMK assumes a size dependent snow density where the density decreases with increasing diameter of the aggregate (see Equation 2.8), the density in the Thompson microphysical scheme is fixed at  $0.1 \text{ g cm}^{-3}$ . More important for the understanding of the discrepancies in reflectivity is the second difference regarding the formulation of snow PSD. In the Thompson scheme, the intercept parameter  $N_o$  and the slope  $\lambda$  of the PSD are defined as a function of temperature with  $N_o$  and  $\lambda$  decreasing for increasing temperature. This results in differences in  $N_o$  in the order of several magnitudes as shown in Figure 5.7 where  $N_o$  is given on a logarithmic scale as a function of temperature in comparison to the fixed  $N_o$  of the LMK scheme. Thus, the Thompson scheme produces for all temperatures smaller than  $0^\circ \text{ C}$  a much steeper PSD of snow than the LMK schemes which significantly affects reflectivity as shown in Figure 5.7. While in the LMK reflectivity only varies with the precipitation amount, in the Thompson scheme  $Z_{HH}$  increases with increasing temperature and snow mixing ratio but still produces significantly smaller intensities than the LMK scheme. The steeper PSD of snow in the Thompson scheme decreases the number of large particles strongly contributing to reflectivity which also explains why the intensities of reflectivity within the melting layer are more realistic although the snow mixing ratios are increased in

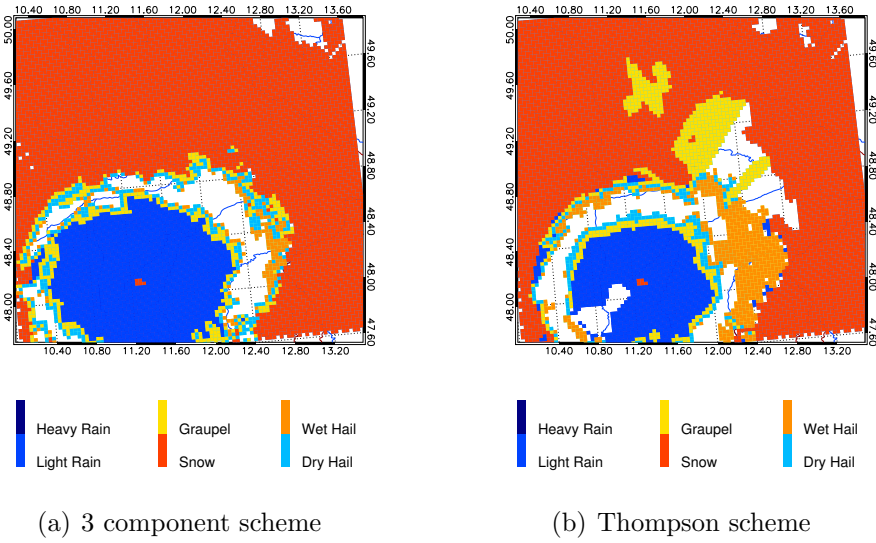


**Figure 5.6:** Hydrometeor classification derived from the polarimetric variables for the  $1^\circ$  PPI scan at 8:00 UTC for the LMK 3.17 simulations considering the 3 component scheme and the Thompson scheme.

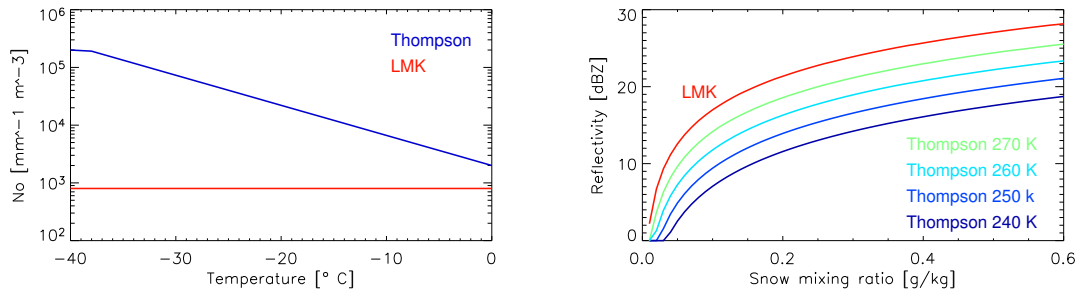


**Figure 5.7:** Left: The snow intercept parameter  $N_o$  [ $\text{mm}^{-1} \text{m}^{-3}$ ] as a function of temperature [ $^\circ \text{C}$ ] for the LMK and the Thompson scheme. Right: Reflectivity [dBZ] as a function of snow mixing ratio [ $\text{g kg}^{-1}$ ] and temperature [K] derived for the LMK 3 component and the Thompson scheme.

comparison to the LMK schemes.

The time series of histograms of reflectivity (Figure 5.2) showed more discrepancies between the individual microphysical parameterization schemes at 10:00 UTC when a major peak appeared in the reflectivity class from 25 to 35 dBZ for the simulation using the Thompson scheme. In the observed  $1^\circ$  PPI scan (Figure 5.8) the systems already decays west of the radar site while the brightband structure is still visible in the north east. Reflectivities range in the rain from 10 to 20 dBZ, in the brightband from 25 to 30 dBZ, and in the snow from 5 to 20 dBZ. In the simulations, the system has already vanished over the radar site apart from some single cells and there is a large band of precipitation extending from the north west to the south east of the model domain. In the region of the melting layer, reflectivity is increased with values higher than 40 dBZ for all model runs with the highest values for

the 2 component scheme and the lowest ones for the Thompson scheme. This is also true for the reflectivities in snow which range for the LMK schemes from 5 to 25 dBZ. The Thompson schemes simulates extreme values reaching 30 dBZ which are in the same order of the POLDIRAD brightband values. These enhanced reflectivities in snow also explain the peak in the histograms in the reflectivity class from 25 – 35 dBZ at 10:00 UTC for the LMK simulations considering the Thompson scheme.

Once again, the differences between the LMK schemes and the Thompson scheme are so

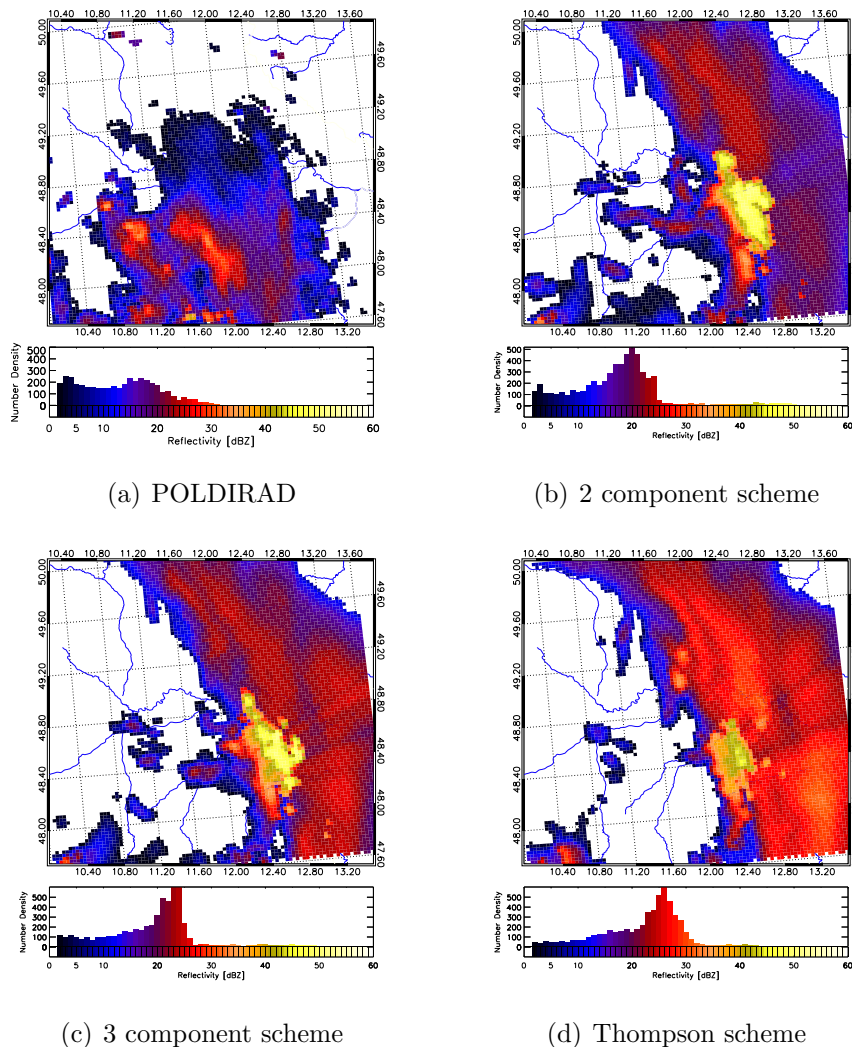


**Figure 5.8:** Observed and simulated 1° PPI scans of reflectivity [dBZ] at 10:00 UTC on July 5th, 2005. Shown are simulations from the LMK version 3.17 for the three different microphysical schemes.

pronounced that a more detailed analysis seems to be reasonable. The Thompson scheme produces extreme intensities in snow although it was shown earlier that this scheme simulates significantly smaller reflectivities for the same snow mixing ratio in comparison to the LMK schemes. Either the snow mixing ratios must be dramatically increased in comparison to the 3 component scheme or another denser ice hydrometeor type must be present increasing reflectivity because of higher dielectric effects. The corresponding hydrometeor classification in Figure 5.9 shows that the precipitation in the ice phase consists in the two model runs

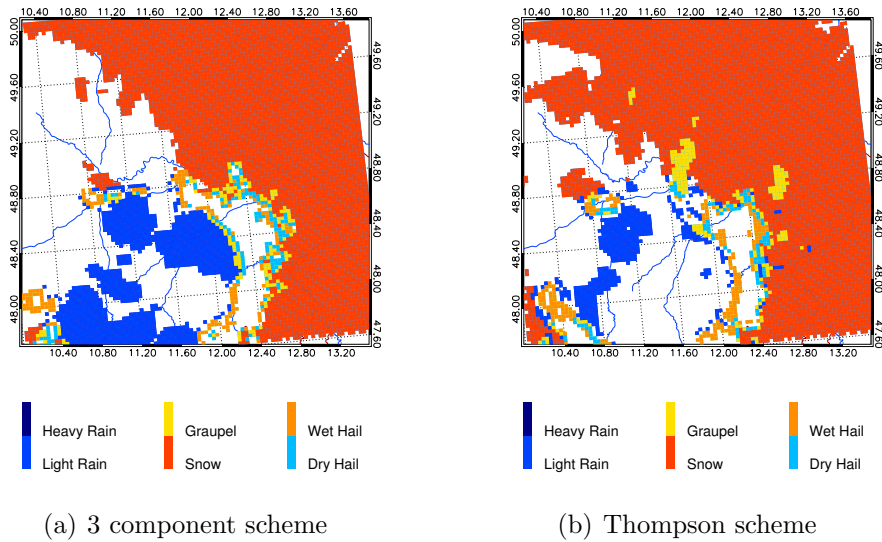


**Figure 5.9:** Hydrometeor classification for the  $1^\circ$  synthetic PPI scan at 10:00 UTC for the LMK 3.17 3 component scheme and the Thompson scheme.

mainly of snow and that the enhanced reflectivities can not be explained with the presence of graupel. Therefore, the extreme reflectivities must result from enhanced total precipitating

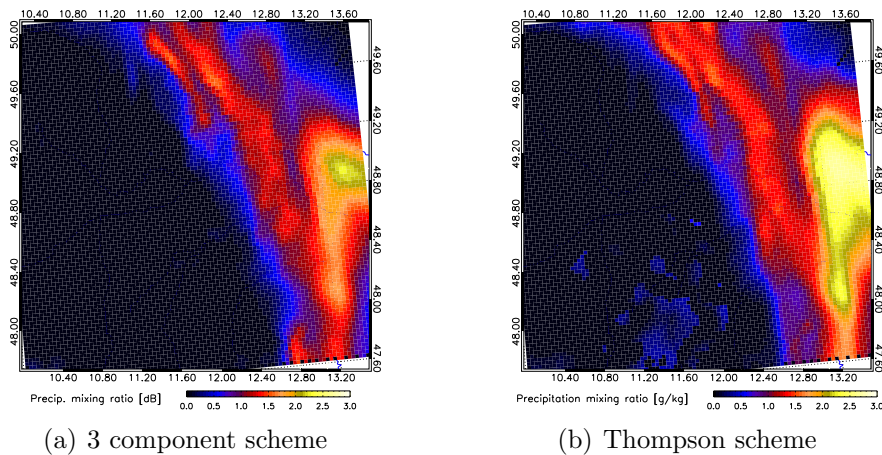


**Figure 5.10:** Precipitation mixing ratio [ $\text{gkg}^{-1}$ ] along the radar path of the 10 UTC  $1^\circ$  PPI scan for the LMK 3 component scheme and the Thompson scheme.

water contents. This is proved by the  $1^\circ$  PPI scan of precipitation mixing ratios in Figure 5.10 showing large discrepancies between the microphysical parameterization schemes which are especially pronounced in the ice phase.

The reason for the enhanced mixing ratios produced by the Thompson scheme must be in the source or sink terms of snow or in a combination of the two. Regarding the sink terms, sedimentation of snow can be inhibited by smaller terminal falling velocities or larger updrafts in the precipitation field. However, comparisons of the mean vertical velocities did not show large differences for the LMK and the Thompson scheme. Regarding the assumed

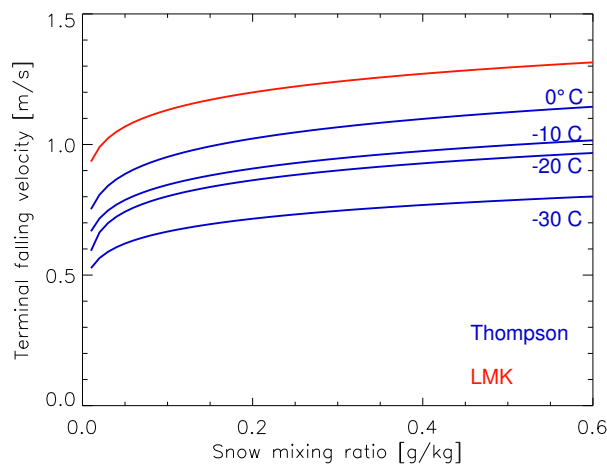


**Figure 5.11:** Comparison of terminal falling velocities of snow [ $\text{m s}^{-1}$ ] as a function of snow mixing ratio [ $\text{g kg}^{-1}$ ] for the LMK 3 component scheme and the Thompson scheme for selected temperatures [ $^{\circ}\text{C}$ ].

terminal falling velocity of the microphysical parameterization schemes, larger discrepancies appear. The terminal falling velocities for snow as derived from the LMK and the Thompson scheme are presented in Figure 5.11 as a function of snow mixing ratio. This is done for selected temperatures which impact on the terminal falling velocity of snow due to the temperature dependence of the PSD in the Thompson scheme. For all temperatures, the terminal falling velocities assumed by the Thompson scheme are significantly smaller than the ones considered in the LMK scheme and decreasing temperature also decreases this sedimentation speed. This means that the residence time of snow is larger in the Thompson scheme and, therefore, more snow particles can accumulate in the precipitation field before falling out.

Another possibility of increasing the snow water content could be in the source terms and, therefore, the autoconversion from cloud ice to snow. Figure 5.12 shows the cloud ice content for both microphysical schemes at model level 10 proving that in the Thompson scheme twice as much cloud ice exists as in the LMK scheme. This can be explained by the fact that in the LMK the threshold for autoconversion from cloud ice to snow is set to 0 (Keil et al. (2006)), therefore, depleting for every time step all the cloud ice moving it into the snow category. A further evaluation of the representation of cloud ice in NWP is not possible with a C band radar due to the large wavelength. However, the discussion showed that precipitation reaching the ground results from a number of microphysical processes in the atmosphere and that differences in the reflectivities in rain can be traced back to discrepancies in the description of cloud ice.

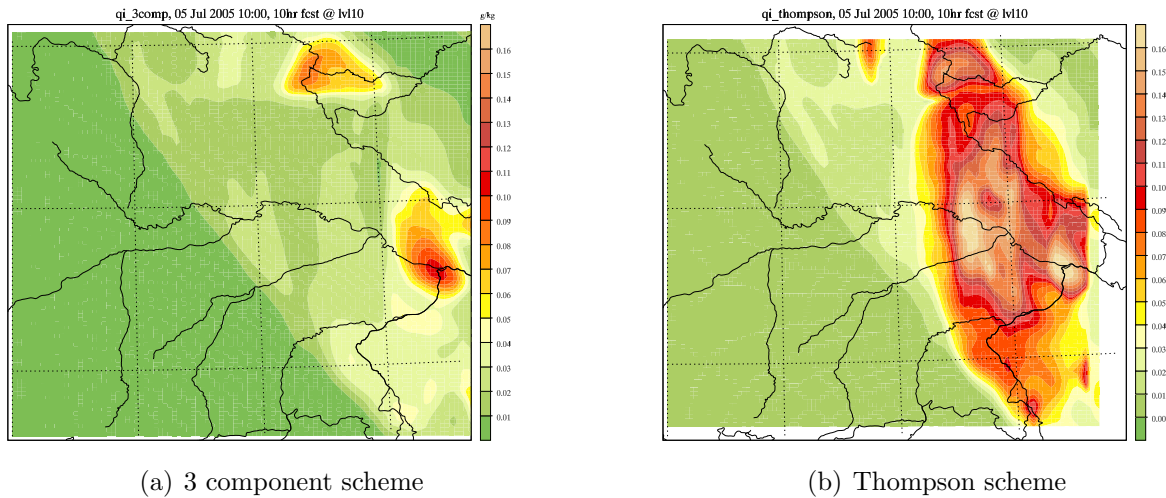


**Figure 5.12:** Cloud ice content [ $\text{g kg}^{-1}$ ] for the 3 component (left) and the Thompson scheme (right) at 10:00 UTC at a height of 300 hPa.

### 5.3 Vertical Profiles

The last section showed large discrepancies in the representation of intensity for the different microphysical parameterization schemes that were closely related to the assumptions regarding the DSD of rain and snow. In this section, the focus will be on the evaluation of the vertical distribution of reflectivity and polarimetric quantities with a special interest in the representation of the melting layer and the rain DSD in the NWP model. This will be done comparing vertical profiles derived from  $2^\circ$  PPI scans. As it was stated in the introduction to this chapter, stratiform precipitation is very homogeneous and, therefore, it is possible to average the observables over the azimuth angles and discuss the radar parameters as a function of range or height. The advantage of this method lies in the higher statistical significance due to the larger data set in contrast to evaluating a single RHI scan. To do so, PPI scans at  $2^\circ$  elevation were chosen because at these elevation angles the observations are not impacted by the ground clutter of the Alps which would be true for smaller elevations. The polarimetric observations started at 8:00 UTC, at a time when the simulations began to underestimate the intensities in rain while at earlier time steps the simulations overestimated the intensities. Therefore, the observations at 8:00 UTC will be compared to the simulations at 6:00 and 8:00 UTC to attain better correlations between simulated and observed polarimetric quantities.

Figure 5.13 shows the averages over the azimuth angles for reflectivity (first row),  $Z_{DR}$  (second row), and  $L_{DR}$  (third row) for the observations at 8:00 UTC and the simulations at 6:00 (left column) and 8:00 UTC (right column). The black graphs represent the measurements of four different Poldirad scans between 7:30 and 8:30 UTC. The small spread between these graphs proves the persistence and spatial homogeneity of the precipitation event at that time where the largest scatter is found in rain with reflectivities ranging from 25 to 30 dBZ. In the brightband, the intensities are increased reaching maximum values of 37 dBZ and intensity diminishes again with increasing height from 22 dBZ directly above the melting layer to 5 dBZ at about 4.8 km height. Regarding the polarimetric quantities, the scatter

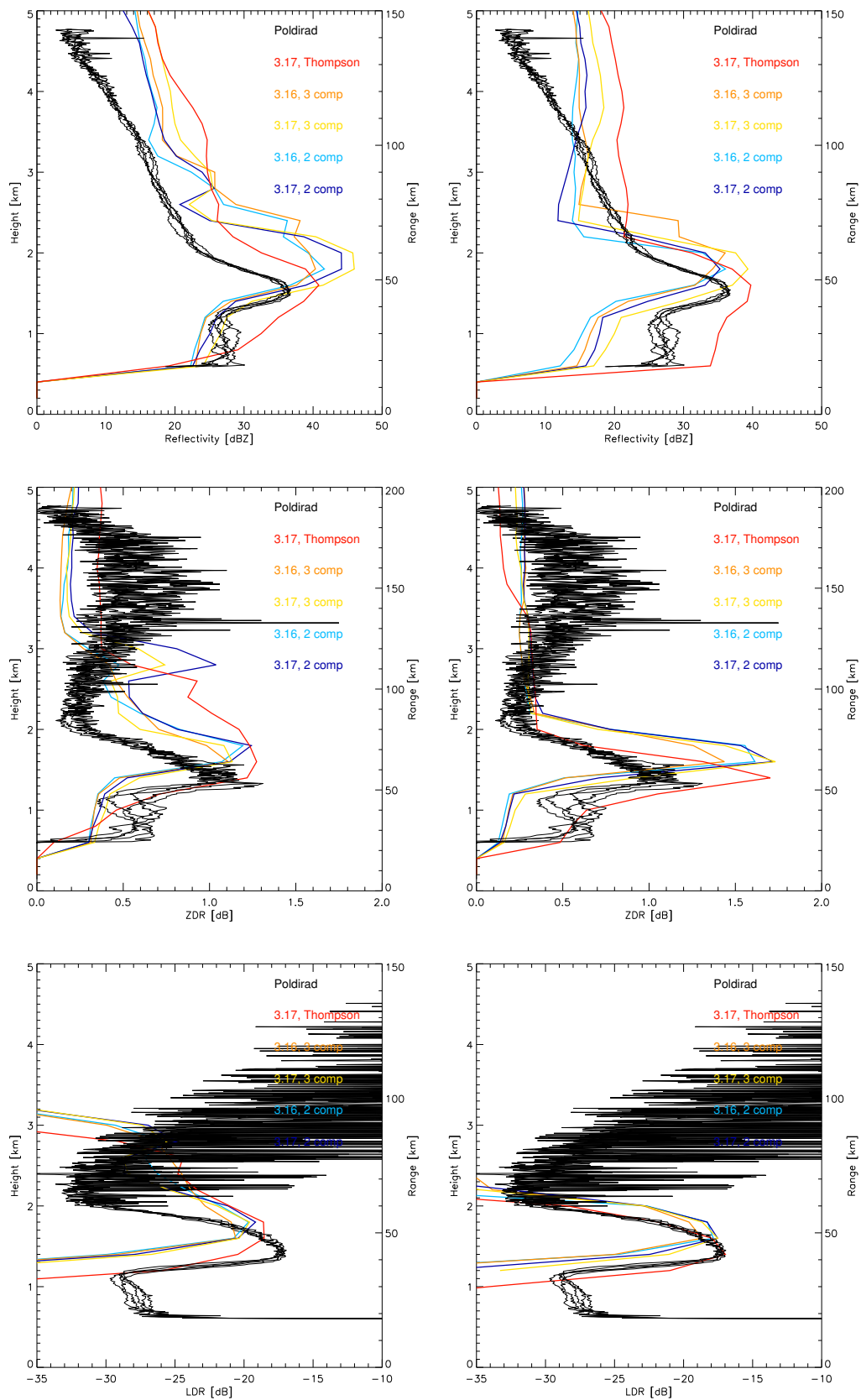


**Figure 5.13:** Mean over the azimuth angles of a  $2^\circ$  PPI scans. Shown are 4 different POLDIRAD scans between 7:30 and 8:30 UTC (black lines) and the LMK forecasts at 6:00 (left) and 8:00 UTC (right) for reflectivity [dBZ] (upper line),  $Z_{DR}$  [dB] (middle), and  $L_{DR}$  [dB] (bottom line).

is much larger than in the case of reflectivity and the observations are especially disturbed at heights above the melting layer. This shows that the assumption of homogeneity is not any more valid for the polarimetric quantities above the brightband and can be explained by the large attenuation in the melting layer related to the long paths of the radar beam at the small elevation angle. Therefore, the polarimetric observations above the melting layer should not be used for evaluation purposes. However, in the rain,  $Z_{DR}$  varies between 0.4 and 0.7 dB and increases in the brightband to a maximum value of 1.3 dB while observable values of  $L_{DR}$  only exist in the brightband reaching maximum values of  $-17$  dB.

For the simulations applies that for all model runs the precipitation extends to higher altitudes than in the observations explaining once again the increased numbers of pixels for the lower reflectivity classes in the time series of histograms. Furthermore, the height of the  $0^\circ$  C isotherm is overestimated and, therefore, the brightband appears at higher altitudes in the averages especially visible in the polarimetric quantities. Although the brightband is overpredicted,  $L_{DR}$  ranges in the order of  $-20$  to  $-17$  dB and reproduces very well the observations. This proves that the assumptions regarding the representation of brightband signatures in SynPolRad with the goal to attain typical values of  $L_{DR}$  are correct and that the dielectric constant is well predicted. The resulting overestimation of reflectivity in the case of the LMK scheme is due to a wrong representation of the PSD of melting snow which produces too many large particles contributing massively to reflectivity in the moment of melting.

For the LMK 2 and 3 component scheme, the best resemblance to the observations is given at 6:00 UTC reproducing well the slope of the observed graphs although the height of the melting layer is overpredicted. This is also true for the reflectivities in the snow and the brightband reaching maximum values of  $40 - 46$  dBZ while the intensities in rain are slightly underestimated with values from  $20 - 27$  dBZ in comparison to the observed  $25 - 30$  dBZ. The highest values in rain are simulated by the LMK 3.17 version with the 3 component scheme with synthetic reflectivities from  $21 - 27$  dBZ. For all model configurations holds further that  $Z_{DR}$  is clearly underestimated with values from  $0.3 - 0.5$  dB. In the following hours, reflectivity decreases steadily for the LMK schemes and the later time steps do not bring new insights in the microphysical parameterizations. In the simulations considering the Thompson scheme at 6:00 UTC, the precipitation field doesn't cover the whole domain resulting in an underestimation of the intensities in rain. At later time steps, this changes rapidly. While producing at 8:00 UTC similar reflectivities in snow and in the brightband as observed, the reflectivities in rain are strongly overpredicted with values from  $28 - 36$  dBZ in comparison to  $25 - 30$  dBZ in the observations resulting in almost no visible transition between the rain and the brightband. However, looking at the simulated values of  $Z_{DR}$  in the rain, the simulations considering the Thompson scheme fit the observations best.

Comparing the results of all model simulations, the combined information content of reflectivity and  $Z_{DR}$  shows that for all microphysical schemes the representation of the rain DSD is not correct in the sense that the slope of the DSD is too steep. In the case of the LMK schemes, the LMK version 3.17 together with the 3 component microphysical scheme reproduces reflectivities in the same order as the observations but  $Z_{DR}$  is clearly underestimated. Therefore, the simulated DSD has not enough large drops for the given reflectivity and the observed rain DSD has a smaller slope than the one assumed by Marshall and Palmer (1948). The Thompson scheme reproduces  $Z_{DR}$  but strongly overestimates reflectivity proving that the number of large drops is comparable to the observations while the total number of drops

is strongly overestimated. In this case the differences between the LMK and the Thompson schemes can result from the different formulations of rain DSD, as reflectivity is under the threshold of 36 dBZ seen in Figure 5.4. This results in an enhanced intercept parameter  $N_0$ , increasing the number of small drops as well as the slope of the DSD by several orders of magnitude.

## 5.4 Discussion

The evaluation of the stratiform case study showed that the LMK is in general able to reproduce the stratiform precipitation event, however, with strong discrepancies in the representation and spatial distribution of intensities. The general life cycle of the precipitation event is well represented with the decay of the system in the early afternoon while in the early morning the intensities were strongly overestimated. All model configurations pro-

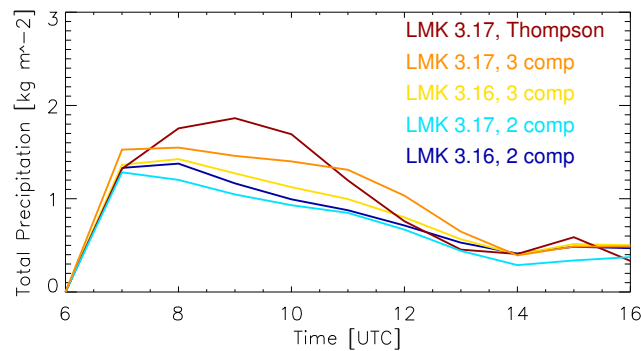


**Figure 5.14:** Times series of hourly accumulated total precipitation [ $\text{kg m}^{-2}$ ] averaged over the model domain for all LMK configurations.

duced, furthermore, an overestimation of the vertical extent of the precipitation and the height of the  $0^\circ$  isotherm. The differences between the model versions 3.16 and 3.17 were small without systematic biases for all model combinations. In general, the LMK schemes tend to underestimate reflectivity in the snow and rain while strongly overpredicting the brightband whereas the Thompson scheme produces enhanced intensities in rain and snow and represents well the brightband signatures. In order to show that the different microphysical parameterization schemes affect QPF, the total precipitation at the ground accumulated over one hour and averaged over the model domain is shown in Figure 5.14. During the morning, the microphysical parameterization schemes clearly produce different precipitation amounts with the Thompson scheme simulating the highest and the 2 component scheme simulating the lowest values.

The large differences between the microphysical parameterization schemes and the observations are striking as they already appear in a stratiform case study where only rain and snow exist as precipitating hydrometeors and the microphysical processes involved in the formation of precipitation are relatively simple. Regarding the individual microphysical parameterization schemes, the differences between the LMK 2 and 3 component scheme remained small as expected while larger discrepancies were found in comparison to the Thompson scheme.

These discrepancies already appeared in the time series of histograms of reflectivity and were related to the different assumptions regarding the formulation of the snow and rain DSD. Major variations were found in the formulation of the DSD of rain and snow regarding the intercept parameter  $N_o$ . The Thompson scheme adapts  $N_o$  to the meteorological situation defining the intercept parameter of snow as a function of temperature and the intercept parameter of rain as a function of rain rate. In case of rain, this results for smaller rain rates in a steeper DSD and, therefore, smaller values of reflectivity and  $Z_{DR}$  are produced as compared to the LMK scheme for the same rain mixing ratio. For larger rain rates the formulation of DSD are the same for both schemes. The combined information content of reflectivity and  $Z_{DR}$  showed that for the given case study for all microphysical schemes, this representation of the rain DSD is not correct in the sense that the slope of the DSD is too steep.

Furthermore, in the Thompson scheme the intercept parameter of snow is defined as a function of temperature with  $N_o$  and  $\lambda$  decreasing for increasing temperature. Thus, for all temperatures smaller than 0° C, the Thompson scheme produces a much steeper PSD of snow than the LMK schemes. This decreases the number of large particles strongly contributing to reflectivity which also explains why the intensities of reflectivity within the melting layer are more realistic in the Thompson scheme although the snow mixing ratios are increased in comparison to the LMK schemes. Furthermore, for all temperatures the terminal falling velocities assumed by the Thompson scheme are significantly smaller than the ones considered in the LMK scheme and decreasing temperature also decreases this sedimentation speed. This means that the residence time of snow is larger in the Thompson scheme and, therefore, more snow particles can accumulate in the precipitation field before falling out. The explanation for the smaller cloud ice contents in the LMK could be in the threshold for autoconversion processes from cloud ice to snow which is set to 0, therefore, depleting for every time step all the cloud ice moving it into the snow category. Due to the different assumptions regarding the representation of microphysics, the Thompson scheme produces significantly higher mixing ratios of rain, snow, and cloud ice as compared to the LMK scheme. This shows that the strong overprediction of reflectivities in rain by the Thompson scheme is due to strongly overpredicted rain rates originating from enhanced snow and cloud ice contents.

Regarding the simulations of the brightband signatures,  $L_{DR}$  was reproduced for all microphysical schemes in the right order. This proves that the assumptions in the calculations of the dielectric constant and the changes in the assumptions regarding the falling behaviour of melting snow are reasonable. The resulting overestimation of reflectivity in the case of the LMK scheme is due to a wrong representation of the PSD of melting snow which produces too many large particles contributing massively to reflectivity at the moment of melting.

Concluding, most of the discrepancies shown in this section originated from the assumptions regarding the representation of the ice phase in the NWP models. Furthermore, the impact of the ice phase on the precipitation at the ground has been discussed. However, only evaluating one stratiform case study, no key parameters for a wrong representation of intensities could be identified. Therefore, these results should not be generalized before the results are also confirmed for a longterm evaluation. Furthermore, the total precipitation at the ground needs to be evaluated against rain gauge observations.

# Chapter 6

## Convective Case Study – 12 August 2004

The last chapter focused on a stratiform case study where the dynamics and related microphysical processes were relatively simple. In contrast, convection is characterized by high vertical velocities in the order of  $1 - 10 \text{ m s}^{-1}$  resulting from the differences in buoyancy in an unstable atmosphere and leading to a larger vertical extent of the cloud and an enhanced condensation and precipitation of water. Due to the high vertical velocities in the convective cores, air parcels are rapidly lifted and cooled, and as a consequence large liquid water contents evolve allowing the formation of heavier ice species like graupel or hail through riming. Downdrafts develop because of falling hydrometeors dragging air downward and can be enhanced and maintained due to the removal of latent heat by melting ice hydrometeors or evaporation. Therefore, the presence of graupel and hail is of high importance impacting the strength and life cycle of the system by redistributing latent heat and feeding energy back to the heat engine of the storm. The different dynamical characteristics of stratiform and convective precipitation result in a sharp distinction in the microphysics but also in the spatial distribution of precipitation. Convection is a more local phenomena related to an unstable atmosphere. Single cells can evolve from heating and grow to larger systems, or organized systems can evolve due to external forcing as orography or large scale dynamics. Accordingly, the spectrum of convective clouds ranges from fair weather cumuli, individual thunderstorms, to complexes of mesoscale convective systems.

The new generation of mesoscale NWP models has been developed to explicitly resolve convection. In order to achieve this goal, the horizontal resolution of the German model LM has been refined from 7 km to 2.8 km and the convection parameterization scheme is not used any more. Furthermore, graupel as an additional precipitating ice species to snow is considered in the LMK 3 component scheme. The extent to which the improvements of the LMK are sufficient to reproduce a convective event will be tested for a case study with organized convection over southern Bavaria on August 12th, 2004 related to a cold front crossing Germany. Due to the external forcing by the cold front, the predictability of the system is increased and the model is expected to reproduce the event. The focus of this study will be on the representation of the life cycle, timing, location, and strength of the system. Especially important will be the evaluation of the different microphysical parameterization schemes where large differences are expected because of the different number and

assumptions regarding the precipitating ice hydrometeors. To increase the outcome of this study, the LMK simulations will be compared to results from the French research model MesoNH. MesoNH considers additionally to rain, snow, and graupel also a hail class. Hail is of utmost importance to the dynamics of a thunderstorm because of its role in triggering the development of downdrafts and the effective redistribution of latent heat. Therefore, a comparison of the MesoNH simulations to the LMK results will show if the consideration of hail as an additional and denser ice hydrometeor type improves the representation of convective precipitation in mesoscale NWP models further.

## 6.1 Synoptic Overview, Observations, and Model Configuration

On August 12th, 2004 a cold front crossed Germany enforcing the development of severe thunderstorms with high intensities in southern Bavaria. The synoptic scale circulation was characterized by a south-westerly flow at upper levels and easterly winds near the surface. Thunderstorm cells developed near the Lake of Constance and propagated eastward from 15:00 to 23:00 UTC. The front developed into a squall line with  $20 \text{ m s}^{-1}$  wind gusts and a sharply defined convective line producing hail and a trailing region of stratiform precipitation. Figure 6.1 shows the precipitation over Germany as observed by the German Radar composite at 18:00 UTC.

The observations with the polarimetric Doppler radar POLDIRAD started at 12:04 UTC

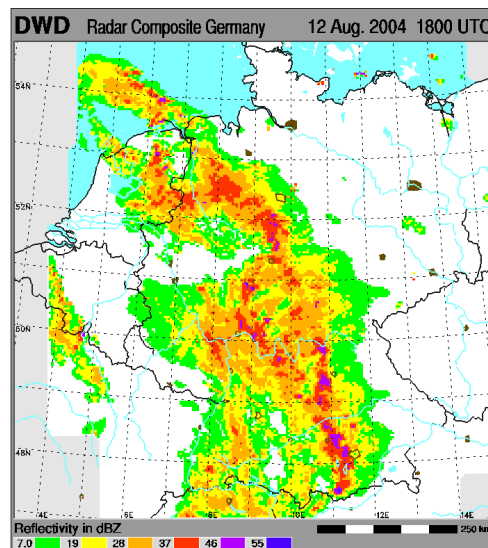


**Figure 6.1:** The squall line on August 12th, 2004 shown in reflectivities [dBZ] as observed by the German radar composite at 18:00 UTC.

with  $1^\circ$  PPI scans. First convection was observed at 15:30 UTC and in the following a number of PPI, RHI, and volume scans were executed. The intensive observation period stopped at 20:37 UTC when the system had already decayed.

For the convective case study, hourly output fields of the operational LM configuration driven

with fields of the global model GME served as input for the high resolution experiment with the LMK. As in the stratiform case, the domain encompassed 100 x 100 x 40 grid points centered over Munich airport. The LMK was run with two different versions: The version LMK 3.16 was run with the 2 component, the 3 component, and the Thompson scheme while the LMK 3.18 was only run with the 2 and the 3 component scheme as the Thompson scheme was not yet available from DWD. The differences in the LMK schemes 3.16 and 3.18 result from changes in the formulation of physics-dynamics interaction as well as the incorporation of a shallow convection scheme in the 3.18 model version. Furthermore, two runs of the French research model MesoNH with one parameterization scheme including snow and graupel, and another one also considering hail as precipitating ice categories will be evaluated.

## 6.2 Evaluation of the Life Cycle and Intensity

Similarly to the stratiform case study, the representation of the life cycle will be examined focusing on the timing, position, and strength of the storm. As the convection evolved in association with a cold front, the model is supposed to well predict the timing and the position of the squall line. Major differences are expected for the representation of the event for the various model configurations depending on the microphysical scheme and the related number and representation of ice hydrometeors. The evaluation will be based on POLDIRAD 1° PPI scans compared hourly to LMK simulations starting at 17:00 UTC when the line of convection entered the LMK domain until 20:00 UTC when the convective system had almost totally decayed.

Figure 6.2 shows the observed and simulated 1° PPI scans at 17:00 UTC on August 12th, 2004. In the observations, the event enters the domain organized in a line of convection from the west. The line is oriented perpendicular to the direction of propagation and extends from the Alps to the Danube with the strongest reflectivities in the south reaching values of 48 dBZ. Towards the north, the intensities weaken and especially north of the Danube only some single convective cells show enhanced reflectivities. The LMK produces convection at 17:00 UTC and for all model configurations the system has already propagated too far east in comparison to the observation. The intensities of the simulated and observed systems are comparable apart from the fact that the simulated storms cover a smaller area than observed. Furthermore, the number of pixels with smaller reflectivities is clearly underestimated for all model configurations. There are some differences between the LMK 3.16 and the LMK 3.18 model version regarding the organization of the systems. The 3.18 version produces a cluster of convection north of the Danube with two centers of convective cells but the nature of the line of convection triggered by the cold front is at that time step not represented in the model. In the 3.16 model version, the linear structure is better represented but not as clearly as observed. Comparing the different microphysical schemes the differences remain small for the respective model versions. Only the Thompson scheme produces even less pixels with low reflectivities in comparison to the other simulations.

At 18 UTC (Figure 6.3), the system has propagated east and compared to the 17:00 UTC

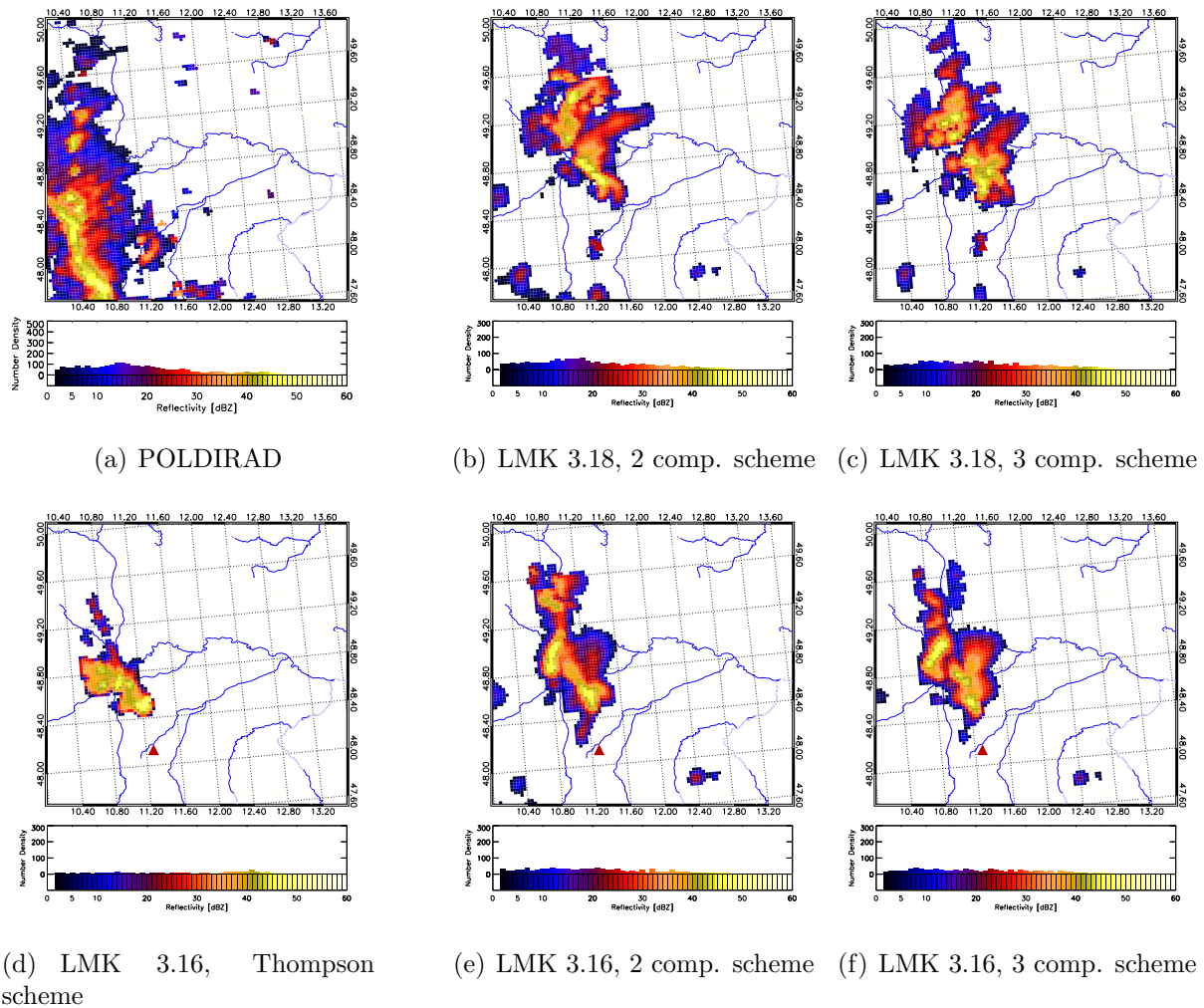


**Figure 6.2:** Observed and simulated  $1^\circ$  PPI scans of reflectivity [dBZ] at 17:00 UTC on August 12th, 2004 for five different configurations of the LMK. The position of POLDIRAD is shown by the triangle.

observations, the line of highest reflectivities has weakened slightly with the maximum intensities now reaching 43 dBZ. While the squall line has decayed in intensity, the total precipitation has spread out over a larger area. In the simulations, the system has also propagated east but slower than in the observations decreasing the spatial differences between the observed and modeled line. However, in contrast to the observations where the system is already decaying in the model the storm has strongly intensified with reflectivities reaching values of 50 dBZ. The differences between the two LMK model versions remain relatively small although at this time step the LMK 3.18 version reproduces better the linear organization of the squall line. Regarding the microphysical schemes, the LMK 2 component scheme produces higher reflectivities in the convective cells for the two model versions in comparison to the 3 component scheme. The Thompson scheme simulates a substantially smaller storm compared to the other microphysical schemes overestimating the higher and underestimating the lower reflectivities while it totally misses the southern part of the convective system.

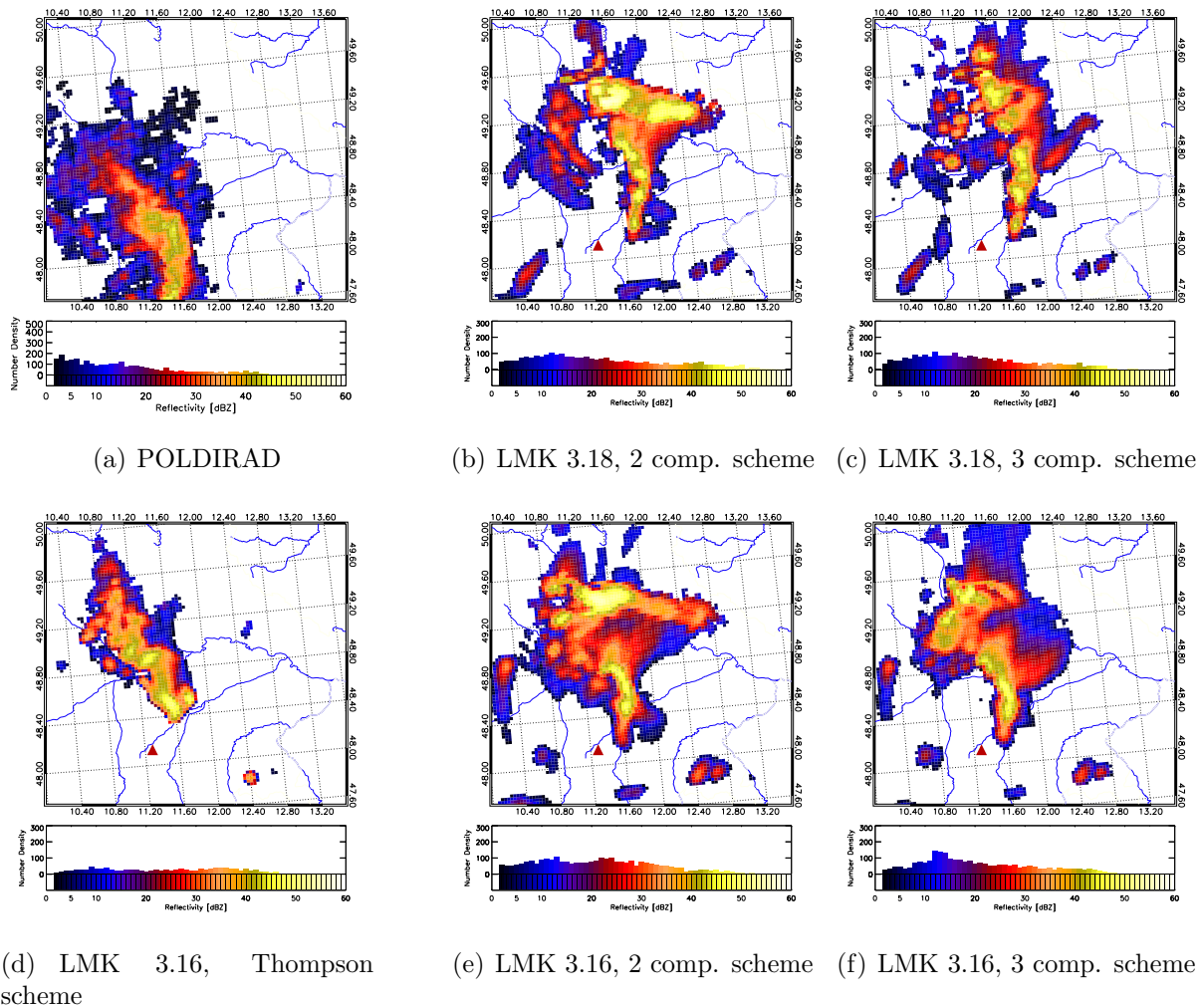


**Figure 6.3:** Observed and simulated  $1^\circ$  PPI scans of reflectivity [dBZ] at 18:00 UTC on August 12th, 2004 for five different configurations of the LMK.

At 19:00 UTC (Figure 6.4), the system has passed Munich and the intensity has decayed further with only some convective cells exceeding reflectivities of 40 dBZ. Behind the line of convection a large area of stratiform precipitation has developed spread over almost the whole domain with reflectivities in the range of 5 – 25 dBZ. In the simulations, the system has also grown covering a larger area with precipitation. In the LMK 3.18 runs, the line of convection is still visible east of Munich but with reflectivities exceeding the observations. Behind the line of convection, smaller convective cells developed with reflectivities between 5 and 39 dBZ. In the LMK 3.16 runs, the linear structure is only found in the model runs including the Thompson scheme which strongly overestimates reflectivity with values up to 50 dBZ while once again the lower reflectivities are almost not present in the simulations.

At 20:00 UTC, the convective system has totally decayed in the observations (Figure 6.5). The line of convection has moved to the east of the domain with maximum reflectivities of 35 dBZ and a second band of enhanced reflectivities developed behind the first one with si-

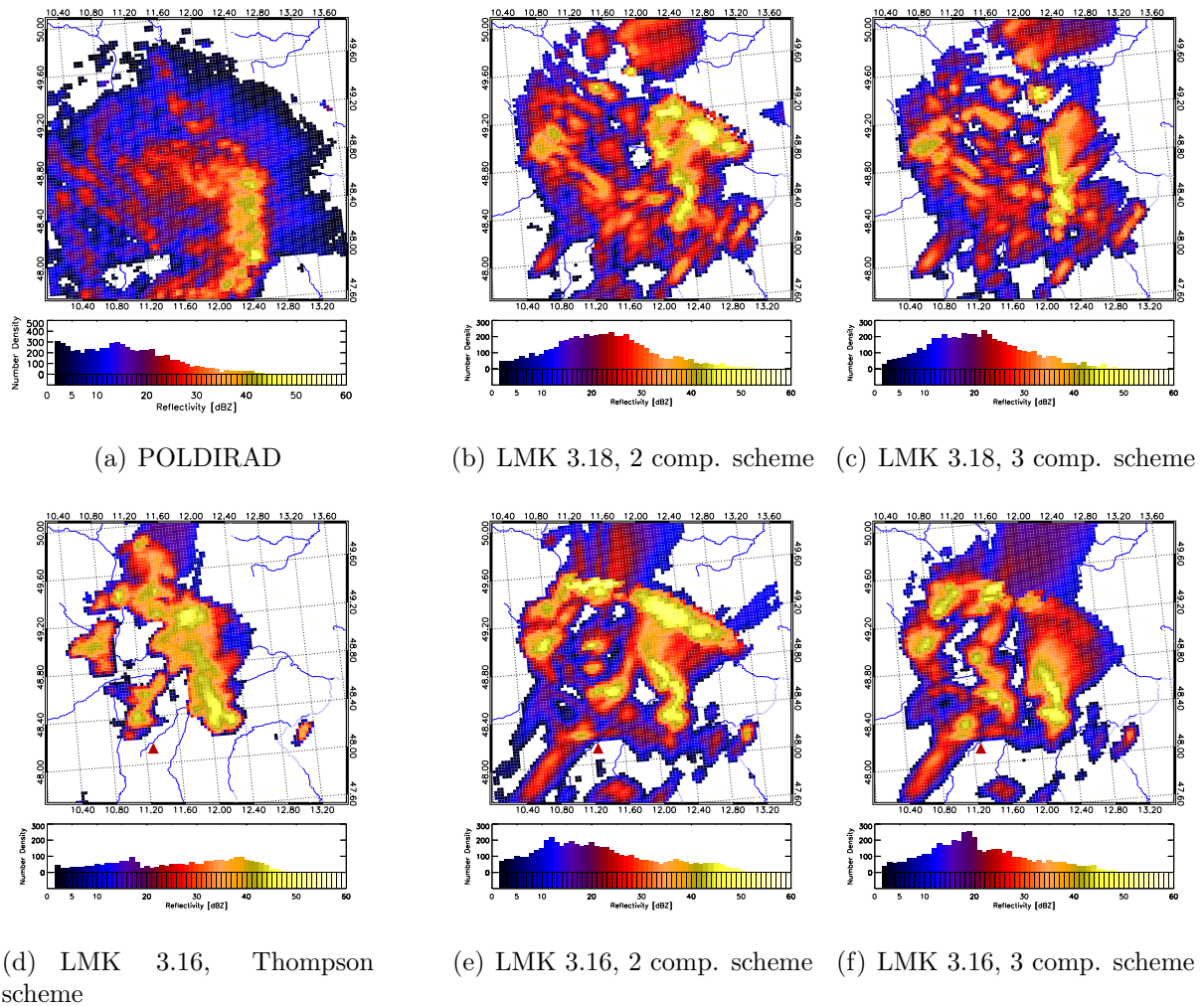


**Figure 6.4:** Observed and simulated  $1^\circ$  PPI scans of reflectivity [dBZ] at 19:00 UTC on August 12th, 2004 for five different configurations of the LMK.

milar reflectivities. The precipitation is spread out over the whole domain with reflectivities in the range of 5 – 30 dBZ. In the simulations, the system is still active and the reflectivities are overestimated for all model runs. In the LMK 3.18 simulations, the reflectivities in the convective cells are increased compared to the 19:00 UTC runs. In the LMK 3.16 model version, the reflectivities are weaker in comparison to the previous run but, nevertheless, the LMK 3.16 version produces higher reflectivities compared to the 3.18 version. Comparing the microphysical schemes, the 2 component scheme produces for both model versions higher reflectivities than the 3 component scheme. The Thompson scheme simulates once again a spatially smaller convective event with higher reflectivities.

In order to compare the life cycle of the storm in the observations and the model runs in a more quantitative way, the temporal evolution of the system is shown in Figure 6.6 as a time series of histograms for the classes of reflectivity from 15 – 25, 25 – 35, 35 – 45, and 45 – 55 dBZ. In the observations, the system developed until 16:30 UTC where the maximum

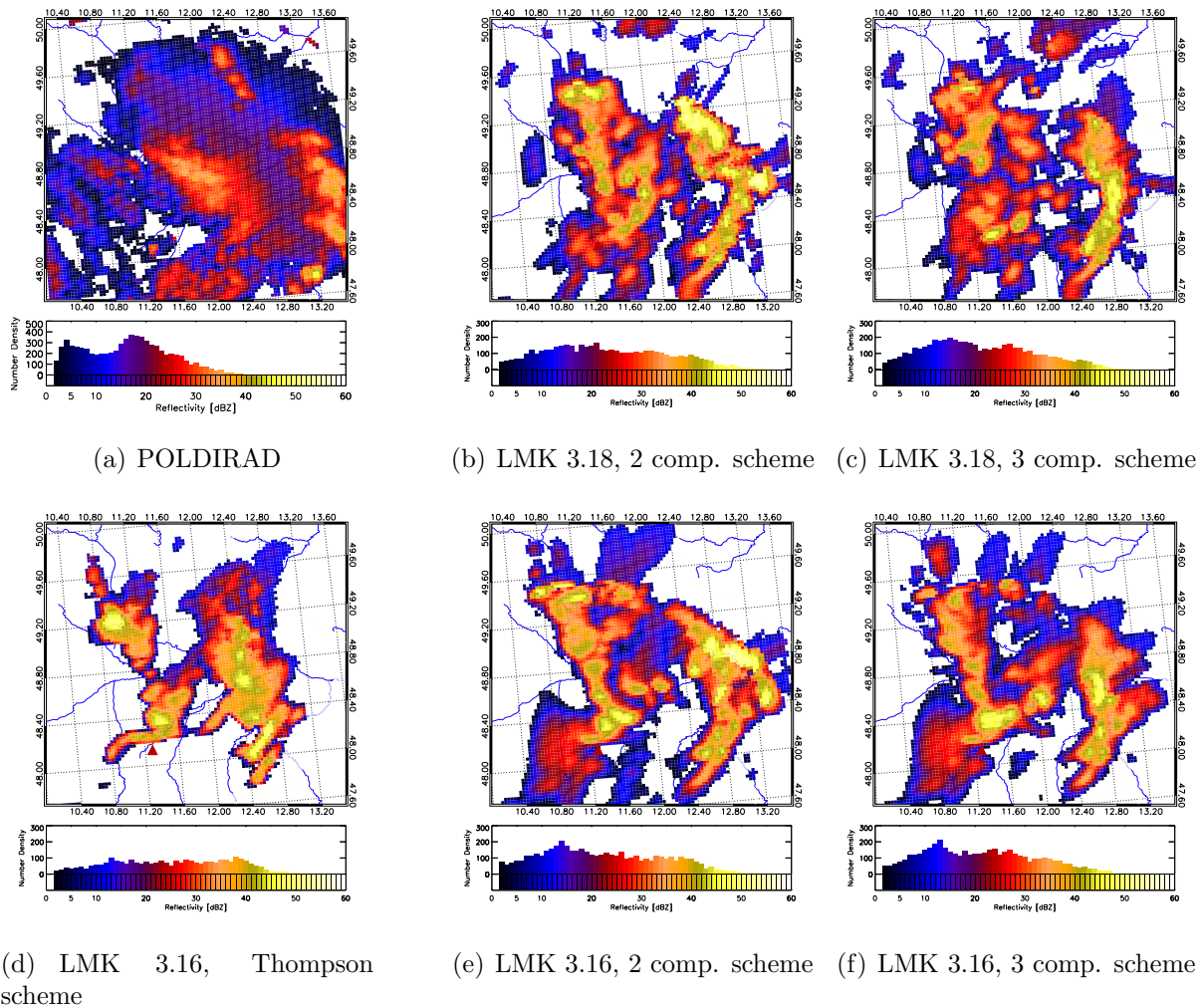


**Figure 6.5:** Observed and simulated  $1^\circ$  PPI scans of reflectivity [dBZ] at 20:00 UTC on August 12th, 2004 for five different configurations of the LMK.

number of pixels in the reflectivity class of 45 – 55 dBZ is reached. These high reflectivities are a strong evidence for the presence of hail in the storm. At that time, the simulated systems are still too small and too weak resulting in an underestimation of the number of pixels in all reflectivity classes and for all model configurations. In the reflectivity class from 35 – 45 dBZ, the observed number of pixels increases until 18:30 UTC while in the model, the evolution of the system lags behind the observations until 17:30 UTC when for the first time comparable numbers of pixels in all classes of reflectivity are obtained. In the model, however, the system develops further until 20:00 UTC while at this time the observed system has almost completely decayed. The simulated number of pixels for the lowest reflectivity class is clearly underestimated showing that the transition from the squall line to the wide spread stratiform precipitation is not captured by the model. The best agreement between observations and simulations is found in the reflectivity class 25 – 35 dBZ for all model configurations.

For the lower reflectivity classes, the differences between the model versions of the LMK are more important than the differences between the LMK microphysical schemes with the LMK

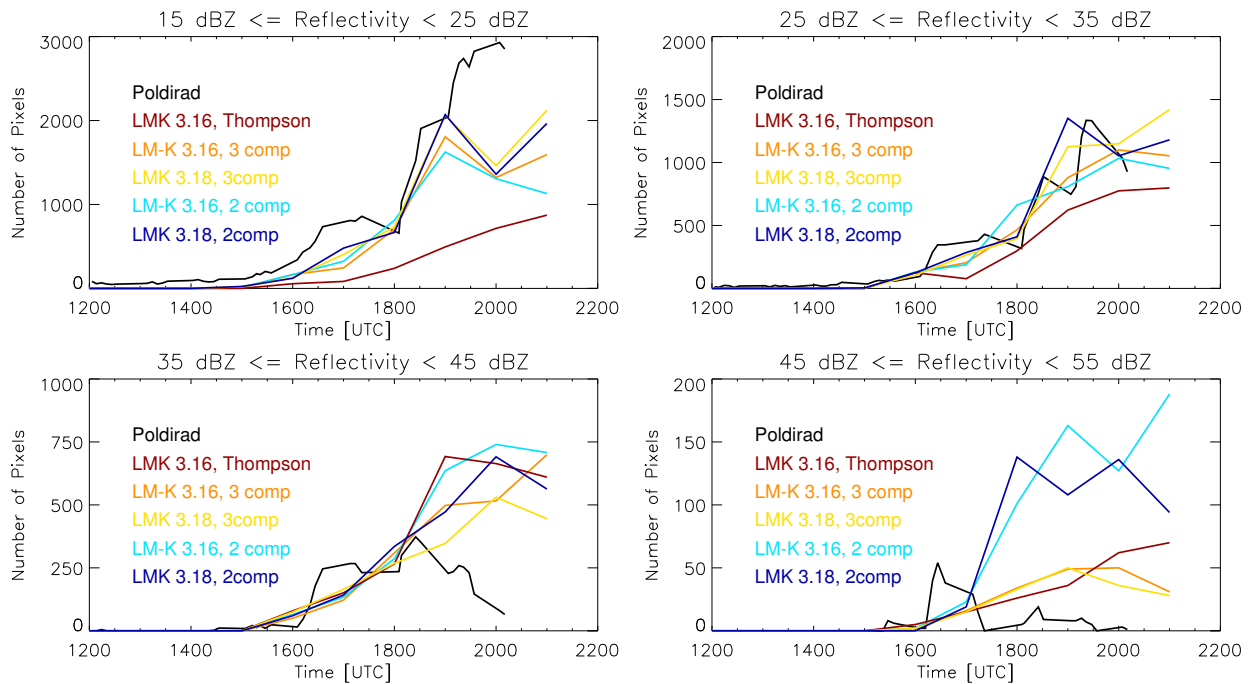


**Figure 6.6:** Time series of histograms derived from observed and simulated  $1^\circ$  PPI scans for different classes of reflectivity [dBZ]. The POLDIRAD observations are given in black while the model runs are plotted in colour.

3.18 producing from 18:00 UTC more pixels in this reflectivity class independently which microphysical scheme is used and, therefore, better reproducing the observations. For the high reflectivity classes, the differences between the LMK versions are less important compared to the differences in microphysical schemes where the 2 component schemes simulates substantially more pixels than the 3 component scheme and, therefore, strongly overestimates these high reflectivities. The Thompson scheme behaves differently producing substantially fewer pixels for the low reflectivity classes and overestimating the number of pixels for the high reflectivity classes.

Concluding, the LMK is generally able to reproduce a comparable convective event but with difficulties in the position, organization, and timing. While the observations show a clearly defined squall line with trailing precipitation, the LMK forecasts tend to produce a more cellular structure without a spatial organization of cells. Until 18:00 UTC, the development of the system is underestimated by the model and in the following the simulated system increases in intensity and spatial extent until 20:00 UTC. Therefore, neither the observed decay nor the transformation to the stratiform precipitation event are captured by the model. The differences between the LMK versions remain relatively small in comparison to the differences between the microphysical schemes where the higher reflectivities are clearly overpredicted by the 2 component and the Thompson scheme. Furthermore, the strong underestimation of low reflectivities by the Thompson scheme is striking. In order to understand these differences between the microphysical parameterization schemes better, vertical profiles of the polarimetric quantities and the classification will be discussed in the next

section.

### 6.3 Volume Scans and Vertical Profiles

As it was stated in the introduction, presence and vertical distribution of the ice hydrometeors are especially important for a correct reproduction of the strength and life cycle of a convective event. Therefore, the spatial distribution of the observed and synthetic polarimetric quantities as well as the hydrometeor types will be studied for volume scans and vertical cross sections. Because in the case of convection, horizontal homogeneity can not be assumed as it has been done in the stratiform case, another method has been applied in order to derive the vertical profiles of the radar quantities using a POLDIRAD volume scan. The volume was scanned at 10 different elevation angles ranging from  $1 - 20^\circ$  and the same number of PPI scans was executed at the same elevations for the synthetic radar data. Then, in contrast to the stratiform case study, reflectivity was not averaged but the number of pixels within predefined reflectivity classes was counted and plotted as a function

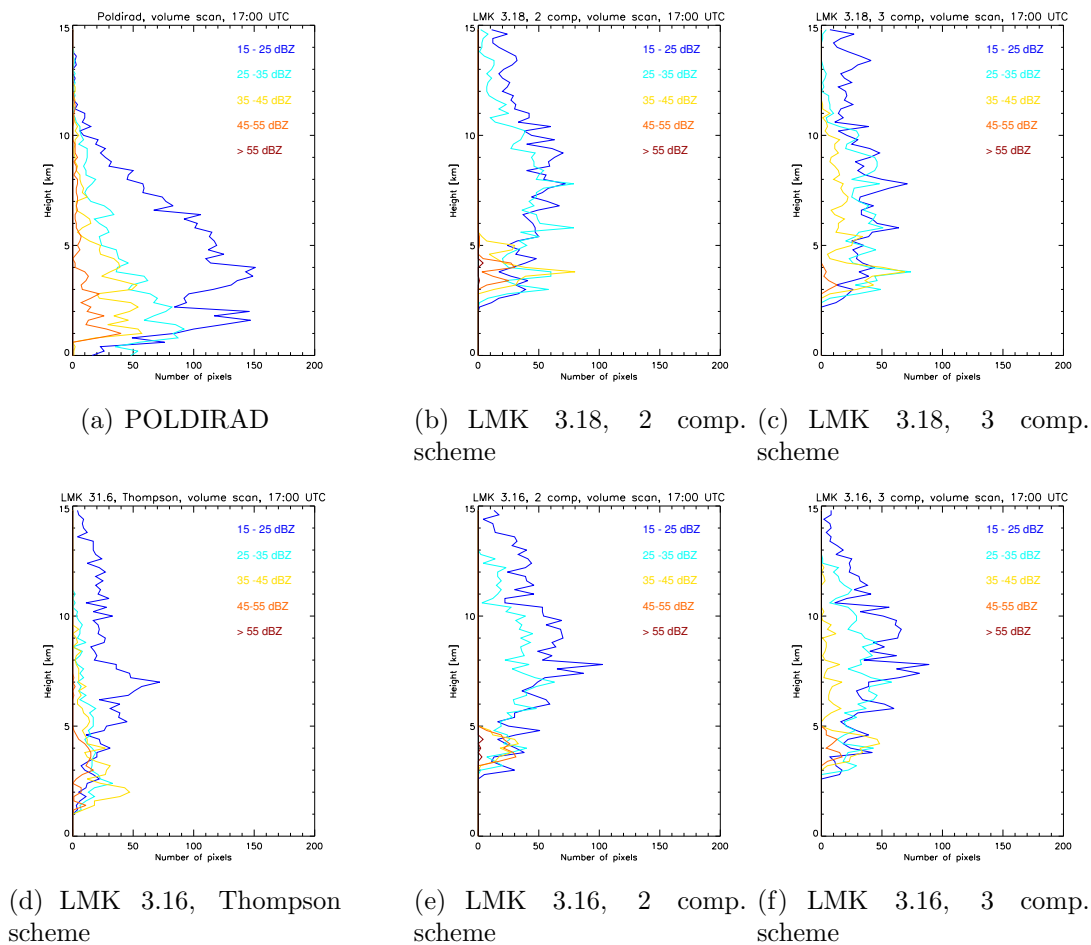


**Figure 6.7:** Observed and simulated histograms of classes of reflectivity [dBZ] as a function of height for a volume scan at 17:00 UTC encompassing 10 elevation angles from  $1 - 20^\circ$ .

of height.

Figure 6.7 shows the vertical distribution of the number of pixels within different classes of reflectivity for the observed and simulated volume scans. In the observations, the highest numbers of pixels are reached for the lowest reflectivities classes and the amount of pixels diminishes almost steadily with increasing reflectivity. The shape of the vertical distribution for a given reflectivity class nearly looks the same for all reflectivities resembling a Christmas tree with a maximum number of pixels near the ground and a decreasing number of pixels with altitude. This is also true for the very high reflectivities from 35 - 55 dBZ related to graupel and hail signatures that are present within the whole vertical extent of the cloud until the lowest observed altitudes. Comparing the observations to the model results the picture looks quite different especially regarding the vertical extent of the signatures. At lower heights, there are no reflectivities for the model runs because in the simulations the system is located at a larger distance from the radar and, therefore, no signals near the ground are available due to the curvature of the earth. On the other hand, in all model runs reflectivity and, thus, precipitation extends to higher altitudes although the synthetic volume scans were executed for the same elevation angles. Furthermore, the modeled systems are smaller in size which can be seen in the total number of pixels in comparison to the observations.

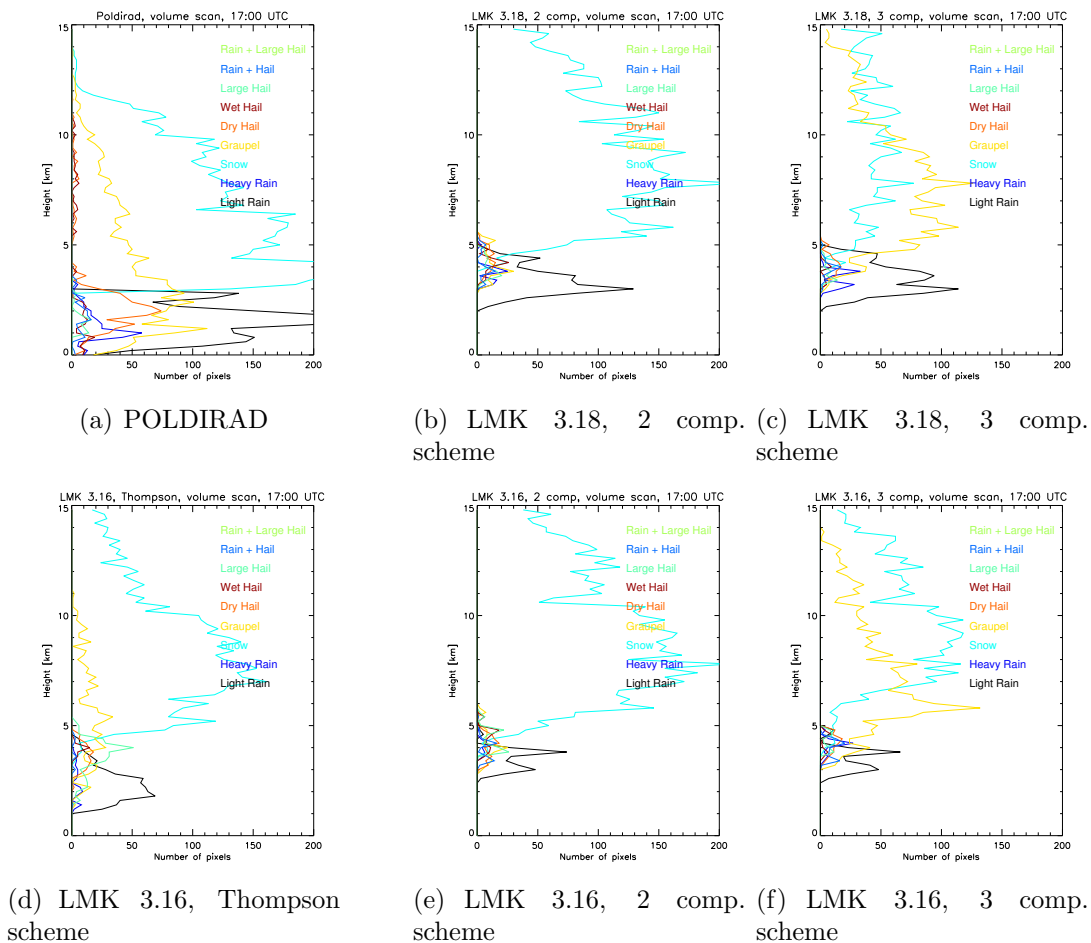


**Figure 6.8:** Observed and simulated histograms of hydrometeor classification as a function of height for a volume scan at 17:00 UTC encompassing 10 elevations from 1 – 20°.

There are substantial differences in the vertical distribution of reflectivities for the microphysical parameterization schemes. The 2 component scheme only considering snow in the ice phase is not able to reproduce reflectivities higher than 35 dBZ above the melting layer. The 3 component and the Thompson scheme also considering a graupel hydrometeor type produce at least a small number of pixels in the reflectivity class from 35 – 45 dBZ. This absolutely contrasts the observations where a decent number of pixels exists in the reflectivity class from 45 – 55 dBZ over a large vertical range. For all model configurations, a well defined brightband signature appears at a height of 5 km with reflectivities exceeding 55 dBZ for the 2 component scheme which is not observed in the POLDIRAD scan. Moreover, in the models, the total number of pixels in a respective class is almost comparable to the other classes of reflectivities showing that the decrease of the number of pixels with increasing reflectivity is not reproduced. The Thompson scheme looks a little different with a larger difference between the reflectivity class from 25 – 35 dBZ and the smaller reflectivity classes and thus reproduces better the observations than the LMK schemes. The vertical extent of the precipitation and related reflectivities for the Thompson scheme is much smaller as for the LMK schemes explaining the underestimation of the total number of pixels within the smaller reflectivity classes in the histograms discussed in the last section. This means that the total number of pixels within the lower reflectivity classes is better represented in the LMK microphysical schemes due to an overestimation of the vertical extent of the precipitation. However, the vertical distribution of these low reflectivities is better reproduced by the Thompson scheme. Furthermore, for all microphysical schemes the number of pixels in the lower reflectivity classes at lower altitudes is strongly underestimated.

Figure 6.8 shows the vertical distribution of hydrometeor types for the same volume scan. In the observations, most of the pixels result from snow or light rain signatures where the number of snow and rain pixels is almost equally distributed around the melting layer. There also appears a large number of pixels classified as graupel but significantly less than snow pixels and, furthermore, different hail signature above and with an increased number below the melting layer. The height of the melting layer at 3 km is clearly visible from the peak in the dry hail class although it was not visible in the vertical profiles of reflectivity.

Once again, the simulations look quite different from the observations. In the 2 component scheme, the precipitation only consists of rain and snow with some signatures of heavier ice hydrometeors in the region of the melting layer. In contrast to the observations, the number of rain pixels is significantly decreased in comparison to the number of snow pixels. Looking at the 3 component scheme, the only difference to the 2 component scheme is the presence of graupel above the 0° C isotherm. The number of graupel particles is in the same order as the number of snow particles or even higher which contradicts the observations. The Thompson scheme almost produces no rain at all and as in the other schemes heavier ice hydrometeors only appear in the region of the brightband. Nevertheless, this microphysical scheme represents best the distribution of snow and graupel particles above the melting layer producing almost the same number of pixels in the different classes of hydrometeors as observed. Comparing the brightband signatures in the observed and synthetic hydrometeor classification, in all model runs the height of the 0° C isotherm is overpredicted.

A second volume scan was performed at 19 UTC encompassing 6 elevation angles from 1 to 7°. As has been shown in the PPI scans (Figure 6.4) at this time, the system was al-

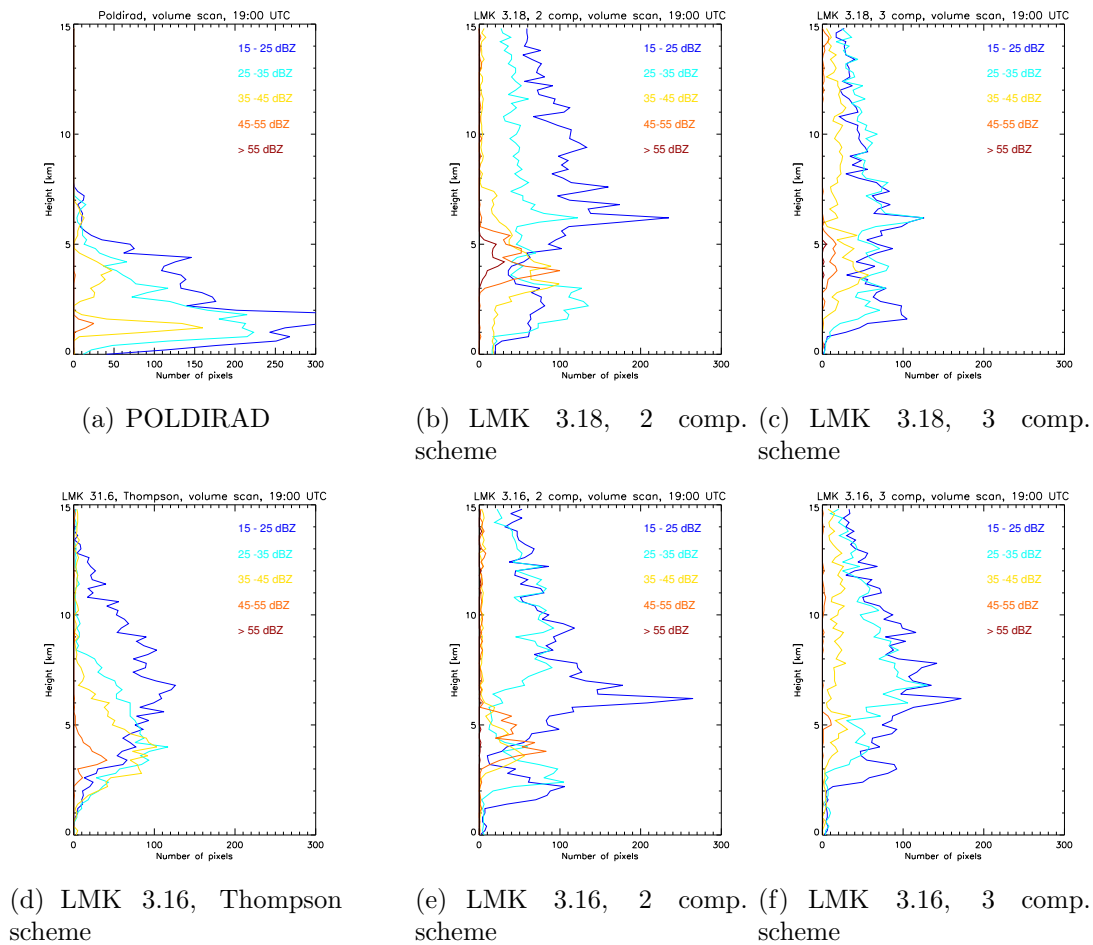


**Figure 6.9:** Observed and simulated histograms of reflectivity [dBZ] as a function of height for a volume scan at 19:00 UTC encompassing 6 elevations from  $1 - 7^\circ$ .

ready decaying in intensity while the spatial extent of the precipitation strongly increased as compared to the earlier volume scan. The decay of the system with a shift from the high reflectivities to more pixels with lower reflectivities can also be seen in the vertical distribution of reflectivity in Figure 6.9. The height of the system has decreased with the lowest reflectivities reaching up to 9 km in contrast to 14 km at 17:00 UTC while the total number of pixels has doubled with more than 300 pixels in the reflectivity class from 15 to 25 dBZ. The very high reflectivities only appear at that time in the region of the melting layer. However, the shape of the vertical distribution of the different reflectivity classes still resembles a Christmas tree with the lowest number of pixels per height interval for the highest reflectivities. In the model, the simulations look relatively similar to the 17:00 UTC results apart from the fact that now also simulated observations near the ground are available and that the total number of pixels is increased to the earlier plot. Although, in the vertical distribution of reflectivity no great changes appear compared to the earlier time step, the vertical distribution of temperature has changed as can be seen in the height of the brightband structures. The height of the melting layer increased in the simulations from 4 or 4.5 km to 5.5 or 6 km depending on the model configuration as compared to the 17:00 UTC volume scan while it decreased in the observations from 3 to 2 km.

In the observations (Figure 6.10), the hydrometeor classification shows mainly pixels classified as rain or snow as for the earlier volume scan but with an significantly increased portion of graupel particles especially at lower altitudes. While in the 17:00 UTC scan, the number

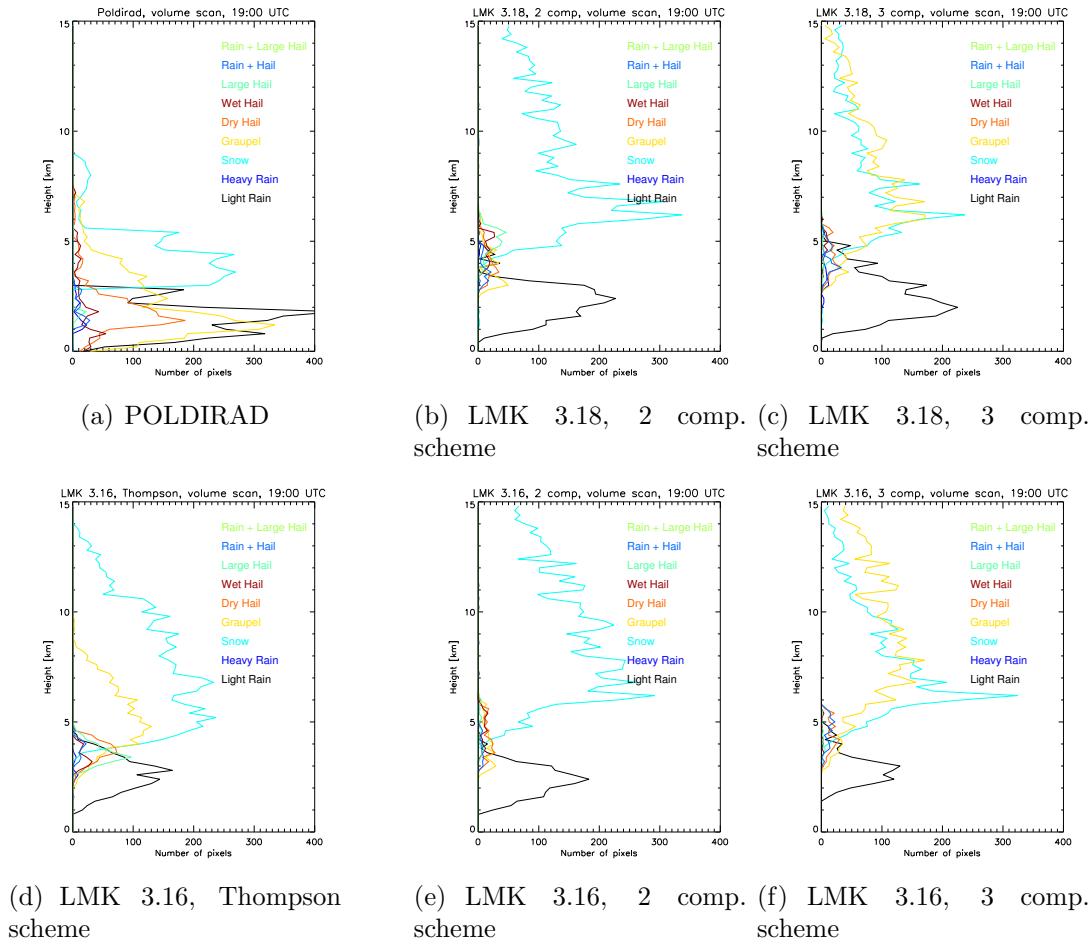


**Figure 6.10:** Observed and simulated histograms of hydrometeor classification as a function of height for a volume scan at 19:00 UTC encompassing 6 elevations from 1 – 7°.

of graupel particles was about half the maximum number of snow or rain now it exceeds the values of snow clearly and is in the order of 3/4 the value of rain. Interpretation is difficult but this increased number could be related to brightband effects because the peak of dry hail is almost at the same altitude. In the simulations, the strength of the event shown in the total number of pixels and the vertical extent of the system is clearly overpredicted. However, the findings regarding the vertical distribution of hydrometeors from the last time step can be confirmed. The 2 component scheme only consists of rain and snow as it is assumed by the microphysical scheme. Signatures of heavier ice species only exist in the region of the brightband due to melting snow. The 3 component scheme also produces graupel signatures where the number is in the same order as the number of snow pixels in contrast to the observations while the Thompson scheme is the only microphysical parameterization scheme reproducing the observed ratio between pixels with graupel and snow signatures.

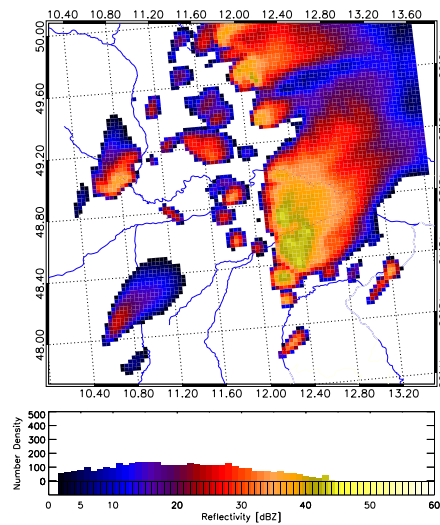


**Figure 6.11:** Synthetic CAPPI of reflectivity [dBZ] at 480 hPa derived from the LMK 3.18 employing the 3 component scheme at 19:00 UTC for August 12th, 2004.

Concluding, the volume scans showed for the observations a typical vertical distribution of classes of reflectivity in a Christmas tree shape with the total number of pixels decreasing for a given height with increasing intensity. At 17:00 UTC when the system was still active, the existence of pixels within the classes of high reflectivity throughout the vertical extent of the precipitation fields clearly proves the presence of highly rimed ice particles reaching the ground before melting. As for the vertical distribution of hydrometeor types, a significant difference between the probability of snow and graupel signatures was observed. For both volumes scans, much higher numbers of pixels were produced for snow than graupel. In the simulations, only the Thompson scheme was able to reproduce the observed ratio of snow and graupel particles and to some extent also the vertical distribution of reflectivities with the decrease of pixels with increasing reflectivity.

For a better understanding of the results derived from the volume scans, observed and simulated RHI scans will be discussed in the following examining the spatial distribution of polarimetric parameters and hydrometeor types in vertical cross sections. Observing convection, the position of the RHI is often chosen to sample the cells with the highest reflectivities. Therefore, similar criteria should be applied to find the RHI with the most resemblance to the observed one in the model domain. For a PPI as well as for a RHI scan, the spatial distribution of intensities of the measurements critically depends on the height or position where the radar beam intersects the precipitation and, therefore, different positions of the radar would result in different patterns of reflectivity and polarimetric quantities for the same precipitation field. This problem can be avoided looking at a CAPPI (constant altitude PPI) which is shown in Figure 6.11 for a constant pressure of 480 hPa derived from the 19:00 UTC simulations of the LMK 3.18 including the 3 component scheme. The areas with the largest reflectivities for the same height can easily be found in the model domain.

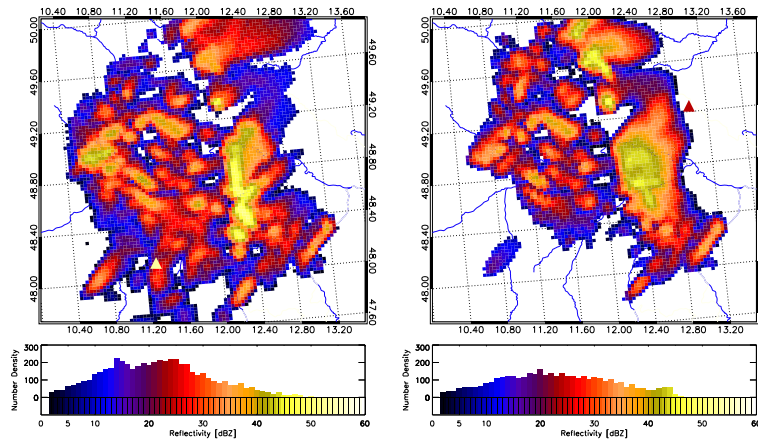


**Figure 6.12:** Synthetic  $1^\circ$  PPI scans for two different positions of the synthetic radar in the model domain derived from the LMK 3.18 employing the 3 component scheme at 19:00 UTC for August 12th, 2004. Shown are on the left the PPI scan for the real POLDIRAD coordinates ( $48.08^\circ$  latitude,  $11.26^\circ$  longitude) and on the right the PPI scan located at the position of the synthetic RHI ( $49.2^\circ$  latitude,  $13.0^\circ$  longitude).

The synthetic RHI scan was chosen to intersect this region of highest reflectivities and, therefore, the radar was positioned at  $49.2^\circ$  latitude and  $13.0^\circ$  longitude in the model domain. The RHI was then executed at an azimuth angle of  $210^\circ$  and elevations from  $0 - 30^\circ$ . Figure 6.12 shows the  $1^\circ$  PPI scans for the different locations of the radar: First, the simulations for the real POLDIRAD coordinates and, second, the position for the synthetic RHI scan. For all model configurations, the same RHI scans were simulated as the differences in the positions and the spatial structure of the convective cells within the different model runs were relatively small. These RHI scans will be compared to a POLDIRAD RHI observed at 19:23 UTC at an azimuth angle of  $99^\circ$ .

Figure 6.13 shows the observed RHI together with the synthetic RHI scans. The observations show a convective system with two convective cells on the right of the figure and a stratiform region of precipitation on the left. The distribution of maximum reflectivities within the storm depicts the sharp transition in the dynamics for the stratiform and the convective part. The highest reflectivities appear within the right convective cell reaching values up to  $55$  dBZ and these enhanced reflectivities are equally distributed throughout the vertical extent of the cell from the ground up to an altitude of  $6$  km. In the stratiform region the maximum reflectivities are organized in a brightband structure with values of reflectivity exceeding  $35$  dBZ while the reflectivities in rain reach values of  $30$  dBZ and in snow slightly smaller values of  $28$  dBZ.

The synthetic RHI scans show a similar organization of the dynamics with a region of stratiform precipitation on the left and a convective cell on the right. Although the convective cell exists in the model simulation, the intensity of the observations is clearly underestimated for all model configurations while the vertical extent of the storm and the height of the melting layer are overestimated. The differences between the LMK versions are very small in com-

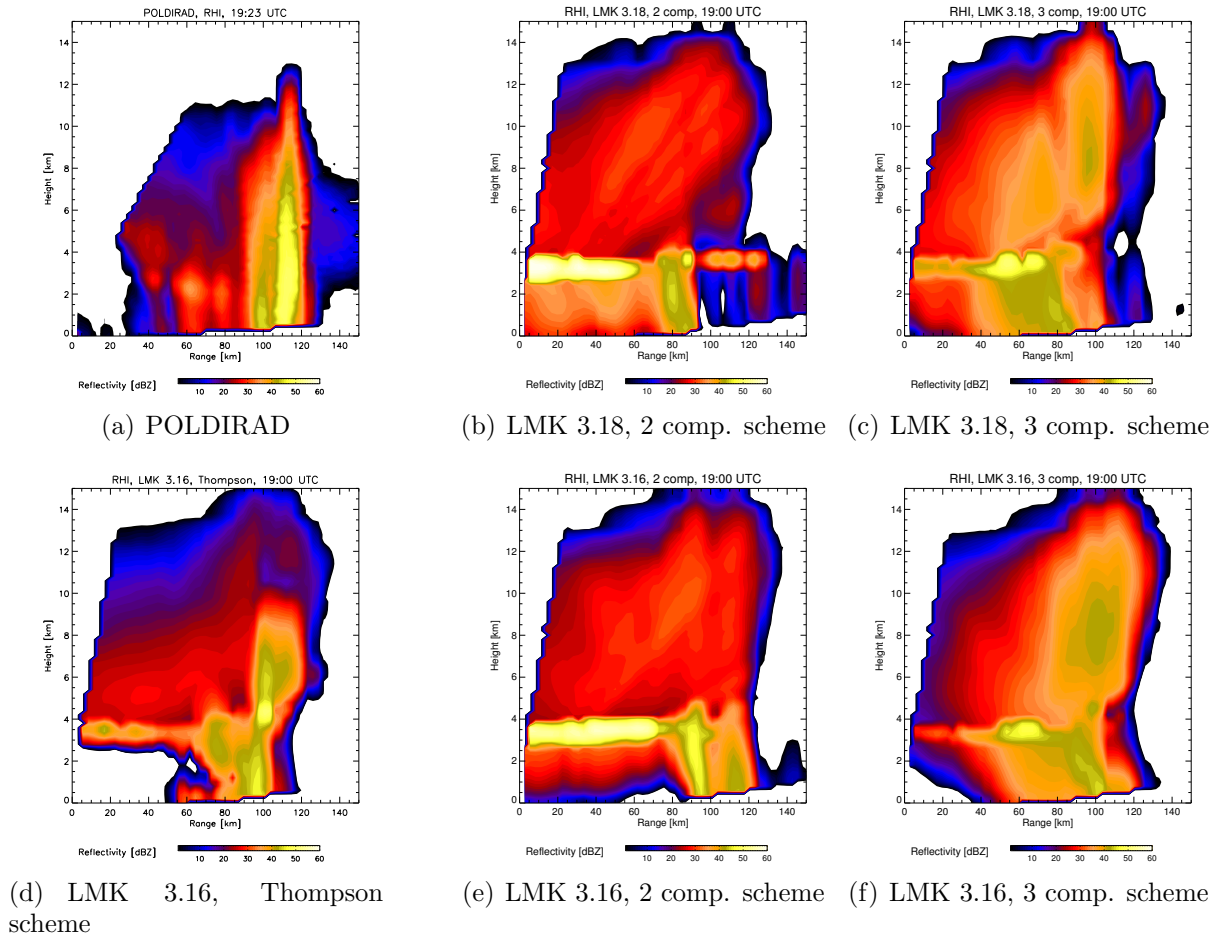


**Figure 6.13:** Observed (19:23 UTC) and simulated RHI of reflectivity [dBZ] for different model versions of the LMK at 19:00 UTC.

parison to the differences between the microphysical schemes and, therefore, the discussion will focus on the parameterization schemes.

The synthetic RHI scans derived from the simulations including the LMK 2 component scheme are dominated by an enhanced brightband signature in the stratiform precipitation while the convective core is hardly detectable. In the ice phase, no differences between the convective and the stratiform part of the storm can be found and the convective core is only visible in the enhanced reflectivities in rain with reflectivities ranging from 45 to 50 dBZ. While the convection is underestimated, reflectivities in the stratiform precipitation are overestimated. This is especially true for the brightband where reflectivities up to 60 dBZ are observed but also in the snow reaching values of 30 dBZ in comparison to the observed 10 – 25 dBZ, and the rain with values up to 40 dBZ. The extreme reflectivities within the brightband result from melting snowflakes which are very effective in attenuating the radar beam because of their size and enhanced dielectric constant. This results in strong attenuation in the ice phase making the beam pattern visible. For the 3 component scheme, the RHI scans looks similar but in contrast to the two component scheme, the convective core can now be detected within the ice phase although reflectivity is still clearly underestimated. The intensity of the brightband has weakened featuring now more realistic values of 20 – 40 dBZ.

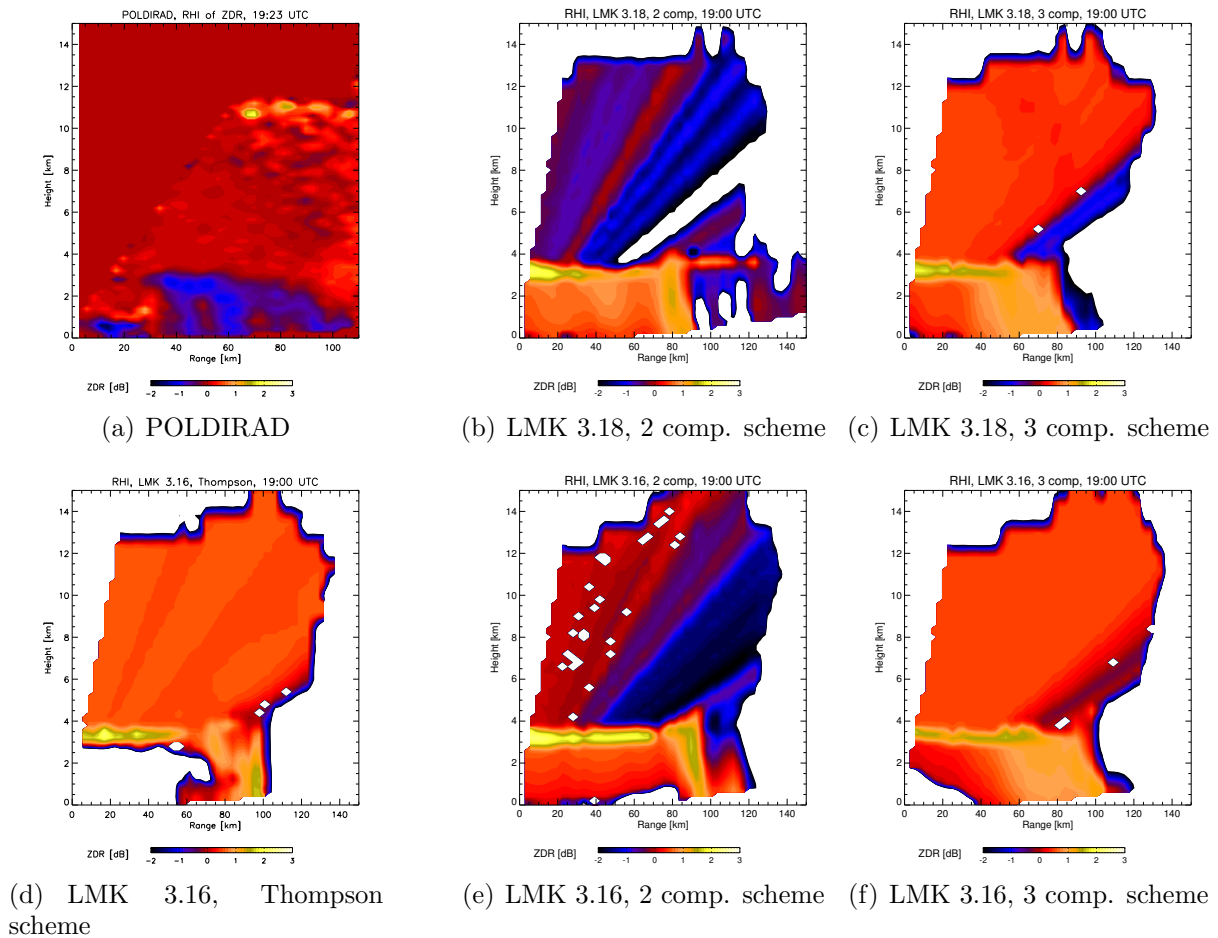


**Figure 6.14:** Observed (19:23 UTC) and simulated RHI of  $Z_{DR}$  [dB] for different model versions of the LMK at 19:00 UTC.

However, for these simulations a new problem has appeared with a large discontinuity in reflectivity within the convective core at the height of the melting level showing enhanced values which are not observed. Generally it can be stated that although the 3 component scheme shows a more realistic distribution of reflectivities than the 2 component scheme, the convective core is still strongly underestimated and the transition in dynamics from the convective to the stratiform precipitation with a pronounced decrease in reflectivity. This is especially true in the ice phase which is not at all represented by the model. In contrast to this the Thompson scheme produces the RHI scan with the most resemblance to the observed RHI clearly showing a convective cell and a region of stratiform precipitation. Within the convective core, reflectivities are equally distributed above and below the melting layer reaching values of 45 dBZ and thus still underestimating the observed ones. As in the 3 component scheme, a comparable brightband signature appears in the region of the melting layer within the convective core reaching values up to 50 dBZ. Nevertheless, the Thompson schemes simulates the most realistic reflectivities of all schemes for both the convective part of the storm as well as for the stratiform precipitation proving its ability to reproduce the different microphysical processes for the given dynamical regimes. In the stratiform part of the precipitation, the reflectivities in the snow and the brightband are more realistic reaching

values of 10 – 25 dBZ for the snow and 30 – 43 dBZ for the brightband. However, in this scheme all the rain evaporates before it reaches the ground.

Regarding the observations of  $Z_{DR}$  (Figure 6.14), the maximum values are found within the brightband due to the enhanced polarimetric signatures for melting snow as well as for regions with heavy rain where the number of large rain drops is especially large. These maximum values are in the order of 1.3 dB. Within the convective core, the observations are strongly attenuated and, therefore, no signal has been processed. For the 2 component scheme,  $Z_{DR}$  is overestimated with values up to 2 dB in the region of the brightband where already reflectivity showed unrealistic high intensities. This proves that for melting snow increasing mixing ratios positively impact  $Z_{DR}$  due to the enhanced number of large particles. For the 3 component and the Thompson scheme,  $Z_{DR}$  values are also overestimated in comparison to the observations but not to the same extent as in the 2 component scheme. Furthermore, all models produce increased values of  $Z_{DR}$  within the convective core, but no larger differences in  $Z_{DR}$  for the stratiform precipitation.

In the observations of  $L_{DR}$  (Figure 6.15), enhanced signatures exist within the brightband which are also reproduced by the simulations in the same order of magnitude. Major dif-

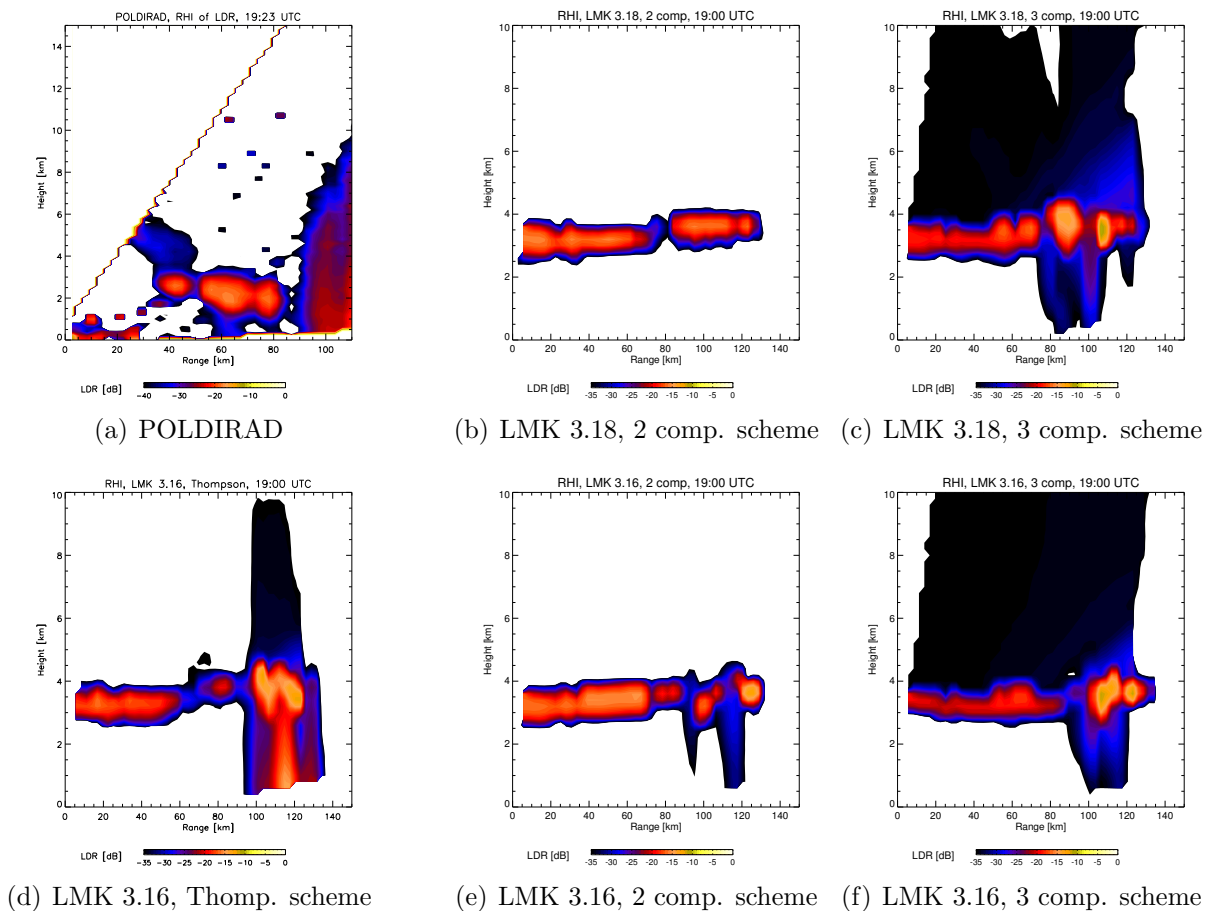


**Figure 6.15:** Observed (19:23 UTC) and simulated RHI of  $L_{DR}$  [dB] for different model versions of the LMK at 19:00 UTC.

ferences arise in the region of heavy precipitation within the convective cell where in the

observations especially high values exist from the ground up to 4 km height. In the simulations the enhanced values of  $L_{DR}$  in the convective core are only reproduced by the Thompson scheme below the melting layer while within the melting layer unrealistic values up to  $-5$  dB are found related to the extreme reflectivities of 55 dBZ that were discussed earlier. However, no enhanced values of  $L_{DR}$  are found above the melting layer in contrast to the observations. The absence of higher values of  $L_{DR}$  within the ice phase which would result from heavily rimed ice hydrometeors is an indicator that the increased values in the rain are only due to attenuation effects behind cores of heavy rain and are not due to graupel or hail particles reaching the ground before melting. This is also true for the other microphysical schemes producing observable values of  $L_{DR}$  below the melting layer.

The hydrometeor classification derived from the observed and computed polarimetric parameters is shown in Figure 6.16. In the observations, the convective core and the brightband

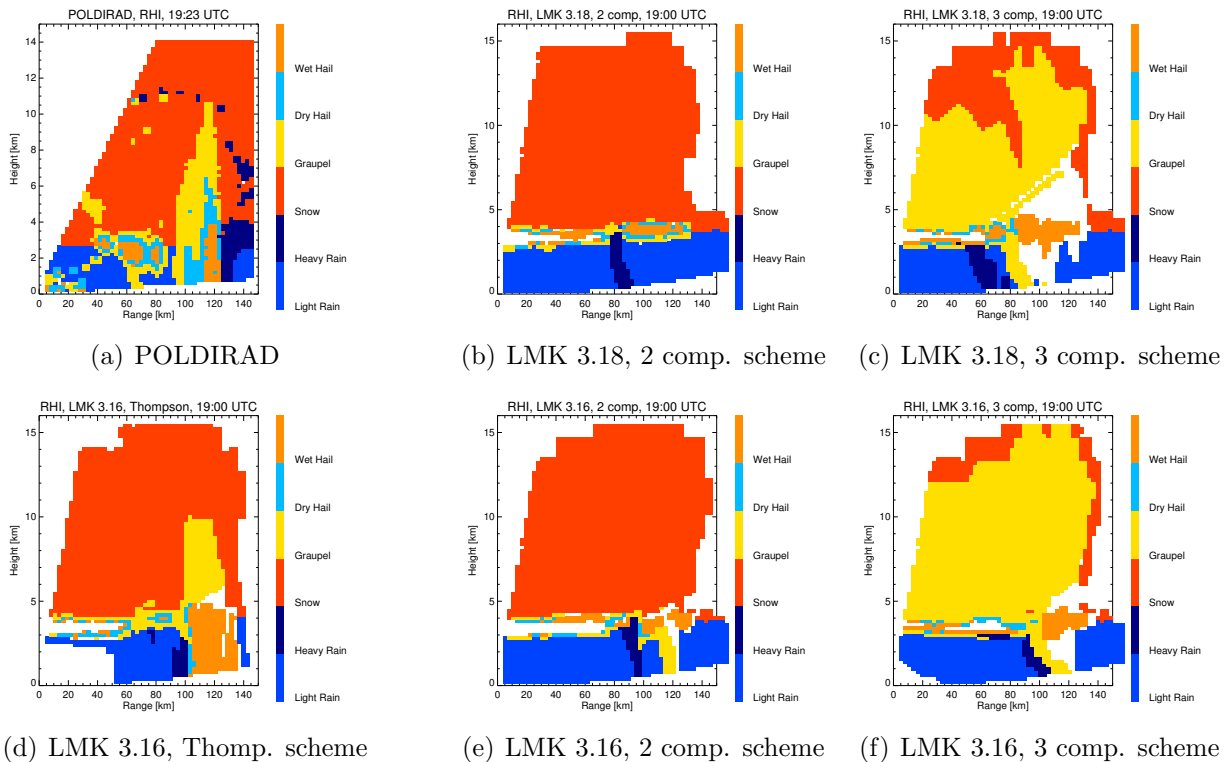


**Figure 6.16:** Hydrometeor classification derived from observed (19:23 UTC) and simulated polarimetric quantities for different model versions of the LMK at 19:00 UTC.

are classified as a mixture of graupel and hail and can be clearly distinguished from the stratiform precipitation consisting of snow and rain. The hail and graupel signatures in the convective core extend from the ground to a height of 11 km and show that heavily rimed ice is present throughout the whole vertical extent of the convective core. In the simulations, the picture looks totally different: In the 2 component scheme, the system consists only of snow and rain with signatures of heavy rain in the region of the convective core which is consistent with the model assumptions only considering these two types of precipitating hydrometeors. In the melting layer, signatures of denser ice hydrometeors appear because of the enhanced polarimetric parameters due to melting snow. In the 3 component scheme, the

ice phase is dominated by graupel and almost no snow signatures exist. Only the Thompson scheme is able to reproduce the areas of snow and graupel as seen in the observations. In both, the 3 component and the Thompson scheme, a graupel signature exists below the brightband which is due to the enhanced values of  $L_{DR}$  discussed in the last section and is supposed to result from attenuation effects. In order to prove this hypothesis, the mixing

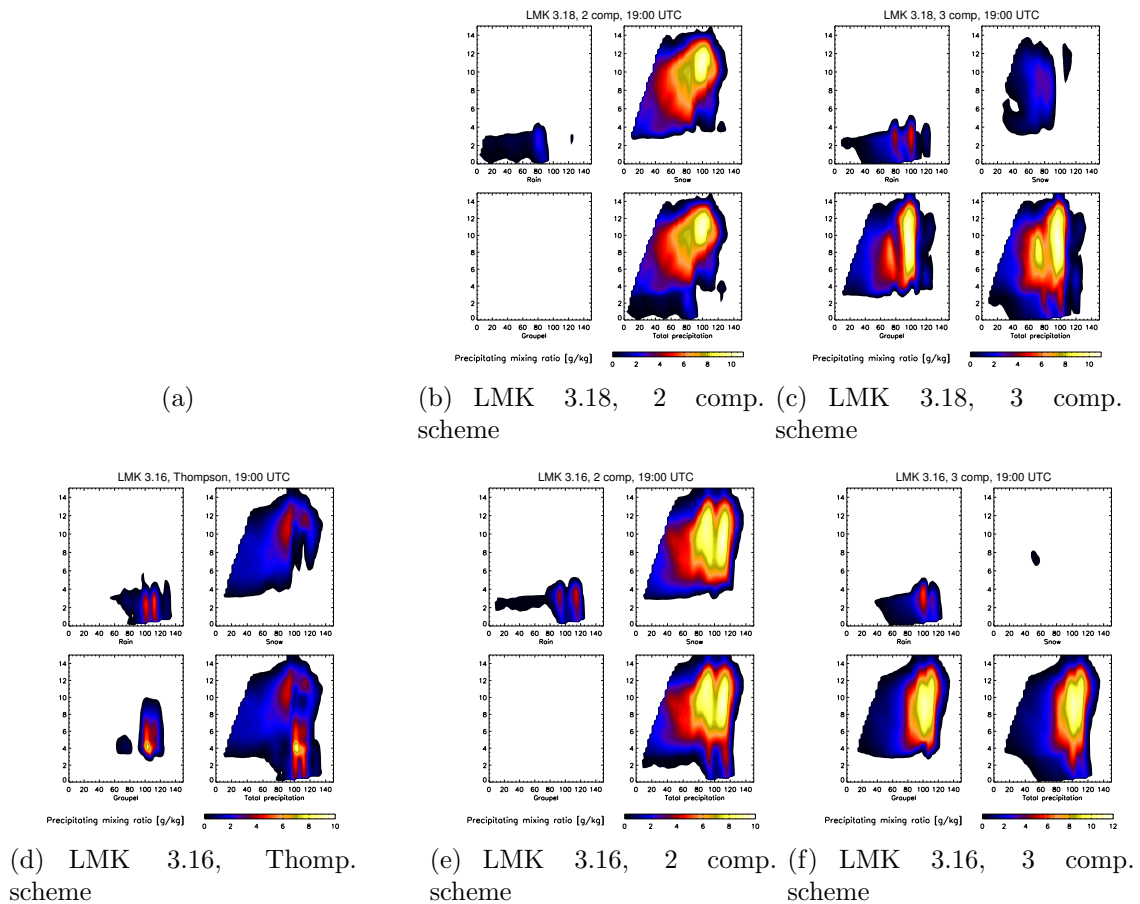


**Figure 6.17:** Mixing ratios of the different hydrometeor types as well as total precipitation [ $\text{g kg}^{-1}$ ] derived from different versions of the LMK along the vertical cross section of the RHI scans. This information is not available from the POLDIRAD observations.

ratios of the different hydrometeors for the different model configurations along the path of the radar beam will be discussed. While the models produce similar mixing ratios of rain (Figure 6.17) once again major differences are found in the ice phase. The smallest total amount of precipitation is produced by the Thompson scheme with maximum values in the graupel of  $8 \text{ g kg}^{-1}$ . Regarding the spatial extent, most of the ice phase consists of snow with a maximum mixing ratio of  $5 \text{ g kg}^{-1}$  and graupel only exists in a small sharply defined area directly above the region with heavy rain as was already shown in the classification scheme. For the LMK schemes, the maximum mixing ratios in the ice phase are comparable for all different model configurations reaching values up to  $12 \text{ g kg}^{-1}$  and, therefore, clearly exceeding the maximum values produced by the Thompson scheme. In the 3 component scheme, the graupel dominates the ice phase in the total amount of precipitation as well as in the spatial distribution covering larger areas than snow. The presence of graupel in the

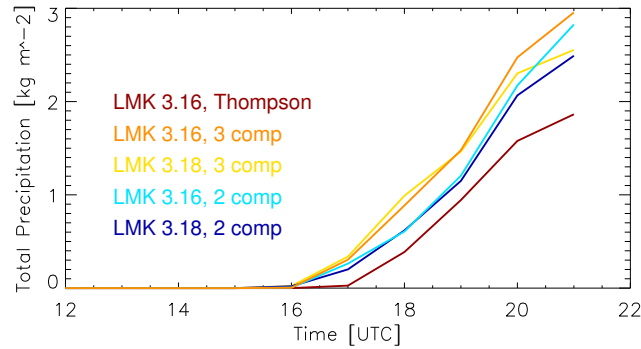


**Figure 6.18:** Times series of hourly accumulated total precipitation [ $\text{kg m}^{-2}$ ] averaged over the model domain for all LMK configurations.

region of the stratiform precipitation for the 3 component scheme also explains that  $Z_{DR}$  is not overestimated to the same extent as in the 2 component scheme. Graupel is assumed to have a larger axis ratio than snow and, therefore, contributes less to  $Z_{DR}$ . This is also true for the overestimation of reflectivity within the melting layer which is not as large for the 3 component scheme as for the 2 component scheme and can be explained with the differences in the assumptions of PSD. The intercept parameter of graupel is one order of magnitude larger than the one for snow producing for the same mixing ratio a steeper PSD with less large particles contributing to the enhanced reflectivity. Finally, it can be concluded that for all microphysical parameterization schemes signatures of heavier ice species within the convective core and precipitating ice reaching the ground are missing and that the graupel signatures in the classification schemes below the melting layer are due to attenuation of  $L_{DR}$  in heavy rain.

The differences between the microphysical parameterization schemes also appear in the accumulated precipitation. Figure 6.18 gives the total precipitation accumulated over one hour and averaged over the model domain as a function of time. The 3 component scheme produces significantly more precipitation as the 2 component scheme while the differences between the LMK versions are marginal. The smallest amount of precipitation at the ground is given by the Thompson scheme which is consistent with the RHI of reflectivity (Figure 6.13) where all the precipitation within the stratiform rain evaporated before reaching the ground.

## 6.4 Evaluation of the MesoNH

The results from the LMK showed that the number of ice hydrometeor types and the related microphysical properties are of utmost importance for a realistic representation of a convective precipitation event. In order to study the influence of an additional ice hydrometeor on the performance of NWP models, the LMK results will be compared to simulations from the French research model MesoNH. The MesoNH was run with a microphysical schemes considering rain, snow, and graupel as prognostic precipitating hydrometeors comparable to the LMK 3 component scheme and another one including an additional hail class. For the

MesoNH, no evaluation of the life cycle will be done because only selected time steps of the simulations are available. Therefore, the discussion will concentrate on the volume scans and RHI scans at 19:00 UTC.

Figure 6.19 shows the 1° PPI scans as observed by POLDIRAD and simulated by the two model versions of the MesoNH at 19:00 UTC for August 12th, 2004. The precipitation is

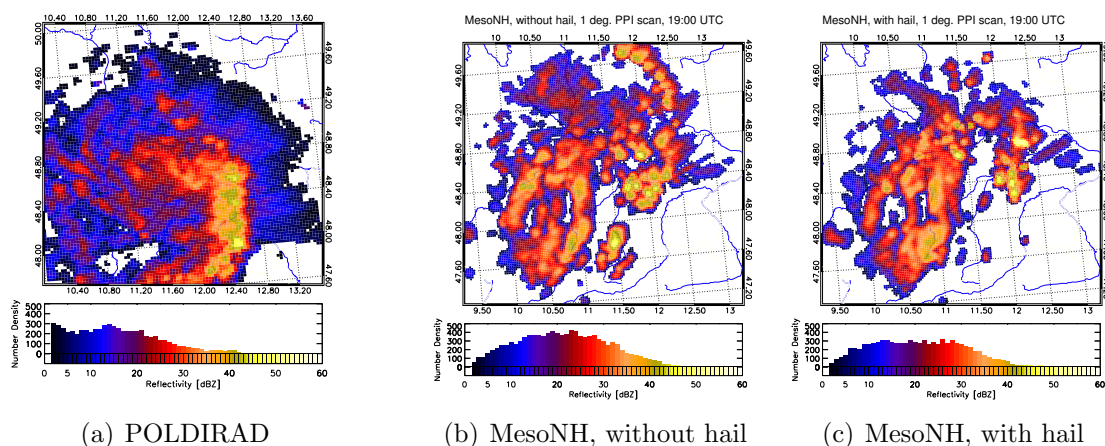
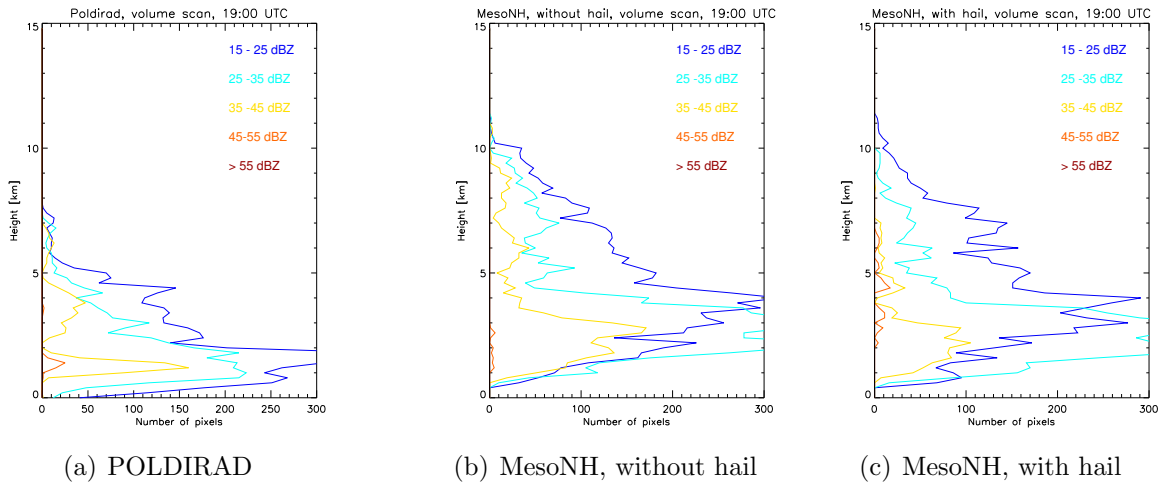


**Figure 6.19:** Observed and simulated 1° PPI scans of reflectivity [dBZ] for the French research model MesoNH in the model versions without and with hail at 19:00 UTC.

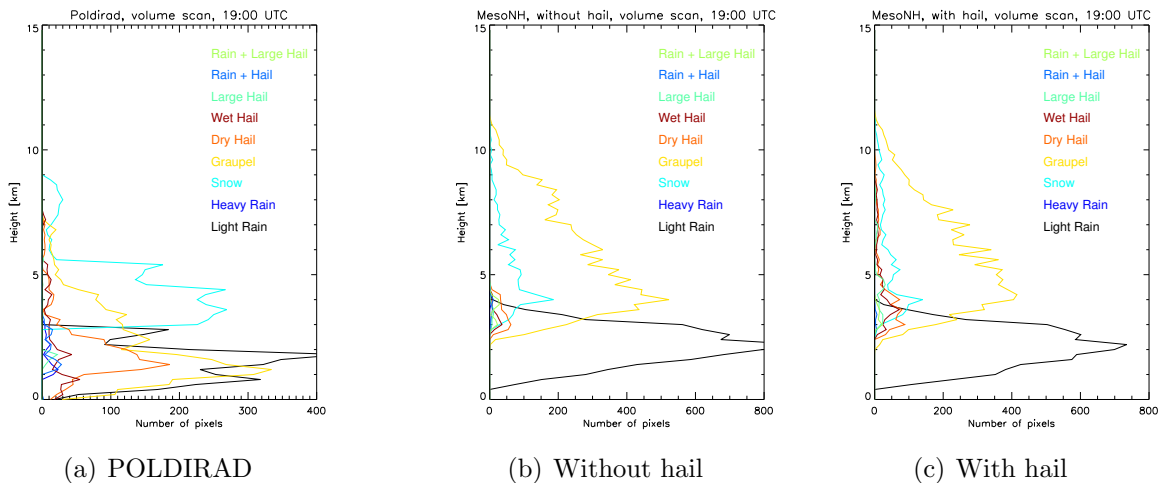
spread over a large area with several convective cells where the differences between the two model versions remain small. The convection is not organized as clearly as in the observations although some linear structure can be found. However, the observed coexistence of the well defined line of convection and the wide spread stratiform precipitation is not at all captured by the model. This is also shown in the distribution of reflectivities where the higher reflectivities are well represented with some convective cells reaching values up to 45 dBZ while the number of pixels with lower reflectivities is clearly underestimated.

In order to have a closer look at the vertical distributions of reflectivities and hydrometeors, the volume scans are displayed in Figure 6.20 in the same way as the LMK results in Figure 6.9. In the MesoNH, the classes of reflectivity are distributed in the Christmas tree shape similar to the observations with maximum number of pixels for the smaller reflectivity classes and decreasing number of pixels for the higher reflectivity classes. However, there are some differences: first, the simulated storm extends to higher altitudes reaching 11 km as compared to the 9 km found in the observations. Second, a decent number of pixels within the reflectivity class of 45 – 55 dBZ exists at altitudes from 2 – 7 km for the simulations considering hail which are not any more present in the observations at that time step. In the observations, these high reflectivities only exist in a well defined layer between 1 – 2 km and can, therefore, be attributed to brightband effects as it is also shown in the simulations for the model version without a hail phase.

Comparing the vertical distribution of hydrometeors (Figure 6.21), the overestimation of the number of pixels with graupel strikes most. While in the observations the ice phase consists two thirds of snow and approximately one third of graupel, in the simulations the ratio is reversed. Furthermore, the height of the melting layer in the model is overpredicted with 4 km in comparison to 3 km and there are no signatures of heavier ice hydrometeors found below the melting layer. Therefore, the MesoNH reproduces better the actual height of the



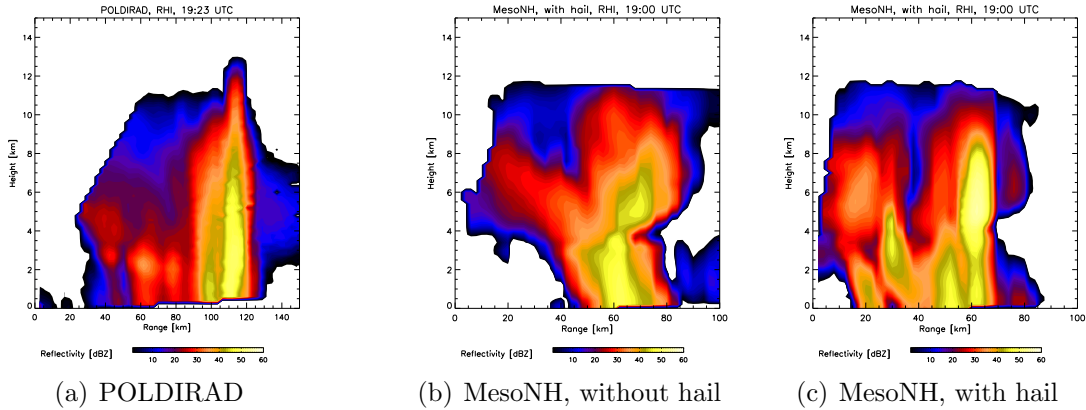
**Figure 6.20:** Vertical distribution of classes of reflectivity [dBZ] for an observed and simulated volume scan for the French research model MesoNH in the model versions without and with hail at 19:00 UTC.



**Figure 6.21:** Vertical distribution of hydrometeors for an observed and simulated volume scan for the French research model MesoNH in the model versions without and with hail at 19:00 UTC.

system as compared to the LMK as well as the vertical distribution of reflectivities. Looking at the classification, the MesoNH produces more pixels with rain but in the ice phase the number of graupel pixels is clearly overpredicted as compared to the observations and the LMK. Although an hail phase has been introduced in the MesoNH, at least in the volume scans, no hail signatures are visible at the ground.

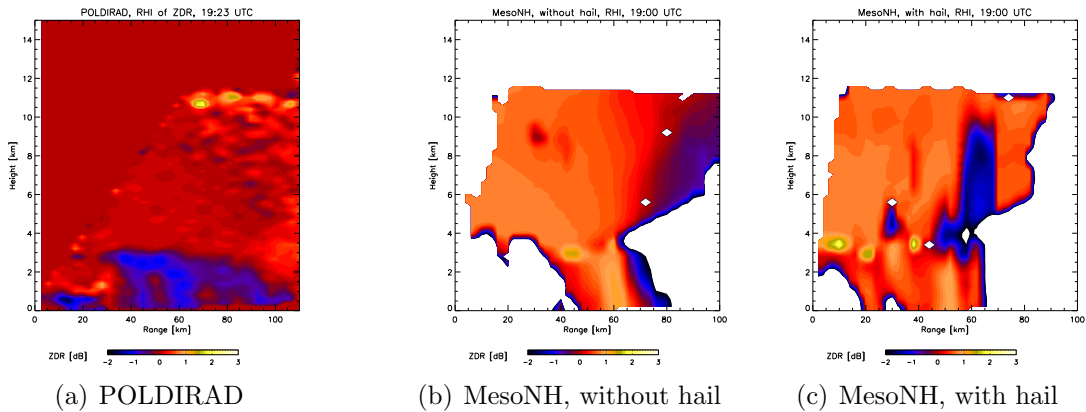
In order to study the differences between the model version including hail and the version without hail more in detail, RHI scans will be discussed. The position of the synthetic radar in the model domain was selected in the same way as for the LMK RHI scans. In the model version including hail, the radar was positioned at a latitude of  $48.9^\circ$ , longitude of  $12.8^\circ$ , and the azimuth angle of the RHI scan was  $227^\circ$ . For the simulations without hail the location of the radar was at a latitude of  $49.2^\circ$ , longitude of  $13.0^\circ$  and the RHI was observed at an azimuth angle of  $225^\circ$ . The RHI of reflectivity (Figure 6.22) shows that for



**Figure 6.22:** Observed (19:23 UTC) and simulated RHI of reflectivity [dBZ] for the MesoNH at 19:00 UTC.

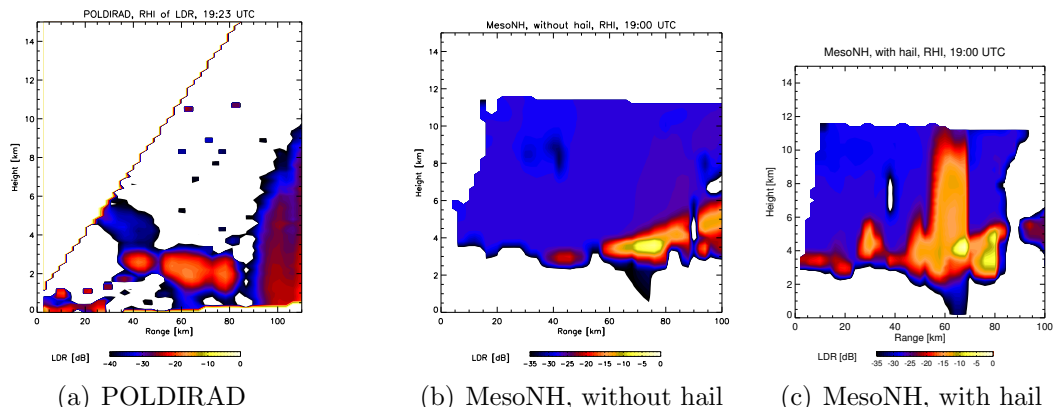
the two model versions the intensities of reflectivity within the convection are comparable to the observations. This is due to the presence of hail as well as the assumptions of the MesoNH describing graupel as a partially soaked particle (see Appendix C). For both model versions, no stratiform region with a well defined brightband can be recognized. Especially in the model version including hail, several small convective cores exist besides the main core of convection. However, the spatial distribution of reflectivities with maximum values in the convective cores looks very similar to the observations. In contrast to the RHI scans simulated from LMK forecasts, in the MesoNH no brightband signatures appear in the convection.

Figure 6.23 shows the same RHI scans for  $Z_{DR}$ . Similar to the LMK simulations, the highest



**Figure 6.23:** Observed (19:23 UTC) and simulated RHI of  $Z_{DR}$  [dB] for the MesoNH at 19:00 UTC.

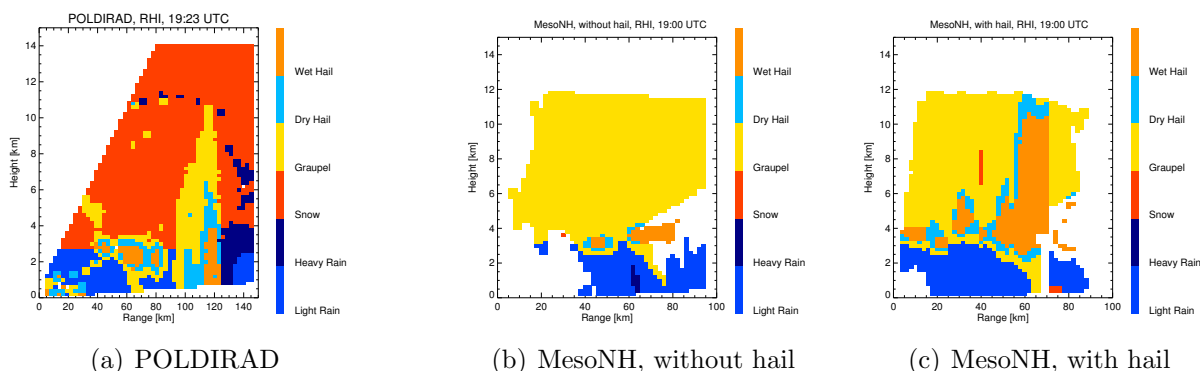
values of  $Z_{DR}$  are found in the region of the melting layer as well as in the convective cores with heavy precipitation. However, the MesoNH simulations result in much more realistic values for the brightband with only slightly enhanced values as compared to the observations. In the simulations of  $L_{DR}$  (Figure 6.24), the highest values are once again found in the region of the brightband and in the case of the simulations considering hail also within the convective core. For the MesoNH model run without the hail class, the  $L_{DR}$  values within the brightband are strongly overestimated with maximum values of  $-8$  dB. These



**Figure 6.24:** Observed (19:23 UTC) and simulated RHI of  $L_{DR}$  [dB] for the MesoNH at 19:00 UTC.

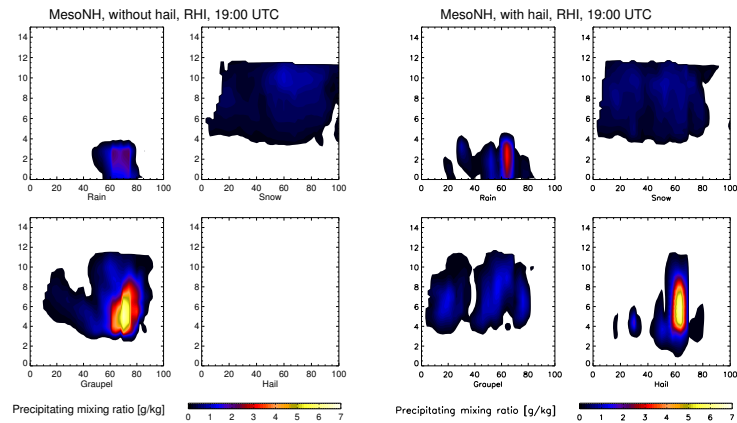
extreme values of  $L_{DR}$  may be due to attenuation within the core of heavy precipitation and the brightband which can be also observed in the increased values behind the  $L_{DR}$  maximum. The small values of  $-35$  to  $-30$  dB below the melting layer can also be attributed to attenuation effects. For the model run considering hail, the brightband signatures are not overestimated to the same extent as in the model run without hail and reproduce the observed signatures quite well. For the convective core,  $L_{DR}$  is strongly overestimated in intensity as well as spatial extent in the higher regions of the precipitation field with values about  $-13$  dB as compared to the observed values of about  $-30$  to  $-25$  dB. In contrast to this overestimation of  $L_{DR}$  in the ice phase, the values in the convective core below the melting layer are clearly underestimated with values below  $-30$  dB in comparison to the observed  $-18$  dB.

Figure 6.25 shows the hydrometeor classification for the MesoNH simulations. In the si-



**Figure 6.25:** Hydrometeor classification derived from observed (19:23 UTC) and simulated polarimetric quantities for the MesoNH at 19:00 UTC.

mulations from the MesoNH version without hail, the ice phase mainly consists of graupel signatures with some signatures of heavier ice species in the region of the brightband and, therefore, resembles strongly the LMK simulations with the 3 component scheme almost totally neglecting the presence of snow. For the model version including hail, the ice phase of the convective core as well as the brightband are classified as hail, therefore, improving the representation of heavier ice species clearly. However, in these simulations almost no



**Figure 6.26:** Mixing ratios [ $\text{g kg}^{-1}$ ] of the different hydrometeor types rain, snow, graupel, and hail along the vertical cross sections of the RHI scans for the MesoNH without (left) and with hail (right) at 19:00 UTC.

pixels are classified as snow while in the observations almost the whole ice phase consists of snow apart from the inner core of the convective cell. Furthermore, the area classified as hail in the model is much larger and extends to higher altitudes as in the observations while no hail signatures are present below the melting layer.

Comparing this classification to the mixing ratios of hydrometeors for the given RHI scan, the main results are confirmed (Figure 6.26). For the two model runs holds that the snow phase is present together with graupel but due to the larger dielectric constant of graupel the polarimetric parameters are dominated by the microphysical properties of graupel. Furthermore, the precipitation fields show that the graupel signatures below the melting layer are due to attenuated  $L_{DR}$ . Although the MesoNH considers an additional hail class, no signatures of densely rimed ice hydrometeors reaching the ground appear in the simulations. The maximum mixing ratios are found with similar magnitudes in the heaviest ice hydrometeor phase considered by the different microphysical schemes and the precipitation water contents are smaller for the MesoNH in comparison to the LMK although the synthetic reflectivity is more realistic.

## 6.5 Discussion

The ability of a mesoscale NWP to reproduce a convective event associated to a cold front crossing southern Germany has been evaluated for the LMK considering three different microphysical schemes and the MesoNH considering two microphysical parameterization schemes. In general, the models were able to reproduce a comparable event but the timing and the decay of the storm were not captured by the different model versions. In the first hours when the system was still growing in the observations, the storm was underestimated while in the following the simulated system developed further missing totally the decay of the observed storm to a wide spread stratiform precipitation event.

The comparison between the observed and the synthetic radar parameters showed large

discrepancies especially regarding the vertical distribution of reflectivity, polarimetric quantities, and hydrometeor types. For the RHI scans, all model versions produced a similar spatial structure with a convective core and a region with stratiform precipitation but not as clearly defined as in the observations. The intensity of reflectivities was underestimated while the vertical extent of the storm and the height of the melting layer were overestimated. The 2 component scheme had major problems in the representation of the reflectivities in the ice phase where the convection was hardly distinguishable from the stratiform part of the cloud. Furthermore, extreme values of reflectivity and  $Z_{DR}$  appeared in the brightband signatures. These enhanced brightband signatures resulted in extreme attenuation in the ice phase clearly showing the pattern of the radar beam. The introduction of a graupel class in the 3 component scheme enhanced the performance of the LMK showing a more realistic distribution of reflectivities but still underestimating the intensities within the convective core. In contrast to this, the Thompson scheme reproduced the RHI scans with the most resemblance to the observed one clearly distinguishing between the convective cell and the region of stratiform precipitation. However, these simulations considering graupel produced a maximum in reflectivity within the convective core at the height of the melting level. The MesoNH reached for the two model versions the best resemblance of reflectivities for the convective core and in contrast to the LMK simulations no brightband signatures were found in the core of heavy precipitation.

These results were confirmed during the discussion of the vertical profiles of reflectivities and hydrometeor types derived from volume scans. For all LMK schemes, no pixels of higher reflectivities were found above the melting layer giving evidence of heavier ice hydrometeors. Furthermore, neither the typical shape nor the decrease of the number of pixels with increasing reflectivity were reproduced. In contrast to the LMK schemes, the simulations from the MesoNH matched very well the typical vertical distribution of reflectivity classes as well as the decreasing number of pixels for the higher reflectivity classes. However, differences resulted from the overestimation of height of the simulated storm and the enhanced reflectivities that were not any more existing in the observations at that time step.

Regarding the hydrometeor classification similar discrepancies were found. In the observations, the convective core and the brightband were classified as a mixture of graupel and hail and were easily distinguished from the stratiform precipitation consisting of snow and rain. The hail and graupel signatures in the convective core extended from the ground to a height of 11 km and proved that heavily rimed ice was present throughout the whole vertical extent of the convective core. In the 2 component scheme, the system consisted only of snow and rain with signatures of heavy rain in the region of the convective core. In the 3 component scheme, the ice phase was dominated by graupel and only the Thompson scheme was able to reproduce the observed distribution of snow and graupel. For the MesoNH model version including hail, the ice phase of the convective core was classified as hail, therefore, improving the representation of heavier ice species. However, for the two MesoNH versions the ice phase was dominated by graupel signatures while the snow was almost totally neglected as in the LMK 3 component scheme. Furthermore, the areas classified as hail in the model simulations were much larger and extended to higher altitudes than in the observations while no hail signatures were present below the melting layer. Thus, although the MesoNH considers an additional hail class no signatures of densely rimed ice hydrometeors reaching the ground were found in the simulations.

The volume scans showed further that the observed height of the melting layer as well as

the total vertical extent of the precipitation decreased from 17:00 UTC to 19:00 UTC while it increased in the simulations. The reason for this missing cooling of the atmosphere could be in the nonexistence of heavier ice hydrometeors redistributing the latent heat as well as the bad distinction between graupel and snow. This can also explain for the missing decay of the simulated storm. However, it is also possible that the effect is due to the boundary conditions.

Generally, the consideration of graupel as an additional precipitating ice hydrometeor clearly enhanced the capabilities of the LMK to simulate explicitly convection. However, major improvements have to be done in the LMK and MesoNH for a better distinction between the snow and graupel phase in different dynamical situations. The MesoNH simulated best the actual height of the system as compared to the LMK as well as the vertical distribution of reflectivities. The Thompson schemes reproduced the most realistic reflectivities of all schemes for both, the convective and the stratiform part of the storm proving its ability to distinguish between the different microphysical processes in stratiform and convective precipitation. However, in this scheme a major part of the precipitation evaporated before reaching the ground.

The discrepancies between the different model runs resulted from the differences between the microphysical parameterization schemes and not from the LMK model versions. Combining different model versions for the evaluation of the microphysical parameterization schemes can be understood as a mini-ensemble providing different dynamical realizations of the storm. This increases the statistical significance of the results as long as the derived information about the skill of the parameterization schemes conforms as it was the case in this study. The importance of microphysical parameterization schemes on the quantitative precipitation forecast was shown in the comparison of the accumulated precipitation at the ground where the 3 component scheme produced significantly higher intensities than the 2 component or the Thompson scheme. The evaluation based on polarimetric quantities and the hydrometeor classification proved that the differences in the simulated precipitation structures were due to the number of assumed ice hydrometeors and their microphysical characteristics. This was especially true for the MesoNH where the reflectivities were very well reproduced showing that the scheme was tuned against conventional radar observations while major discrepancies appeared in the distribution of hydrometeor types.

The overprediction of graupel in comparison to snow that was found in the LMK and MesoNH may be due to an overprediction of cloud water and, therefore, enhanced riming. Other possible reasons are wrong assumptions regarding the thresholds for autoconversion rates or the general characteristics between the assumed graupel and snow being too similar. This can be due to the assumed particle size distribution as well as density. For all microphysical parameterization schemes signatures of heavier ice species within the convective core and precipitating ice reaching the ground are missing. It is strongly assumed that this had major impact on the representation of the life cycle of the storm. However, this can not be confirmed without further investigating the impact of the boundary conditions on the representation of the storm in the context of a systematic long term evaluation.

# Chapter 7

## Conclusions and Outlook

The aim of this thesis was to develop methods allowing the information content of polarimetric radar data to be employed for the evaluation of microphysical parameterization schemes in mesoscale NWP models. Polarimetric radar systems are the only remote sensing instruments to provide information on the intensity and the microphysical characteristics of a precipitation event at high temporal and spatial resolution. Therefore, these observations are especially suited for evaluating microphysical parameterization schemes. However, the observed quantities are not directly related to the parameters considered in mesoscale models inhibiting a direct comparison. In order to establish a relationship between the model parameters and the observations, the polarimetric radar forward operator SynPolRad has been developed. SynPolRad simulates synthetic polarimetric radar quantities out of forecasts provided by NWP mesoscale models allowing for a direct comparison of the intensity and the microphysical characteristics of the precipitation event in terms of observed quantities. The potential of this new method was demonstrated for a stratiform and a convective case study where large discrepancies between the model forecasts and the observations were found. These results showed that the polarimetric radar forward operator SynPolRad provides the means for future systematic model evaluations with the aim to identify substantial model errors and improve the parameterizations. This has the potential to significantly increase model skill especially in the context of short term forecasts of convective precipitation events which will constitute a major step towards better quantitative precipitation forecasts.

SynPolRad has been developed combining the conventional radar forward operator RSM (Haase and Crewell (2000)) with the T-Matrix scattering code (e. g. Bringi et al. (1986)). It computes the synthetic reflectivity, the linear depolarization ratio  $L_{DR}$ , and the differential reflectivity  $Z_{DR}$  from predicted bulk water quantities and simulates the beam propagation in the model domain. This is done under consideration of refractivity using the 4/3 effective earth radius model and simulation of the actual attenuation by the relevant atmospheric gases and hydrometeors. In order to successfully employ SynPolRad for model evaluation purposes, the link between the forward operator and the mesoscale model has to conform as closely as possible to the model assumptions. However, in the case of a polarimetric radar forward operator not all the input parameters are defined by the model. This is especially true for ice phase hydrometeors because of the large natural variability of particle

shapes, densities, and falling behavior. Sensitivity studies were carried out to understand the importance of the individual input parameters for the simulation of polarimetric radar quantities from ice particles. The sensitivity studies showed that reflectivity only depends on the dielectric constant and the particle size distribution of the hydrometeors determining the intensity of the precipitation. The polarimetric quantities  $L_{DR}$  and  $Z_{DR}$  are independent of the intensity but are very sensitive to the dielectric constant and the microphysical characteristics of the ice hydrometeor type. The results of the sensitivity study were used to derive the free parameters accordingly to the assumptions of the NWP model such that the resulting synthetic polarimetric quantities matched the thresholds of the hydrometeor classification scheme by Höller et al. (1994). This derivation of the free parameters, the axis ratio and the maximum canting angle, was fundamental to bridge the gap between the information content of the microphysical parameterization schemes and the polarimetric quantities allowing SynPolRad to be applied to the forecasts of the NWP model.

In the development of SynPolRad, special care has been given to the assumptions regarding the representation of brightband signatures. In the brightband,  $L_{DR}$  values as high as  $-15$  dB are observed due to the enhanced polarimetric signatures of melting snow (e.g. Hagen et al. (1993)). This value was taken as a threshold to determine the free parameters for melting snow in order to reproduce the observed signatures.

SynPolRad was applied to two case studies to demonstrate the potential of the new method. A stratiform and a convective case study were chosen to assess the ability of mesoscale models to represent precipitation in different dynamical regimes. The evaluation concentrated on the representation of life cycle, intensity, and the spatial distribution of synthetic reflectivity,  $L_{DR}$ , and  $Z_{DR}$  as well as the hydrometeor type derived from the polarimetric quantities employing a classification scheme.

Already in the stratiform case study major discrepancies were found between the synthetic and the observed radar quantities. These were not expected to that extent because of the relatively simple microphysical processes involved in stratiform precipitation formation. In general, the LMK microphysical parameterization schemes underestimated reflectivity in snow and rain while strongly overpredicting the brightband signatures. The Thompson scheme overestimated the intensities in rain and snow, but reproduced best the brightband signatures. The strong overprediction of reflectivities in rain by the Thompson scheme was found to result from enhanced precipitation mixing ratios of rain, snow, and cloud ice content. The discrepancies between the different microphysical parameterization schemes and the observations were related to the assumptions regarding the particle spectrum, the ice density, and the resulting terminal falling velocity.

Regarding the convective case study, the models were able to reproduce a comparable event but the life cycle and especially the decay of the storm were not captured by the different model versions. In the simulations with the 2 component scheme, the convective core could only be distinguished by the enhanced precipitation in rain while the reflectivities in the ice phase were equally distributed in the convective and stratiform part of the storm. The introduction of a graupel phase in the 3 component scheme significantly enhanced the performance of the LMK simulating more realistic distributions of reflectivities but still with large discrepancies to the observations. The Thompson scheme reproduced best the distribution

of reflectivity and hydrometeor types with a clear distinction between the convective and the stratiform part of the storm. In the LMK as well as in the MesoNH simulations, the ice phase was dominated by graupel and almost no snow signatures appeared. The simulations of the MesoNH including a hail class showed improved reflectivities in the convection. Nevertheless, no microphysical parameterization scheme was able to reproduce the observed hail signatures in the convective core reaching the ground before melting. The evolution of the thermodynamical stratification was not captured by the models, all of which simulated an increase of the height of the 0° C isotherm in contrast to the observed decrease. However, this effect may also depend on the boundary conditions.

The different microphysical parameterization schemes had major problems to reproduce the microphysical characteristics of a convective precipitation event. This is especially true for the distinction between the convective and the stratiform part of the storm which has been shown in reflectivity as well as in the distribution of hydrometeor types. Furthermore, a better distinction between the graupel and snow phase is needed and heavier ice hydrometeor types have to be introduced in order to reproduce the typical hail signatures in the convective core. As the problems regarding the representation of convection are so evident and can be related to the lack of heavier ice hydrometeors, in this case, similar results would be expected for other cases. However, a long term evaluation of the model is desirable to confirm the results from both case studies and identify systematic errors in the microphysical parameterization schemes. This can also be helpful to distinguish between errors due to the representation of physical processes in the model and the errors resulting from the initial and boundary conditions.

The evaluation based on polarimetric quantities and the hydrometeor classification demonstrated for the two case studies that the differences in the simulated precipitation structures were due to the number of assumed hydrometeors and their microphysical characteristics. This was possible because of the combined information content of the polarimetric quantities and reflectivities. The polarimetric signatures together with the hydrometeor classification allowed to trace the ambiguities in the simulated reflectivity fields back to the assumed hydrometeors types and the related formulations of the PSD, density, and terminal falling velocity. The importance of the microphysical parameterization schemes for quantitative precipitation forecasts was demonstrated for the two case studies where the accumulated precipitation only varied with the parameterization scheme but not with the model version of the LMK.

The results from the case studies showed further that future model development and evaluation studies should focus stronger on the ice phase and also consider cloud water and cloud ice. However, for a full evaluation of the representation of cloud and precipitation processes polarimetric radar alone is not enough. The extension of SynPolRad to also simulate cloud radar observations would be a step towards a more complete picture of the model skill. Furthermore, the combination with information derived from satellites, radiometers, or GPS would be desirable. The evaluation has to be completed employing rain gauge measurements to assess the total precipitation at the ground. In other studies, the ability of the MM5 to simulate non precipitating ice clouds was successfully assessed combining simulated and measured lidar and radar profiles (Chiriaco et al. (2006)). For future model evaluations synergy effects resulting from the combination of different observation techniques should be utilized to describe the actual state of the atmosphere as good as possible before assessing

the model skill.

Apart from the number of ice hydrometeors, the parameter responsible for most of the discrepancies in the reflectivities was the formulation of the particle spectrum. This result confirms that for a realistic prediction of precipitation intensity, the DSD has to be described as accurately as possible and that one prognostic parameter is not sufficient to achieve the necessary accuracy. With two-moment schemes (e.g. Ferrier (1994)) explicitly considering the intercept parameter  $N_o$  of the exponential distribution as second prognostic variable or three-moment schemes (Milbrandt and Yau (2005)) also predicting the spectral shape parameter of the Gamma-Distribution, new concepts for a better representation of DSD have been successfully tested in research applications and should become available for operational use.

Besides the particle spectrum, the second parameter defining the microphysical characteristics of the hydrometeor type is the density. Both determine the falling velocity of the hydrometeors and, therefore, the time to interact with the system. This was shown in the stratiform case study to have a major impact on the precipitation intensity. In the convective case study, the importance of the assumptions regarding the ice density was demonstrated examining the spatial distribution of hydrometeor types. First, explaining the missing distinction between snow and graupel in the LMK and the MesoNH schemes where the graupel phase dominated because of its microphysical characteristics being too similar to snow. Second, discussing the lack of heavier ice hydrometeors reaching the ground before melting within the convective core. These results suggest that the description of precipitation processes in the model can be significantly improved introducing a more realistic or even prognostic ice density. This would also allow for a better distinction and a smoother transition between the different ice hydrometeor types. Even more potential would be found in a prognostic dielectric constant which could be attained by explicitly predicting the density and the melting degree of the ice hydrometeor. Combining a prognostic dielectric constant together with an improved formulation of the particle spectrum would also facilitate an explicit assimilation of reflectivity.

In recent years, new microphysical parameterization schemes have been developed increasing the number of bulk hydrometeor types. However, the results of this thesis suggest more potential in developing new concepts of microphysical parameterization schemes that are more closely related to or even explicitly predict relevant radar quantities. Formulating the microphysical processes in terms of observed variables will automatically establish a direct relationship between the model and the remote sensor and will be the first step towards a future assimilation of polarimetric radar data.

For future parameterization schemes, the concept of double-moment normalization schemes to describe the DSD should be of major interest. Lee et al. (2004) showed that using this normalization method any rain spectrum can be collapsed onto a unique normalized DSD which can then be described by just two independent moments of the DSD. Introducing this concept into NWP models, the microphysical processes in the model can then be formulated as a function of the two prognostic moments (Szyrmer et al. (2005)). The advantage of this

method is that the intercept parameters  $N_o$  which is of little physical meaning (describing the number of drops with a diameter equal to zero) is not used any more. Furthermore, polarimetric radar systems are able to observe two moments of the DSD of rain (e.g. using radar reflectivity and  $Z_{DR}$  or  $K_{dp}$ ) which determine the DSD of rain to a high degree of accuracy and can be directly assimilated into NWP models. In the ice phase, the polarimetric radar quantities are not directly related to the particle spectrum because no clear relationship between the shape of the particles and the diameter exists as in the case of rain. Here, most potential should be in the assimilation of reflectivity and the information about the hydrometeor type derived from classification schemes.

Concluding the results, the representation of ice phase hydrometeors and microphysical processes has been identified as one key parameter for a correct prediction of the precipitation at the ground. However, within this thesis a general problem regarding the understanding of the ice phase in theory, observation, and modeling has been found. Most of the publications studying the microphysical characteristics of ice phase hydrometeors are based on only a small number of observations that can not be representative for the natural variability. New observation methods have to be developed and the information content of different sensors has to be combined to derive more information about the microphysical properties of ice phase hydrometeors. Furthermore, more studies concentrating on the theoretical description of ice microphysics are needed to allow for a better representation of ice hydrometeors in the NWP models and provide necessary information for the development of retrieval algorithms on the observational side.

Within this thesis, the polarimetric radar forward operator SynPolRad has been developed for model evaluation purposes and its potential was proven evaluating two cases. Regarding future evaluations, SynPolRad can be applied for case studies as well as long term evaluations in order to identify systematic model errors. As the discussion of assimilation of polarimetric radar data showed, a forward operator is closely related to both, verification and initialization of NWP models. Therefore, SynPolRad can be further developed to be used as a test bed for polarimetric radar assimilation studies. Moreover, any formulation of the particle spectrum can be easily implemented into SynPolRad providing, therefore, the means for testing and developing future microphysical parameterization schemes. In the context of nowcasting or very short term weather prediction, SynPolRad can be employed to evaluate the actual model skill which can also be used for the best member selection in probabilistic prediction systems. SynPolRad provides a virtual tool to study and better understand sensitivities of polarimetric radar observations. Last but not least, SynPolRad can be extended to simulate synthetic signatures from model forecasts for radar systems on board of aircraft or satellites (e.g. TRMM, EARTHCARE (Ingmann (2004)), GPM).

# Appendix A

## Technical Specifications of POLDIRAD

Frequency [GHz]	5.5027
Wavelength [cm]	5.45
Horiz./Vert. Beam-Width [°]	1
Transmitted Power [kW]	250
PRF [Hz]	160 – 1200
Pulse Width [ $\mu$ s]	0.5, 1, 2
Range Resolution [m]	Any multiple of 75
Minimum Detectable Signal [dBm]	–108, for 0.5 $\mu$ s Pulse Width
Antenna Diameter [m]	ca. 5
Antenna Gain [dB]	44.5
Sidelobe Level [dB]	< –32 (For Linear Polarization)
Polarizations	Variable (Linear, Circular, Elliptic)
Longitude	11° 16' 45"
Latitude	48° 05' 12"
Height above MSL [m]	600

# Appendix B

## The T-Matrix Method

The T-Matrix method was initially introduced by Waterman (1969) as a technique for computing electromagnetic scattering by single, homogeneous, arbitrarily shaped particles. Up to now, it has been further developed and employed to be one of the most powerful and widely used tools for rigorously computing electromagnetic scattering. In many applications it surpasses other frequently used techniques in terms of efficiency and size parameter range. Because of its high and readily controllable numerical accuracy, the T-Matrix method is one of a very few sources of benchmark results for scattering from particles of arbitrary shape (Mishchenko et al. (2002)).

Within the T-Matrix method, the scattered fields are related to the incident fields and the physical characteristics of the scatterer applying the extended boundary condition method introduced by Waterman (1969). In the following the basic concepts of the method will be discussed based on the publications by Mishchenko and Travis (1998) and Barber and Yeh (1975).

In the framework of the T-Matrix approach, the incident  $\mathbf{E}_i(\mathbf{R})$  and the scattered fields  $\mathbf{E}_s(\mathbf{R})$  are expanded in vector spherical functions  $\mathbf{M}_{mn}$  and  $\mathbf{N}_{mn}$  as follows:

$$\mathbf{E}^i(\mathbf{R}) = \sum_{n=1}^{n_{max}} \sum_{m=-n}^n [a_{mn} Rg\mathbf{M}_{mn}(k\mathbf{R}) + b_{mn} Rg\mathbf{N}_{mn}(k\mathbf{R})], \quad (\text{B.1})$$

$$\mathbf{E}^s(\mathbf{R}) = \sum_{n=1}^{n_{max}} \sum_{m=-n}^n [p_{mn} \mathbf{M}_{mn}(k\mathbf{R}) + q_{mn} \mathbf{N}_{mn}(k\mathbf{R})], \quad |\mathbf{R}| > r_o, \quad (\text{B.2})$$

where  $k = 2\pi/\lambda$  is the wave number and  $\mathbf{R}$  is the radius vector.  $r_o$  gives the radius of a circumscribing sphere of the scattering particle and the origin of the coordinate system is assumed to be inside the particle. The functions  $Rg\mathbf{M}_{mn}$  and  $Rg\mathbf{N}_{mn}$  are regular (finite) at the origin while the use of the outgoing functions  $\mathbf{M}_{mn}$  and  $\mathbf{N}_{mn}$  ensures that the scattered field satisfies the radiation condition at infinity (i. e. the transverse component of the scattered electric field decays at  $1/|\mathbf{R}|$  while the radial component decays faster (see Mishchenko et al. (2002)). Because of the linearity of the Maxwell equations, the scattered field coefficients  $p_{mn}$  and  $q_{mn}$  and the incident field coefficients  $a_{mn}$  and  $b_{mn}$  can be related by a transition matrix (or T-Matrix)  $\mathbf{T}$ :

$$p_{mn} = \sum_{n'=1}^{n_{max}} \sum_{m'=-n}^{n'} [T_{mnm'n'}^{11} a_{m'n'} + T_{mnm'n'}^{12} b_{m'n'}], \quad (\text{B.3})$$

$$q_{mn} = \sum_{n'=1}^{n_{max}} \sum_{m'=-n}^{n'} [T_{mnm'n'}^{21} a_{m'n'} + T_{mnm'n'}^{22} b_{m'n'}]. \quad (\text{B.4})$$

In a compact matrix notation, Equations B.3 and B.4 can be rewritten as (see Equation 3.4):

$$\begin{bmatrix} \mathbf{p} \\ \mathbf{q} \end{bmatrix} = \mathbf{T} \begin{bmatrix} \mathbf{a} \\ \mathbf{b} \end{bmatrix} = \begin{bmatrix} \mathbf{T}^{11} & \mathbf{T}^{12} \\ \mathbf{T}^{21} & \mathbf{T}^{22} \end{bmatrix} \begin{bmatrix} \mathbf{a} \\ \mathbf{b} \end{bmatrix}. \quad (\text{B.5})$$

This equation forms the basis of the T-Matrix approach. The expansion coefficients  $a$  and  $b$  of the incident wave can be easily calculated and the knowledge of the T-Matrix for a given scatterer allows the computation of the scattered field via Equations B.2–B.4. The elements of the T-Matrix are independent of the incident and scattered fields and only depend on the shape, size, and refractive index of the scattering particle as well as on its orientation with respect to the reference frame.

Waterman (1969) developed the extended boundary condition which still provides the basis for the standard computation of the T-Matrix. In this approach, the equivalent theorem is applied showing that the scattered fields can be understood as the result of a set of surface currents on the surface of the scattering particle. Then, the scattering problem can be divided into an external and an internal part.

In the internal problem, the fields within the scatterer are expanded into series of vector spherical harmonics with coefficients that have to be determined. Applying the boundary condition at the surface, a linear set of equations can be derived that relates the coefficients of the unknown internal field to the expansion coefficients of the incident field. In the external problem, the scattered fields are described by a set of equivalent electromagnetic currents on the surface of the scattering particle which are unknown. Employing the equivalent theorem again, it can be shown that these surface currents must cancel the incident field throughout the interior volume of the scatterer. This extinction principle relates the unknown surface currents to the known incident field.

Expanding the internal field in vector spherical functions gives:

$$\mathbf{E}^{\text{int}}(\mathbf{R}) = \sum_{n=1}^{n_{max}} \sum_{m=-n}^n [c_{mn} R g \mathbf{M}_{mn}(m_r k \mathbf{R}) + d_{mn} R g \mathbf{N}_{mn}(m_r k \mathbf{R})], \quad |\mathbf{R}| > r_o, \quad (\text{B.6})$$

where  $m_r$  is the refractive index of the particle relative to that of the surrounding medium. The relation between the expansion coefficients of the incident and internal fields is linear and is given by

$$\begin{bmatrix} \mathbf{a} \\ \mathbf{b} \end{bmatrix} = \begin{bmatrix} \mathbf{Q}^{11} & \mathbf{Q}^{12} \\ \mathbf{Q}^{21} & \mathbf{Q}^{22} \end{bmatrix} \begin{bmatrix} \mathbf{c} \\ \mathbf{d} \end{bmatrix}, \quad (\text{B.7})$$

where the elements of the matrix  $\mathbf{Q}$  are two-dimensional integrals which must be numerically evaluated over the particle surface and depend on the particle size, shape, refractive index, and orientation. The scattered field coefficients are expressed in the internal field coefficients as

$$\begin{bmatrix} \mathbf{p} \\ \mathbf{q} \end{bmatrix} = \begin{bmatrix} Rg\mathbf{Q}^{11} & Rg\mathbf{Q}^{12} \\ Rg\mathbf{Q}^{21} & Rg\mathbf{Q}^{22} \end{bmatrix} \begin{bmatrix} \mathbf{c} \\ \mathbf{d} \end{bmatrix}, \quad (\text{B.8})$$

where, again, the elements of the  $Rg\mathbf{Q}$  matrix are two-dimensional integrals over the particle surface. Using the boundary condition at the surface, and superimposing internal and external field representations, a T-Matrix can be generated which directly relates the scattered field to the known incident field. Comparing Equations B.7 and B.8 with Equation B.5, we finally derive

$$\mathbf{T} = -Rg\mathbf{Q}[\mathbf{Q}]^{-1}. \quad (\text{B.9})$$

In the case of rotationally symmetric particles and provided that the axis of particle symmetry coincides with the  $\mathbf{Z}$  axis of the reference frame, the formulas become much simpler. Then, all surface integrals reduce to single integrals over the polar angle, and the T-Matrix becomes diagonal with respect to the indices  $m$  and  $m'$ :

$$T_{mm'n'}^{ij} = \delta_{mm'} T_{mmn}^{ij}. \quad (\text{B.10})$$

This allows to calculate each  $m$ th submatrix of the T-Matrix separately.

For the numerical calculations, the T-Matrix must be truncated to a finite size although, in theory, its size is infinite ( $n_{max} = \infty$ ). The convergence size of the T-Matrix is determined by increasing  $n_{max}$  in unit steps until the optical cross sections and the expansion coefficients converge within some specified accuracy. Problems can arise in the calculation of the inverse matrix  $\mathbf{Q}^{-1}$  because different elements of the matrix  $\mathbf{Q}$  can differ by many orders of magnitude. Even small numerical errors in the computed elements of the matrix  $\mathbf{Q}$  may result in large errors in the elements of the inverse matrix  $\mathbf{Q}^{-1}$ . The round off errors become increasingly significant with increasing particle size and/or highly aspherical particles, for which T-Matrix computations can become poorly convergent or even divergent.

# Appendix C

## SynPolRad Parameters

### C.1 LMK

	Rain	Snow	Graupel
$N(D)$	$N_o \exp(-\lambda D)$		
$N_o$ [mm <sup>-1</sup> m <sup>-3</sup> ]	8000	800	4000
$\lambda$	$\left(\frac{\pi \rho_w N_o}{\rho q_r}\right)^{1/4}$	$\left(\frac{\pi \rho_s N_o}{\rho q_s}\right)^{1/3}$	$\left(\frac{\pi \rho_g N_o}{\rho q_g}\right)^{1/4}$
Axis Ratio	$f(D)$	0.3	0.5
Maximum Canting angle	10°	20°	40°
$\Delta\vartheta$	5°	10°	20°
Brightband			
Water portion [%]		36	36
Maximum canting angle		60°	60°
$\Delta\vartheta$		45°	40°

**Table C.1:** SynPolRad input parameters for the computation of synthetic polarimetric quantities from the LMK microphysical schemes.

## C. 2 Thompson Scheme

	Rain	Snow	Graupel
$N(D)$	$N_o \exp(-\lambda D)$		$N_o^g D \exp(-\lambda D)$
$N_o$ [ $\text{mm}^{-1} \text{m}^{-3}$ ]	$f(q_r)$	$f(T)$	$f(q_g)$
$\lambda$	$\left(\frac{\pi \rho_w N_o}{\rho q_r}\right)^{1/4}$	$\left(\frac{\pi \rho_s N_o}{\rho q_s}\right)^{1/4}$	$1.32 \left(\frac{\pi \rho_g N_o}{\rho q_g}\right)^{0.2}$
Axis Ratio	$f(D)$	0.3	0.7
Maximum Canting angle	10°	10°	40°
$\Delta\vartheta$	5°	5°	20°
Brightband			
Water portion [%]		36	36
Maximum canting angle		60°	60°
$\Delta\vartheta$		45°	40°

**Table C.2:** SynPolRad input parameters for the computation of synthetic polarimetric quantities from the Thompson microphysical scheme.

## C. 3 MesoNH

	Rain	Snow	Graupel	Hail
$N(D)$	$C \lambda^{x+1} \exp(-\lambda D)$			
$N_o$ [ $\text{mm}^{-1} \text{m}^{-3}$ ]	$N_o = C \lambda^x$			
$\lambda$	$\lambda_x = \left(\frac{\rho q_x}{a C G(b)}\right)^{\frac{1}{x-b}}$			
Axis Ratio	$f(D)$	0.3	0.6	1.8
Maximum Canting angle	10°	20°	60°	90°
$\Delta\vartheta$	5°	10°	30°	45°
Water portion [%]			0.14	0.81
Brightband				
Water portion [%]		19	81	90
Maximum canting angle		50°	60°	90°
$\Delta\vartheta$		35°	40°	45°

**Table C.3:** SynPolRad input parameters for the computation of synthetic polarimetric quantities from the MesoNH microphysical scheme. The constants for the specific hydrometeor types can be found in Chapter 2, Table 2.3.

# Symbols

$A_{dp}$	Specific Differential Attenuation
$a_m$	Form Factor in the Mass–Size Relationship
$a_{mn}$	Field Coefficients
$a_p$	Coefficients of the Moments of the DSD
$b_{mn}$	Field Coefficients
$C$	Radar Constant
$c$	Speed of Light
$D$	Diameter
$D_o$	Median Diameter
$d$	Diameter of the Antenna
$E^i$	Incident Wave
$E^s$	Scattered Wave
$\mathbf{e}$	Unit Vector
$e$	Vapor Pressure
$f$	Volume of Intrusions
$G$	Antenna Gain
$H$	Horizontal
$H$	Height of the Radar Beam
$h$	Transmitted Pulse Length
$i$	Imaginary Part
$K$	Complex Dielectric Constant
$K_{dp}$	Specific Differential Phase
$k$	Specific Attenuation
$L_{DR}$	Linear Depolarization Ratio
$m$	Mass
$m$	Complex Refractive Index
$\mathbf{N}$	Symmetry Axis
$N$	Refractivity
$N$	Number Concentration
$N_o$	Intercept Parameter
$n$	Ordinary Refractive Index
$P$	Rainfall Parameters
$\overline{P}_r$	Mean Received Power
$P_t$	Transmitted Power

$p$	Pressure
$p$	Moments of the DSD
$p_{mn}$	Field Coefficients
$p(\vartheta)$	Distribution of Canting Angles
$q$	Hydrometeor Mixing Ratio
$q_{mn}$	Field Coefficients
<b>R</b>	Rotation Matrix
$R$	Rain Rate
$R$	Earth Radius
$R'$	Effective Radius
$r$	Range
<b>S</b>	Scattering Matrix
<b>T</b>	T-Matrix
$T$	Temperature
$V$	Vertical
$V$	Volume
<b>X</b>	X Axis
$x$	Hydrometeor Type
<b>Y</b>	Y Axis
<b>Z</b>	Z Axis
$Z$	Reflectivity
$Z_{DR}$	Differential Reflectivity
$z$	Reflectivity Factor
$\alpha$	Axis Ratio
$\beta$	Form Factor of Intrusions
$\Gamma$	Gamma Function
$\Delta$	Increment
$\Theta$	Beam Width
$\vartheta$	Canting Angle
$\bar{\vartheta}$	Mean Canting Angle
$\lambda$	Wavelength
$\lambda$	Slope of the Marshall Palmer Distribution
$\nu$	Speed of Light in a Medium
$\rho$	Density
$\rho_{HV}(0)$	Cross Correlation between Horizontal and Vertical Polarization
$\sigma$	Backscatter Cross-Section
$\tau$	Pulse Duration
$\Phi$	Beam Width
$\Phi_{dp}$	Differential Phase Shift
$\Psi$	Radar Elevation Angle

# Abbreviations and Acronyms

Anaprop	Anomalous Propagation
AROME	Application of Research to Operations in MesoscaleE
CASA	Collaborative Adaptive Sensing of the Atmosphere
CAPPI	Constant Altitude PPI
CCN	Cloud Condensation Nucleus
dB	Decibel
dBZ	Decibels relative to a Reflectivity of 1 mm <sup>6</sup> m <sup>3</sup>
DLR	Deutsches Zentrum für Luft- und Raumfahrt
DSD	Drop Size Distribution
DWD	Deutscher Wetterdienst
GME	Global Modell
<i>L<sub>DR</sub></i>	Linear Depolarization Ratio
LM	Lokal Modell
LMK	Lokal Modell Kürzestfrist
MesoNH	Mesoscale Non-Hydrostatic Model
MM5	PSU/NCAR Mesoscale Model
NCAR	National Center of Atmospheric Research
NWP	Numerical Weather Prediction
POLDIRAD	Polarimetric Diversity Doppler Radar
PPI	Plan Position Indicator
PSD	Particle Size Distribution
PSU	Pennsylvania State University
QPF	Quantitative Precipitation Forecast
RHI	Range Height Indicator
RSM	RadarSimulationsModell
SynPolRad	Synthetic Polarimetric Radar
TRMM	Tropical Rainfall Measuring Mission
WRF	Weather Research and Forecasting Model
<i>Z<sub>DR</sub></i>	Differential Reflectivity

# Bibliography

- Anagnostou, E. N. and W. F. Krajewski, 1997: Simulation of radar reflectivity fields: Algorithm formulation and evaluation. *Water Resources Research*, **33**, 1419–1428. 28, 29
- Andsager, K., K. V. Beard, and N. F. Laird, 1999: Laboratory measurements of axis ratios for large raindrops. *Journal of the Atmospheric Sciences*, **56**, 2673–2683. 8, 42
- Atlas, D., 1953: Optical extinction by rainfall. *Journal of Meteorology*, **10**, 486–488. 9
- Aydin, K., T. A. Seliga, and V. Balaji, 1986: Remote sensing of hail with a dual linear polarization radar. *Journal of Climate and Applied Meteorology*, **25**, 1475–1484. 24
- Balakrishnan, N. and D. S. Zrnica, 1990a: Estimation of rain and hail rates in mixed-phase precipitation. *Journal of the Atmospheric Sciences*, **47**, 565–583. 24
- 1990b: Use of polarization to characterize precipitation and discriminate large hail. *Journal of the Atmospheric Sciences*, **47**, 1525–1540. 25
- Baldini, L., E. Gorgucci, and V. Chandrasekar, 2004: Hydrometeor classification methodology for C-band polarimetric radars. *Proceedings of ERAD*, volume 2, 62–66. 25
- Barber, P. and C. Yeh, 1975: Scattering of electromagnetic waves by arbitrarily shaped dielectric bodies. *Applied Optics*, **14**, 2864–2872. 28, 110
- Barthazy, E. and R. Schefold, 2004: Properties of snowflakes of different riming degree and crystal types. *Preprints, 14th International Conference on Clouds and Precipitation, ICCP, 19-23 July 2004*, 715–718. 11, 12
- Battan, L. J., 1973: *Radar observation of the atmosphere*. The University of Chicago Press. 20, 21, 38
- Bean, B. and E. Dutton, 1968: *Radio meteorology*. Dover Publications, Inc.. 36
- Beard, K. V. and C. Chuang, 1987: A new model for the equilibrium shape of raindrops. *Journal of the Atmospheric Sciences*, **44**, 1509–1524. 8
- Beard, K. V. and A. R. Jameson, 1983: Raindrop canting. *Journal of the Atmospheric Sciences*, **40**, 448–454. 9
- Bech, J., A. Sairouni, B. Codina, J. Lorente, and D. Bebbington, 2000: Weather radar anaprop conditions at a Mediterranean coastal site. *Physics and Chemistry of the Earth (B)*, **25**, 829–832. 36, 37

- Bohren, C. F. and L. J. Battan, 1982: Radar backscattering of microwaves by spongy ice spheres. *Journal of the Atmospheric Sciences*, **39**, 2623–2628. 35
- Bouttier, F., 2005: Overview of Meteo–France NWP plans and AROME project. *15th Aladin workshop, Bratislava, 6-10 June 2005*. 2, 18
- Brandes, E. A., J. Vivekanandan, J. D. Tuttle, and C. J. Kessinger, 1995: A study of thunderstorm microphysics with multiparameter radar and aircraft observations. *Monthly Weather Review*, **123**, 3129–3143. 25
- Brandes, E. A., G. Zhang, and J. Sun, 2006: On the influence of assumed drop size distribution form on radar-retrieved thunderstorm microphysics. *Journal of Applied Meteorology and Climatology*, **45**, 259–268. 2, 3, 4
- Bringi, V. N., D. Brunkow, V. Chandrasekar, S. Ruthledge, P. Kennedy, and A. Mudukutore, 1993: Polarimetric measurements in Colorado convective storms using the CSU-CHILL radar. *Preprints, 26th Int. Conf. on Radar Meteorology, Norman, OK*, American Meteorological Society, 519–521. 24
- Bringi, V. N. and V. Chandrasekar, 2001: *Polarimetric Doppler Weather Radar*. Number ISBN 0 5 21 623847, Cambridge University Press. 23, 24, 39
- Bringi, V. N., R. M. Rasmussen, and J. Vivekanandan, 1986: Multiparameter radar measurements in Colorado convective storms. Part I: Graupel melting studies. *Journal of the Atmospheric Sciences*, **43**, 2545–2563. 25, 28, 30, 104
- Caniaux, G., J.-L. Redelsperger, and J.-P. Lafore, 1994: A numerical study of the stratiform region of a fast-moving squall line. Part I: General description and water and heat budgets. *Journal of the Atmospheric Sciences*, **51**, 2046–2074. 18, 19
- Capsoni, C., M. D’Amico, and R. Nebuloni, 2001: A multiparameter polarimetric radar simulator. *Journal of Atmospheric and Oceanic Technology*, **18**, 1799–1809. 28, 29
- Caumont, O., V. Ducrocq, G. Delrieu, M. Gosset, J.-P. Pinty, J. P. du Chatelet, H. Andrieu, Y. Lemaitre, and G. Scialom, 2006: A radar simulator for high-resolution nonhydrostatic models. *Journal of Atmospheric and Oceanic Technology*, **23**, 1049–1067. 3, 28, 30
- Chandrasekar, V. and V. N. Bringi, 1987: Simulation of radar reflectivity and surface measurements of rainfall. *Journal of Atmospheric and Oceanic Technology*, **4**, 464–478. 4, 28
- Chandrasekar, V., W. A. Cooper, and V. N. Bringi, 1988: Axis ratios and oscillations of raindrops. *Journal of the Atmospheric Sciences*, **45**, 1323–1333. 8, 9, 42
- Cheng, L. and M. English, 1983: A relationship between hailstone concentration and size. *Journal of the Atmospheric Sciences*, **40**, 204–213. 12, 43
- Cheng, L., M. English, and R. Wong, 1985: Hailstone size distributions and their relationship to storm thermodynamics. *Journal of Climate and Applied Meteorology*, **24**, 1059–1067. 11

- Chevallier, F. and P. Bauer, 2003: Model rain and clouds over oceans: Comparison with SSM/I observations. *Monthly Weather Review*, **131**, 1240–1255. 3, 28
- Chiriaco, M., R. Vautard, H. Chepfer, M. Haeffelin, J. Dudhia, Y. Wanherdrick, Y. Morille, and A. Protat, 2006: The ability of MM5 to simulate ice clouds: Systematic comparison between simulated and measured fluxes and lidar/radar profiles at the SIRTA atmospheric observatory. *Monthly Weather Review*, **134**, 897–918. 106
- Chuang, C. H. and K. V. Beard, 1990: A numerical model for the shape of electrified raindrops. *Journal of the Atmospheric Sciences*, **47**, 1374–1389. 8
- Colle, B. A., M. F. Garvert, J. B. Wolfe, C. F. Mass, and C. P. Woods, 2005: The 13–14 December 2001 IMPROVE-2 event. Part III: Simulated microphysical budgets and sensitivity studies. *Journal of the Atmospheric Sciences*, **62**, 3535–3558. 2
- Cremonini, R., R. Bechini, P. P. Alberoni, and M. Celano, 2004: Which hydrometeor classification scheme is realistic using ZH, ZDR and temperature in complex orography? A study based on operational C-band polarimetric weather radar in northern Italy. *Proceedings of ERAD*, volume 2, 393–397. 25
- Dölling, I., 1997: *Modellrechnungen für polarimetrische Radarparameter im C-Band für Ensembles taumelnder und schmelzender Eispartikeln und Vergleich mit Messungen*. Ph.D. thesis, DLR Institut für Physik der Atmosphäre. 4, 28, 52
- Doms, G. and J. Förstner, 2004: Development of a kilometer-scale NWP-system: LMK. *COSMO Newsletter*, 159–167. 2
- Doms, G. and U. Schättler, 1999: *The nonhydrostatic limited-area model LM (Lokalmodell) of DWD. Part I: Scientific documentation*. German Weather Service (DWD). 14, 16, 48
- Dotzek, N., H. Höller, C. Thery, and T. Fehr, 2001: Lightning evolution related to radar-derived microphysics in the 21 July 1998 EULINOX supercell storm. *Atmospheric Research*, **56**, 335–354. 20
- Doviak, R. J. and D. S. Zrnic, 1984: *Doppler radar and weather observations*. Academic Press, Inc. 20, 37, 38
- Droegemeier, K. K., J. D. Smith, S. Businger, and C. Doswell, 2000: Hydrological aspects of weather prediction and flood warnings: Report on the ninth prospectus development team of the U.S. Weather Research Program. *Bulletin of the American Meteorological Society*, **81**, 2665–2680. 1, 3
- Ebert, E. E., U. Damrath, W. Wergen, and M. E. Baldwin, 2003: The WGNE assessment of short-term quantitative precipitation forecast. *Bulletin of the American Meteorological Society*, 481–492. 1
- Fabry, F. and W. Szyrmer, 1999: Modeling of the melting layer: Part II: Electromagnetic. *Journal of the Atmospheric Sciences*, **56**, 3593–3600. 35, 50
- Feingold, G. and Z. Levin, 1986: The lognormal fit to raindrop spectra from frontal convective clouds in Israel. *Journal of Climate and Applied Meteorology*, **25**, 1346–1363. 9

- Ferrier, B. S., 1994: A double-moment multiple-phase four-class bulk ice scheme. Part I: Description. *Journal of the Atmospheric Sciences*, **51**, 249–280. 14, 107
- Ferrier, B. S., W. K. Tao, and J. Simpson, 1995: A double-moment multiple-phase four-class bulk ice scheme. Part II: Simulations of convective storms in different large-scale environments and comparisons with other bulk parameterizations. *Journal of the Atmospheric Sciences*, **52**, 1001–1033. 2
- Friedrich, K., U. Germann, J. J. Gourley, and P. Tabary, 2006: Effects of radar beam shielding on rainfall estimation for polarimetric C-band radar. *Submitted to J. Atmos. Oceanic. Technology*. 2
- Fritsch, J. M., R. A. H. Jr., R. Adler, H. Bluestein, L. Bosart, J. Brown, F. Carr, C. Davis, R. H. Johnson, N. Junker, Y.-H. Kuo, S. Rutledge, J. Smith, Z. Toth, J. W. Wilson, E. Zipser, and D. Zrnica, 1998: Quantitative precipitation forecasting: Report of the eighth prospectus development team, U.S. Weather Research Program. *Bulletin of the American Meteorological Society*, **79**, 285–299. 1, 3
- Fujiyoshi, Y., 1986: Melting snowflakes. *Journal of the Atmospheric Sciences*, **43**, 307–311. 50
- Garvert, M. F., C. P. Woods, B. A. Colle, C. F. Mass, P. V. Hobbs, M. T. Stoelinga, and J. B. Wolfe, 2005: The 13-14 December 2001 IMPROVE-2 event. Part II: Comparison of MM5 model simulations of clouds and precipitation with observations. *Journal of the Atmospheric Sciences*, **62**, 3520–3534. 2
- Gilmore, M. S., J. M. Straka, and E. N. Rasmussen, 2004: Precipitation uncertainty due to variations in precipitation particle parameters within a simple microphysics scheme. *Monthly Weather Review*, **132**, 2610–2627. 2
- Gourley, J. J., P. Tabary, and J. P. du Chatelet, 2006: Data quality of the Meteo France C-band polarimetric radar. *Journal of Atmospheric and Oceanic Technology*, **23**, 1340–1356. 2
- Green, A. W., 1975: An approximation for the shapes of large raindrops. *Journal of Applied Meteorology*, **14**, 1578–1583. 8
- Grell, G. A., J. Dudhia, and D. R. Stauffer, 1994: A description of the fifth-generation Penn State/NCAR Mesoscale model (MM5). Technical Report NCAR/TN-389+IA, National Center for Atmospheric Research. 17
- Gunn, K. L. S. and J. S. Marshall, 1957: The distribution with size of aggregate snowflakes. *Journal of Meteorology*, **15**, 452–461. 11
- Haase, G., 1998: *Simulation von Radarmessungen mit Daten des Lokalmodells*. Master's thesis, Meteorologisches Institut der Rheinischen Friedrich-Willhelms-Universität Bonn. 52
- Haase, G. and S. Crewell, 2000: Simulation of radar reflectivities using a mesoscale weather forecast model. *Water Resources Research*, **36**, 2221–2231. 3, 28, 30, 38, 52, 104

- Hagen, M., H. Höller, and P. F. Meischner, 1994: *Cost 75: Weather Radar systems*, European Commission, chapter Multiparameter radar characterization of precipitation particles with in situ measurements. Number ISSN 1018-5593. 26
- Hagen, M., J. Hubbert, C. Richter, V. N. Bringi, and P. Meischner, 1993: Bright band observations with radar and aircraft. *26th International Conference on Radar Meteorology, Norman*, American Meteorological Society, 304–305. 49, 105
- Heymsfield, A. J., 1978: The characteristics of graupel particles in northeastern Colorado cumulus congestus clouds. *Journal of the Atmospheric Sciences*, **35**, 284–295. 11, 12
- Heymsfield, A. J. and M. Kajikawa, 1987: An improved approach to calculating terminal velocities of plate-like crystals and graupel. *Journal of the Atmospheric Sciences*, **44**, 1088–1099. 17
- Höller, H., V. Bringi, J. Hubbert, M. Hagen, and P. F. Meischner, 1994: Life cycle and precipitation formation in a hybrid-type hailstorm revealed by polarimetric and Doppler radar measurements. *Journal of the Atmospheric Sciences*, **51**, 2500–2522. 2, 20, 25, 26, 46, 105
- Holt, A. R., 1984: The scattering of electromagnetic waves by single hydrometeors. *Radio Science*, **17**, 929–965. 33
- Huang, G. J., J. C. Hubbert, and V. N. Bringi, 2001: Precipitation canting angle distribution estimation from covariance matrix analysis of CSU-CHILL radar data. *30th International Conference on Radar Meteorology, Munich, Germany*, 651–653. 9
- Illingworth, A., 2004: *Weather Radar*, P. F. Meischner, chapter Polarimetric Measurements. 130 – 166. 24
- Ingmann, P., 2004: EarthCARE-earth, clouds, aerosols and radiation explorer. Reports for mission selection SP-1279(1), European Space Agency. 108
- Jameson, A. R., 1983: Microphysical interpretation of multi-parameter radar measurements in rain. Part I: Interpretation of polarization measurements and estimation of raindrop shapes. *Journal of the Atmospheric Sciences*, **40**, 1792–1802. 23
- Jung, Y., M. Xue, and J. M. Straka, 2005: Assimilation of polarimetric radar data using ensemble Kalman filter: Experiment with simulated data. *AMS 21st Conference on Weather analysis and forecasting/ 17th Conference on numerical weather prediction, Washington, DC*. 3, 4
- Keenan, T., 2003: Hydrometeor classification with a C-band polarimetric radar. *Australian Meteorological Magazine*, 871–886. 25
- Keil, C., 2000: *Numerische Simulation von Starkniederschlagsereignissen mit mesoskaligen Wettervorhersagemodellen*. Ph.D. thesis, DLR Institut für Physik der Atmosphäre. 2
- Keil, C., A. Tafferner, and H. Mannstein, 2003: Evaluating high-resolution model forecasts of European winter storms by use of satellite and radar observations. *Weather and Forecasting*, **18**, 732–747. 2, 3

- Keil, C., A. Tafferer, and T. Reinhardt, 2006: Synthetic satellite imagery in the Lokal-Modell. *Atmospheric Research*, **82**, 19–25. 70
- Kessler, E., 1969: *On the distribution and continuity of water substance in atmospheric circulations*. Number 32 in Meteor. Monogr., Amer. Meteor. Soc., 84 pp. pp. 14
- Klaassen, W., 1988: Radar observations and simulations of the melting layer of precipitation. *Journal of the Atmospheric Sciences*, **45**, 3741–3753. 50
- Knight, C. A. and N. C. Knight, 1970: The falling behavior of hailstones. *Journal of the Atmospheric Sciences*, **27**, 672–681. 12
- Knight, N. C., 1986: Hailstone shape factor and its relation to radar interpretation of hail. *Journal of Climate and Applied Meteorology*, **25**, 1956–1958. 12
- Lafore, J. P., 1998: The Meso-NH atmospheric simulation system. Part I: Adiabatic formulation and control simulations. *Annales Geophysicae*, **16**, 90–109. 18
- Lee, G. W. and I. Zawadzki, 2005: Variability of drop size distributions: Time-scale dependence of the variability and its effects on rain estimation. *Journal of Applied Meteorology*, **44**, 241–255. 9
- Lee, G. W., I. Zawadzki, W. Szyrmer, D. Sempere-Torres, and R. Uijlenhoet, 2004: A general approach to double-moment normalization of drop size distributions. *Journal of Applied Meteorology*, **43**, 264–281. 107
- Liebe, H. J., G. A. Hufford, and M. G. Cotton, 1993: Propagation modeling of moist air and suspended water/ice particles at frequencies below 1000 GHz. *AGARD 52nd Special Meeting of the Panel on Electromagnetic Wave Propagation, Palma de Mallorca, Spain*. 30, 38
- Lin, Y.-L., R. D. Farley, and H. D. Orville, 1983: Bulk parameterization of the snow field in a cloud model. *Journal of Climate and Applied Meteorology*, **22**, 1065–1092. 13, 14, 16, 18
- Liu, H. and V. Chandrasekar, 2000: Classification of hydrometeors based on polarimetric radar measurements: Development of fuzzy logic and neuro-fuzzy systems, and in situ verification. *Journal of Atmospheric and Oceanic Technology*, **17**, 140–164. 25, 26
- Locatelli, J. D. and P. V. Hobbs, 1974: Fall speeds and masses of solid precipitation particles. *Journal of Geophysical Research*, **79**, 2185–2197. 16
- Magono, S. C. and C. W. Lee, 1966: Meteorological classification of natural snow crystals. *J. Fac. Sci. Hokkaido Univ. Serv. VII*, **2**, 321–362. 10
- Marshall, J. and W. M. Palmer, 1948: The distribution of raindrops with size. *Journal of Meteorology*, **5**, 165–166. 9, 16, 64, 73
- Marzano, F. S., D. Scaranari, M. Celano, P. Alberoni, G. Vulpiani, and M. Montopoli, 2006: Hydrometeor classification from dual-polarized weather radar: Extending fuzzy logic from S-band to C-band data. *Advances in Geosciences*, **7**. 25

- Mason, B. J., 1994: The shapes of snow crystals - fitness for purpose? *The Quarterly Journal of the Royal Meteorological Society*, **120**, 849–860. 10
- Matrosov, S. Y., R. F. Reinking, R. A. Kropfli, and B. W. Bartram, 1996: Estimation of ice hydrometeor types and shapes from radar polarization measurements. *Journal of Atmospheric and Oceanic Technology*, **13**, 85–96. 35
- Matson, R. J. and A. W. Huggins, 1980: The direct measurement of the sizes, shapes and kinematics of falling hailstones. *Journal of the Atmospheric Sciences*, **37**, 1107–1125. 12
- Maxwell Garnet, J. C., 1904: Colours in metal glasses and in metallic films. *Philos. Trans. Roy. Soc. London*, **A 203**, 385–420. 35
- May, P. T. and T. D. Keenan, 2005: Evaluation of microphysical retrievals from polarimetric radar with wind profiler data. *Journal of Applied Meteorology*, **44**. 26
- Meetschen, D., S. Crewell, P. Gross, G. Haase, C. Simmer, and A. van Lammeren, 2000: Simulation of weather radar products from a mesoscale model. *Physics and Chemistry of the Earth. Part B: Hydrology, Oceans and Atmosphere*, **25**, 1257–1262. 30
- Meischner, P. F., V. N. Bringi, D. Heimann, and H. Höller, 1991: A squall line in southern Germany: Kinematics and precipitation formation as deduced by advanced polarimetric and Doppler radar measurements. *Monthly Weather Review*, **119**, 678–701. 20, 25
- Meischner, P. F., N. Dotzek, M. Hagen, and H. Höller, 2004: *Weather Radar*, P. F. Meischner, chapter Understanding Severe Weather Systems using Doppler and polarisation Radar. 2
- Milbrandt, J. A. and M. K. Yau, 2005: A multimoment bulk microphysics parameterization. Part I: Analysis of the role of the spectral shape parameter. *Journal of the Atmospheric Sciences*, **62**, 3051–3064. 107
- Mishchenko, M. I. and L. D. Travis, 1998: Capabilities and limitations of a current Fortran implementation of the T-matrix method for randomly oriented, rotationally symmetric scatterers. *Journal of Quantitative Spectroscopy and Radiative Transfer*, **60**, 309–324. 30, 110
- Mishchenko, M. I., L. D. Travis, and A. A. Lacis, 2002: *Scattering, Absorption, and Emission of Light by Small Particles*. Cambridge University Press. 110
- Oguchi, T., 1983: Electromagnetic wave propagation and scattering in rain and other hydrometeors. *Proc. IEEE*, **71**, 1029–1078. 39
- Olson, W. S., P. Bauer, N. F. Viltard, D. E. Johnson, W.-K. Tao, R. Meneghini, and L. Liao, 2001: A melting-layer model for passive/active microwave remote sensing applications. Part I: Model formulation and comparison with observations. *Journal of Applied Meteorology*, **40**, 1145–1163. 50
- Pfeifer, M., G. Craig, M. Hagen, and C. Keil, 2004: A polarimetric radar forward operator. *Proceedings of ERAD*, volume 2, 494–498. 29

- Pinty, J.-P., E. Richard, and P. Tabary, 2002: Fine scale simulations of the MAP-IOP2A precipitating system: Comparison with radar data and sensitivity to the hail category. *11th Conference on Cloud Physics*, volume 2, P.4.15. 18
- Pruppacher, H. R. and K. Beard, 1970: A wind tunnel investigation of the internal circulation and shape of water drops falling at terminal velocity in air. *The Quarterly Journal of the Royal Meteorological Society*, **96**, 247–256. 8
- Pruppacher, H. R. and J. D. Klett, 2003: *Microphysics of clouds and precipitation*. Kluwer Academic Publishers. 8, 9, 10, 11, 12, 43
- Rasmussen, R. M., I. Geresdi, G. Thompson, K. Manning, and E. Karplus, 2002: Freezing drizzle formation in stably stratified layer clouds: The role of radiative cooling of cloud droplets, cloud condensation nuclei, and ice initiation. *Journal of the Atmospheric Sciences*, **59**, 837–860. 13
- Ray, P. S., 1972: Broadband complex refractive indices of ice and water. *Applied Optics*, **11**, 1836–1844. 30, 34, 35, 42
- Reisner, J., R. M. Rasmussen, and R. T. Brintjes, 1998: Explicit forecasting of supercooled liquid water in winter storms using the MM5 mesoscale model. *Q. J. R. Meteorolog. Soc.*, **124**, 1071–1107. 17
- Rinehart, R. E., 2004: *Radar for meteorologists*. Rinehart publications. 37
- Rutledge, S. A. and P. V. Hobbs, 1984: The mesoscale and microscale structure and organization of clouds and precipitation in midlatitude cyclones. XII: A diagnostic modeling study of precipitation development in narrow cold-frontal rainbands. *Journal of the Atmospheric Sciences*, **41**, 2949–2972. 14, 17, 18
- Ryzhkov, A. V., T. J. Schuur, D. W. Burgess, P. L. Heinselman, S. E. Giangrande, and D. S. Zrnic, 2005: The joint polarization experiment: Polarimetric rainfall measurements and hydrometeor classification. *Bulletin of the American Meteorological Society*, 809–824. 2
- Schefold, R., B. Baschek, M. Wüst, and E. Barthazy, 2002: Fall velocity and axial ratio of snowflakes. *Proceedings of ERAD*, 84–89. 11
- Schroth, A. C., M. S. Chandra, and P. F. Meischner, 1988: A C-band coherent polarimetric radar for propagation and cloud physics research. *Journal of Atmospheric and Oceanic Technology*, **5**, 804–822. 4, 20, 24
- Sekhon, R. S. and R. C. Srivastava, 1970: Snow size spectra and radar reflectivity. *Journal of the Atmospheric Sciences*, **27**, 299–307. 11, 17
- 1971: Doppler radar observations of drop-size distributions in a thunderstorm. *Journal of the Atmospheric Sciences*, **28**, 983–994. 9
- Seliga, T. A. and V. N. Bringi, 1976: Potential use of radar differential reflectivity measurements at orthogonal polarizations for measuring precipitation. *Journal of Applied Meteorology*, **15**, 69–76. 23, 24

- Sempere-Torres, D., J. M. Porra, and J.-D. Creutin, 1994: A general formulation of raindrop size distribution. *Journal of Applied Meteorology*, **33**, 1494–1502. 9
- Skamarock, W. C., J. B. Klemp, J. Dudhia, D. O. Gill, D. M. Barker, W. Wang, and J. G. Powers, 2005: A description of the advanced research WRF Version 2. Technical Note NCAR/TN-468+STR, NCAR. 2
- Straka, J. M. and E. R. Mansell, 2005: A bulk microphysics parameterization with multiple ice precipitation categories. *Journal of Applied Meteorology*, **44**, 445–466. 14
- Straka, J. M., D. S. Zrnic, and A. V. Ryzhkov, 2000: Bulk hydrometeor classification and quantification using polarimetric radar data: Synthesis of relations. *Journal of Applied Meteorology*, **39**. 23, 24, 25, 26, 34, 42, 43
- Szyrmer, W., S. Laroche, and I. Zawadzki, 2005: A microphysical bulk formulation based on scaling normalization of the particle size distribution. Part I: Description. *Journal of the Atmospheric Sciences*, **62**, 4206–4221. 107
- Szyrmer, W. and I. Zawadzki, 1999: Modeling of the melting layer. Part I: Dynamics and microphysics. *Journal of the Atmospheric Sciences*, **56**, 3573–3592. 50
- Testud, J., S. Oury, R. A. Black, P. Amayenc, and X. Dou, 2001: The concept of “normalized” distribution to describe raindrop spectra: A tool for cloud physics and cloud remote sensing. *Journal of Applied Meteorology*, **40**, 1118–1140. 9
- Thompson, G., R. M. Rasmussen, and K. Manning, 2004: Explicit forecasts of winter precipitation using an improved bulk microphysics scheme. Part I: Description and sensitivity analysis. *Monthly Weather Review*, **132**, 519–542. 17
- Ulbrich, C. W., 1983: Natural variations in the analytical form of the raindrop size distribution. *Journal of Climate and Applied Meteorology*, **22**, 1764–1775. 9, 10
- Vivekanandan, J., 1986: *Multiparameter radar measurements in Colorado convective storms*. Ph.D. thesis, Colorado State University and NCAR. 31, 32, 33, 39, 48, 52
- Vivekanandan, J., V. N. Bringi, and R. Raghavan, 1990: Multiparameter radar modeling and observation of melting ice. *Journal of the Atmospheric Sciences*, **47**, 549–564. 4, 28
- Vivekanandan, J., R. Raghavan, and V. N. Bringi, 1993: Polarimetric radar modeling of mixtures of precipitation particles. *IEEE Transactions on Geoscience and Remote Sensing*, **31**, 1017–1030. 28
- Vivekanandan, J., D. S. Zrnic, S. M. Ellis, R. Oye, A. V. Ryzhkov, and J. Straka, 1999: Cloud microphysics retrieval using S-band dual-polarization radar measurements. *Bulletin of the American Meteorological Society*, **80**, 381–388. 2, 3, 25
- Walko, R. L., W. R. Cotton, M. P. Meyers, and J. Y. Harrington, 1995: New RAMS cloud microphysics parameterization Part I: The single-moment scheme. *Atmospheric Research*, **38**, 29–62. 14

- Warren, S. G., 1984: Optical constants of ice from the ultraviolet to the microwave. *Applied Optics*, **23**, 1206–1225. 30, 34, 35
- Waterman, P. C., 1969: Scattering by dielectric obstacles. *Alta Frequenza (Speciale)*, 348–352. 3, 28, 30, 110, 111
- Zawadzki, I., E. Monteiro, and F. Fabry, 1994: The development of drop size distributions in light rain. *Journal of the Atmospheric Sciences*, **51**, 1100–1113. 13
- Zhang, G., J. Sun, and E. A. Brandes, 2006: Improving parameterization of rain microphysics with disdrometer and radar observations. *Journal of the Atmospheric Sciences*, **63**, 1273–1290. 3
- Zrnic, D. S., T. D. Keenan, L. D. Carey, and P. May, 2000: Sensitivity analysis of polarimetric variables at a 5-cm wavelength in rain. *Journal of Applied Meteorology*, **39**, 1514–1526. 23, 28
- Zrnic, D. S. and A. Ryzhkov, 1996: Advantages of rain measurements using specific differential phase. *Journal of Atmospheric and Oceanic Technology*, **13**, 454–464. 24
- Zrnic, D. S., A. Ryzhkov, J. Straka, Y. Liu, and J. Vivekanandan, 2001: Testing a procedure for automatic classification of hydrometeor types. *Journal of Atmospheric and Oceanic Technology*, **18**, 892–913. 2, 25

# Acknowledgements

The realization of this thesis would not have been possible without help and support from numerous people to whom I would like to express my gratitude.

Prof. Ulrich Schumann, for his willingness to accept me as a Ph.D. student and giving me the possibility to work at the DLR Institute of Atmospheric Physics. His comments and suggestions improved the work substantially.

I would like to thank Prof. Susanne Crewell for reviewing this thesis as a co-examiner and for accompanying this work during the last years.

I am deeply grateful to Dr. George Craig for the most stimulating discussions and the critical review of this thesis. His comments coming from the modeling side were always inspiring and substantially contributed to this thesis.

I would like to thank Martin Hagen for introducing me to the exciting world of polarimetric radar and for setting up such an visionary project. He accompanied this thesis from the very beginning and had always time to answer my questions.

Many thanks go to Christian Keil for being one of my supervisors and for introducing me to the mysteries of NWP. I was lucky to profit from his profound expertise on mesoscale modeling and his support running the LMK for me.

I would like to thank Evelyne Richard for providing me with the MesoNH simulations and her great interest in my work. Thanks for very stimulating discussions and comments coming from the modeler's point of view.

Many thanks go to Günther Haase, who provided the code of the conventional radar forward operator RSM and for his enthusiastic support.

I would like to thank Prof. Bringi (Colorado State University, Ft. Collins) for supplying the T-Matrix code.

Thanks to all the people working within the project QUEST for the very interesting workshops and showing me that there is more than polarimetric radar.

Many thanks go to the radar group of our department for maintaining POLDIRAD and providing me with such excellent data.

I would like to thank the LMK group of DWD for rapid replies to any kind of questions.

My thanks go to all members of the department for such a pleasant working atmosphere and assigning me the title of a 'social event manager'.

Special thanks to all my friends for their great support and for making life so exciting.

Finally, I would like to thank my family and especially my parents who encouraged me to go my way and always gave me the support I needed.

# Curriculum Vitae

Monika Pfeifer

Born on July 18th, 1977 in München.

## University Education

Since September 2003	Scientific Researcher and Ph.D. Student at DLR Institut für Physik der Atmosphäre, Oberpfaffenhofen
April 2003	Diploma in Meteorology, Master Thesis: "Abhängigkeit der UV-Strahlung von der Seehöhe: Untersuchung am Beispiel Boliviens"
1999 - 2003	Studies of Meteorology, Ludwig-Maximilians-Universität München
September 1998 - June 1999	Studies of Physics, Universidad de Sevilla, Spain
1996 - 1998	Studies of Meteorology, Ludwig-Maximilians-Universität München

## Primary and Secondary Education

1987 - 1996	Gymnasium der Armen Schulschwestern v.u.l.Fr. am Anger, München
January - April 1994	Lycee Mixte Raynouard, Brignoles, France
1983 - 1987	Primary School, Taufkirchen

## Internships and Work Experience

2001 - 2003	Junior Scientist at Meteorologisches Institut München
June - August 2002	Universidad de La Paz, Bolivia
March - April 2001	Chinese Academy of Sciences, Beijing, China
August - September 2000	MeteoFrance, Toulouse, France
March - April 2000	Alfred-Wegener-Institut für Polarforschung, Bremerhaven
March - April 1998	DLR Institut für Physik der Atmosphäre, Oberpfaffenhofen
September - October 1997	ZAMG, Vienna, Austria

# Index

- 2 Component Scheme, 16, 105
- 3 Component Scheme, 16, 105
- 4/3 Earth Radius Model, 30, 37, 104
  
- Absorption, 34
- Aggregation, 7, 10
- Anaprop, 36
- Attenuation, 23–25, 29–31, 38
- Axis Ratio, 8, 11, 12, 23, 43–46, 50
  
- Backscatter Cross-Section, 20
- Backscatter Matrix, 32
- Beam Propagation, 35, 36
- Break Up, 7, 9
- Brightband, iii, 23, 24, 34, 49, 59, 105
  
- Canting Angle, 9, 23, 24, 32, 33, 42–45, 50
- Coalescence, 7
- Complex Index of Refraction, 20
- Condensation, 7
- Convective Precipitation, 1, 8, 76
- Cross Correlation, 24
  
- Density, 11, 17, 19
- Deposition, 7
- Dielectric Constant, 22–24, 26, 30, 32, 33, 42, 45, 46, 49, 105
- Differential Phase Shift, 24
- Differential Reflectivity, 23, 24, 33
- Drop Shape, 8
- Drop Size Distribution, 8, 9
  
- Effective Radius, 37
- Equivalent Diameter, 9, 16, 43
- Evaporation, 7
  
- Falling Behavior, 12
- Forward Operator, iii, 3, 28–30, 41, 104
  
- Gamma Distribution, 9
- Gaseous Attenuation, 38
  
- Graupel, 8, 11, 26, 47
  
- Hail, 8, 24, 26, 39
- Heterogeneous Nucleation, 6
- Hydrometeor Classification, 24–26, 105
  
- Ice Enhancement, 7
- Intercept Parameter, 9, 43
  
- Linear Depolarization Ratio, 23, 33
- Liquid Water Content, 9
- Logarithmic Reflectivity Factor, 21
- Lognormal Distribution, 9
- Lokal-Modell, 16
- Lokal-Modell-Kürzestfrist, 2
  
- Marshall-Palmer Distribution, 9, 16–18
- Maxwell Garnet Formula, 35
- Median Diameter, 9
- Melting, 7, 49, 59
- MesoNH, 18, 77
- Microphysical Parameterization Scheme, 2, 13, 59, 104
- Mie Scattering, 20, 25, 30, 33
- MM5, 17
- Model-to-observation approach, 3, 28
- Moments of the DSD, 9
  
- Normalized Distribution, 9
- Nucleation, 6
- Numerical Weather Prediction, iii, 1, 59, 76, 104
  
- Observation-to-model Approach, 3, 28
  
- Particle Size Distribution, 8, 43
- Polarimetric Radar, 2, 19, 22, 24, 26, 28, 104
- POLDIRAD, 4, 20, 24, 25, 37, 40, 43, 49, 52, 60, 61, 68, 72, 77
- PPI, 39
- Propagation Phase, 25

- Quantitative Precipitation Forecast, 1, 104
- Radar Constant, 21
- Radar Equation, 20
- Radar Reflectivity, 21
- Radar Reflectivity Factor, 9
- RadarSimulationsModell, 3, 28–31, 52
- Rain, 8, 24, 26, 39
- Rain Rate, 9, 23
- Rayleigh Scattering, 20, 30, 33
- Reflectivity, 22
- Reflectivity Factor, 21, 22
- Refractive Index, 30, 34–37
- Refractivity, 36
- Reisner scheme, 17
- RHI, 39, 40
- Riming, 7, 11
- Sedimentation, 7
- Snow, 8, 10, 26, 43, 48
- Specific Attenuation, 39
- Specific Differential Attenuation, 39
- Specific Differential Phase, 24
- Stratiform Precipitation, 1, 8, 16, 59
- Sublimation, 7
- Subrefraction, 36
- Superrefraction, 36
- SynPolRad, iii, 4, 29, 31, 35, 37–39, 41, 42, 45, 46, 50, 51, 58, 104
- T-Matrix, 3, 4, 25, 28, 30, 33, 43, 52, 104
- Terminal Falling Velocity, 7, 46
- Thompson Scheme, 17, 105
- Transmission Matrix, 39